12-2006

HARMONIC DETECTION OF RESONANCE IN MICRO- AND NANO- CANTILEVERS

Jay Gaillard

Clemson University, jgailla@clemson.edu

Follow this and additional works at: https://tigerprints.clemson.edu/all_dissertations

Part of the Condensed Matter Physics Commons

HARMONIC DETECTION OF RESONANCE IN
MICRO- AND NANO- CANTILEVERS

A Thesis
Presented to
the Graduate School of
Clemson University

In Partial Fulfillment
of the Requirements for the Degree
Doctor of Philosophy
Physics

by
Jay B. Gaillard
December 2006

Accepted by:
Dr. Apparao M. Rao, Committee Chair
Dr. Joseph R. Manson
Dr. Malcolm J. Skove
Dr. Terry M. Tritt

ABSTRACT

Over the past decade there has been an explosion in the study of cantilevered beams on the micron and submicron dimension. The applications and research that involve these structures include state-of-the-art electronic components, sensors, and more recently, studies aimed at elucidating the mechanical properties of cantilevered carbon nanotubes and semiconducting nanowires. In nanoelectro-mechanical systems (NEMS), it is desirable to develop a capacitive readout method involving only two electrodes that are fully compliant with standard CMOS technology. However, the main drawback with this method is the ability to detect resonance in the presence of parasitic capacitance, which is due to the fringing electric fields present between the electrodes (cantilever and the counter electrode).

The work presented in this thesis deals with the electrical actuation / detection of mechanical resonance in individual micron and sub-micron sized cantilevers. The aim is to overcome parasitic capacitance which masks the detection of resonance signal in these cantilevers thereby increasing the signal-to-background ratio (SBR). In our method, a silicon microcantilever, or cantilevered multi-walled carbon nanotube (MWNT), is placed close to a counter electrode whose potential is varied at a frequency ω. An electrical signal comes from the flow of charge on and off of the cantilever when ω equals a resonant frequency ω_0 of the cantilever. Higher harmonics of ω_0 are measured to overcome the parasitic capacitance. This technique, termed harmonic detection of resonance (HDR), allows detection at frequencies well removed from the driving

frequency thereby increasing the SBR by ~3 orders of magnitude. It is shown that HDR allows the detection of resonance even in multi-walled carbon nanotubes, which have diameters on the order of 50 nm. Furthermore, superharmonics inherent to electrostatic actuation, are shown to occur at driving frequencies of ω_0/n where $n = 1, 2, 3, \ldots$.

DEDICATION

During my graduate studies, my younger brother passed away. May our family find comfort that this thesis is dedicated with love to the memory of Michael David Sneed Jr., 1983-2004.

ACKNOWLEDGMENTS

To all of those who gave their friendship and support throughout my graduate career, I give my deepest and most sincere gratitude. I would like to thank those who were instrumental in my development as a scientist including: my advisor, Dr. Apparao Rao; Dr. Malcolm Skove; and my father, Julius Gaillard.

Firstly, my advisor, Dr. Apparao Rao, has given me the guidance and friendship that is not commonly found in a person in his position. My research has been inspiring and challenging with his support. Besides being an excellent advisor, he has been as close to me as a relative and a good friend. I am glad that I have gotten to know Rao in my life.

Dr. Malcolm Skove became involved, just out of interest, with this project a couple of years ago. From the very beginning he took a good idea and made it work. It was his knowledge of the electronics and the lock-in amplifiers that helped develop the HDR method. He also helped develop the theory used throughout this thesis, specifically he worked out the theory in chapter 4. We worked closely together in the lab, and for that I am grateful and fortunate to have had so much of his time. In addition to his contributions to the research, Malcolm has become a great friend and role model.

To truly do well in the lab environment, a good scientist should not only have a great intellect, but he/she must also have good hands on skills as well. Before I started my research career as an undergrad six years ago, I worked with my father landscaping for over ten years. I gained invaluable experience working on machinery, landscaping in a fast paced and arduous environment, and interacting with the many people that worked with us. The hand skills gained through this experience may have been the most valuable

thing to help in the lab environment. Without the work ethic and leadership skills that I gained from my father, I wouldn't be the person that I am today.

I had the privilege of supervising and working with several students who are doing their graduate work in our group and have been somehow beneficial for the presented work in this thesis. J.D. Taylor provided the simulation on the superharmonics in Chapter 6. Razvan Ciocan developed the theoretical work in Chapter 5, and he wrote the Labview program to capture the data for the measurements in Chapters 4-6. I would like to acknowledge those in the group that have spent time enjoying this experience with me. Rahul, Gayatri, Matt, Jason, JD, and Yang, thanks for being such good friends. I will miss you all.

To my beloved wife Vikki, I am thankful for your love and support. And thanks for undertaking the challenge of formatting and proofreading this thesis. To my children, Nicholas and Olivia, you guys have been my "happy thought" throughout my graduate career. To my mother, without your unconditional love and support, I would not have ever made it this far. To my step father, Mike, who I have a relationship with like no other, you have always inspired me to keep going and have always trusted that I would finish each challenge faced in graduate school and in life.

TABLE OF CONTENTS

Table of Contents (Continued)

Table of Contents (Continued)

LIST OF TABLES

LIST OF FIGURES

List of Figures (Continued)

List of Figures (Continued)

List of Figures (Continued)

CHAPTER 1

INRODUCTION

1.1 Introduction

The ability to build extremely small devices via recently discovered micro- and nano- fabrication processes has opened the door to the possibility of electromechanical machines and sensors of a size existing only in the realm of science fiction in previous generations. For instance, many methods now exist to build working microelectro-mechanical systems (MEMS) as well as even smaller nanoelectro-mechanical systems (NEMS). While the technology to build these devices is continuing to expand and grow, practical applications for such devices remain elusive. Problems currently faced by researchers in taking this final step often center around the challenges to be overcome in regard to communicating to the macroscopic world the mechanical motion and/or the electronic signals generated on the micro- or nano-sized scale. For instance, as the devices are so small, the capacitance of a signal junction can approach the unavoidable parasitic capacitance due to the existence of junctions between components of the device. As such, the devices can have an extremely low signal to noise ratio, making the detection of an electrical signal very difficult, if not impossible.

One of the primary mechanical elements being utilized in the development of MEMS and NEMS technology are micro- and nano-sized cantilevers. Cantilever-based devices are often used in sensing or actuating technologies and are generally based upon

the changes in a mechanical property of the cantilever due to absorption of a species at the cantilever surface or changes in the physical characteristics of a sample including, for instance, pressure/acceleration changes, magnetic force changes, temperature changes, and/or extremely small changes in mass. Detection of changes in resonance frequency of the cantilever is one particular mechanical property that has been used in many such regimes. In the past, changes in the oscillating or resonance frequency of a micro- or nano-sized cantilever have generally been limited to determination through optical detection, e.g., analysis of the deflection properties of a laser directed at a reflecting surface of the cantilever, through analysis and detection of changes in the resistivity of a piezoresistor integrated into the cantilever, or through analysis of magnetically induced signals. Difficulties exist with these detection methods, however. For instance, optical detection techniques require optical access to the cantilever as well as the utilization of relatively expensive laser technologies. Integration of a piezoresistor onto a cantilever so as to detect changes in resistivity on the material can necessitate increase in size as well as cost of the apparatus. Also, the large magnetic fields required in magnetic systems can be difficult and expensive to establish.

This thesis presents a detection scheme based on electrostatic transduction which facilitates the ability to convert mechanical vibrations on the micron and nano-scale into an electrical signal. First a study is shown for which the mechanical properties of individual nanotubes was found without electrical detection, and then the thesis develops to show the electrical detection method and its incredible ability to convert complicated mechanical vibrations from micro- and nano- cantilevers into an electrical signal.

1.2   History of micro- and nano- cantilevers

The history of micro- and nano- cantilevers began with the invention of the Atomic Force Microscope (AFM) [1]. In their ground-breaking paper, Binnig et al. found promise in measuring the displacement of a spring, particularly a cantilever, to mimic the imaging process of the Scanning Tunneling Microscope (STM). They used a cantilever with a sharp tip at the end to scan the surface of a flat sample to obtain a topographic line scan of the surface. With the recent advances in silicon micromaching, the AFM soon became a common tool in nanotechnology labs around the world. Once researchers became aware of the remarkable sensitivity of the AFM cantilever, they began to use these micron sized structures as stand alone devices to measure any change in the environment surrounding the cantilevers by monitoring a change in resonant frequency. In recent years, there has been an explosion in development of cantilever transducers as a platform for chemical and biological sensors [2]. Cantilevers have been shown to detect a wide range of chemical, physical, and biological analytes [3-7]. To make a sort of fingerprint to distinguish one analyte from another, researchers have gone even further to develop an artificial nose based on arrays of microcantilevers [8]. The usefulness of microcantilevers has also played a major role in the development of microelectronics, particularly in MEMS. Cantilevers are the most ubiquitous structures in these systems because they are the easiest to machine and mass produce. They have the advantage over structures such as doubly-clamped beams which, although structurally more stable, deflect less under the same applied force, making it more difficult to measure the deflection. With the application of micro-cantilevers in a mature phase, recent studies are

directed more towards developing cantilevers on the nanoscale dimensions which add advantages such as faster speeds and greater sensitivities.

1.3   Actuation methods

As a transducer, a cantilever is used to translate mechanical energy into electrical signals [9]. In general, this means that physical, chemical, or biological stimuli can affect the mechanical characteristics of the cantilever, which in turn, can be translated into an electrical signal. It can operate in a static mode, where the cantilever just deflects from an equilibrium position, or in a dynamic mode, where the cantilever vibrates at its resonant frequency. In this thesis, we are only concerned with the dynamic mode. The most common actuation methods are piezoelectric and electrostatic. Other methods include thermal and magnetic actuation. Experimental results for the piezoelectric and electrostatic techniques are presented in chapter 4.

1.3.1   Piezoelectric actuation

Because of its use with the AFM, piezoelectric actuation is the most known actuation method used for exciting a cantilever into resonance. This method takes advantage of certain crystalline materials which expand and contract when an electric field is applied. For the AFM, a piezoelectric sheet is sandwiched between two metal plates where alternating voltages are applied. The cantilever is attached to a small (~3mm × 5mm rectangle) chip which is mounted, usually glued, near the piezoelectric sheet. The frequency of the applied voltage is swept until it matches the fundamental resonant

frequency of the cantilever. The resonance of this method is generally limited to the kHz range.

1.3.2 Electrostatic actuation

In MEMS, electrostatic actuation is common, and is the most preferred method used in a cantilever-based system [10-16]. This method is convenient to incorporate with the fabricating processes used to make micro- and nano- cantilevers. For this technique, a parallel plate configuration can be used with the thinner plate able to vibrate at resonance. As can be seen in Fig. 1.1, an ac and a dc voltage are applied to one plate, the counter electrode, while the other plate, the cantilever, is set to ground. The basic idea is to sweep the frequency of the ac voltage until the cantilever is found to resonate. Its resonance is due to the time dependent force that drives the motion of the cantilever.

1.4 Detection methods

Measurement of the deflection of a micro- or nano- cantilever requires a detection scheme that can monitor any parameter which is directly related to the deflection in real time with at least nanometer accuracy [2]. Typically, the amplitude and additional information from the phase are measured in the resonant mode. In the past, the optical beam deflection, originally employed by the AFM, was common, but became ineffective when used with cantilevers at the nanoscale. This has led to other detection methods which can not only measure deflection in nanoscale cantilevers, but can be incorporated with MEMS and NEMS.
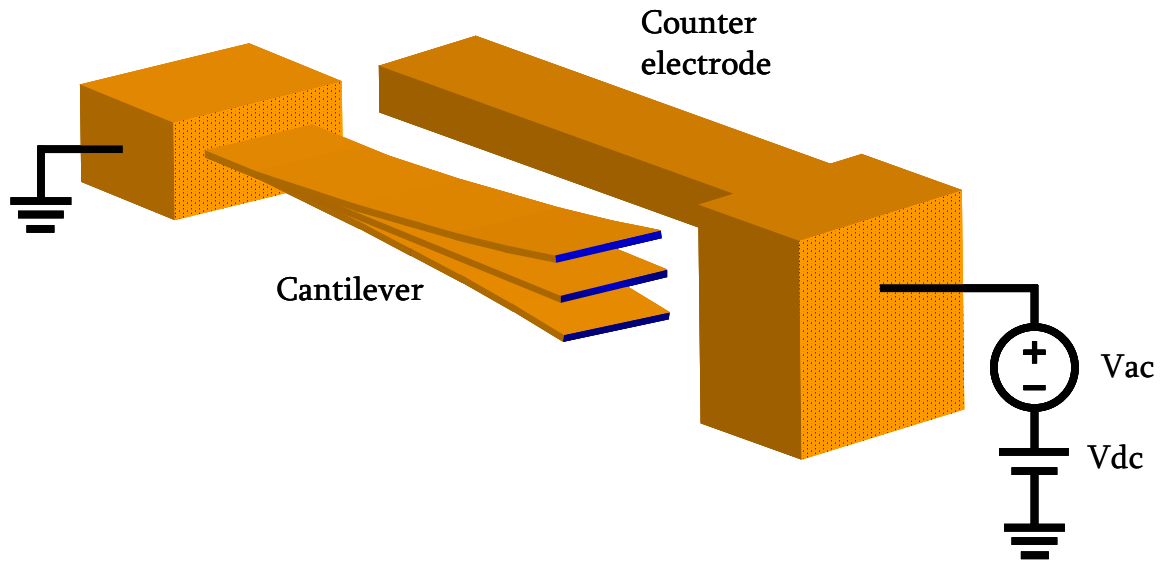
Figure 1.1: Schematic illustration of electrostatic actuation. The ac and dc voltage is applied to the counter electrode. The cantilever is grounded to maintain a potential difference. The frequency of the ac voltage is swept until the cantilever resonates, which can be detected by most detection schemes for microcantilevers. For capacitive detection the ground on the cantilever is replaced by detection electronics.

1.4.1 Optical detection

Optical detection includes the optical beam deflection method, typically used with microcantilevers, and interferometry, a method that is applied to both microcantilevers and nanocantilevers. With optical beam deflection, a laser diode is used to bounce a laser beam off of the reflective surface of the cantilever and to a position sensitive

photodetector (PSD). Originally associated with AFM, the optical beam deflection method has been used for numerous applications with microcantilevers; however, this method does have its limitations. For instance, the surface of the cantilever must be reflective eliminating nonreflective materials. The bulky equipment used for these measurements limits the cantilevers integration with MEMS or any other portable devices. Additionally, the bandwidth of the PSDs is typically on the order of several hundred kilohertz. Interferometry can be used for high bandwidth high resolution mapping of these cantilevers. This enables applications with cantilevers on the nanoscale, but the equipment is even larger than for the PSD method.

1.4.2 Visual detection

With the numerous techniques available for detecting resonance on the micron scale and the lack thereof for the nanoscale, early measurements used visual detection for finding the resonance in nanocantilevers. Here, nanocantilevers include nanofabricated silicon cantilevers and cantilevered nanotubes, nanowires, and nanobelts. Electrically induced mechanical oscillations in such cantilevers have been recorded using visual detection methods that involve the use of a transmission electron microscope [17], scanning electron microscope [18], field emission microscope [19], or an optical microscope [20, 21]. It is difficult with this technique to acquire quantitative information beyond the value of the maximum resonance. Additionally, this method is limited when measuring environmental changes, such as pressure, temperature, or presence of absorbents.

1.4.3   Electrical Detection

Some common electrical detection techniques are the piezoresistance, piezoelectric, capacitance, and electron tunneling methods [2]. The piezoresistance and piezoelectric methods measure the resonance of the cantilever by a change in resistance and charge induced from applied stress. The main drawback of both these methods is their requirement for intricate electrical contacts to the cantilever. With the piezoresistive technique, a current is required to flow through two "legs" which make up the cantilever. With a current path in the cantilever, heat is created which can cause thermal drifts. Fabrication for these techniques is also complicated, limiting their construction for nanoscale sizes. The structure of the electron tunneling method is simply a configuration that requires that a cantilever, typically on the nanoscale, is charged and then touched to a counter electrode to release this charge. Although cantilevers can be made on the nanoscale, touching the cantilever to a counter electrode dampens the motion of the cantilever which in turn impedes its performance. The most desired detection scheme is capacitance detection. In this section, this discussion is limited to detection of the dynamic capacitance between a cantilever and its counter electrode (see Fig. 1.1). When in resonance the change in the capacitance of the system creates a dynamic signal as follows [22]:

$$I(t) = \frac{d(CV)}{dt} = C(t)\frac{\partial V(t)}{\partial t} + V(t)\frac{\partial C(t)}{\partial y(t)}\frac{\partial y(t)}{\partial t} \qquad (1.1)$$

where z is the deflection of the cantilever in a direction perpendicular to its surface. The first term in equation (1.1) corresponds to a signal created by the ac voltage applied to the static capacitance. The second term comes from the oscillation of the cantilever. This method is limited by the signal coming from the first term which is much larger than the

desired signal coming from the second term. Due to additional electrical pickup, the first term in equation (1.1) is generally larger than a signal strictly coming from the static capacitance between the cantilever and counter electrode. Since an electric field is also present across the contacts, which can be large compared to the cantilever, the first term is even further enhanced. These signals coming from the first term in equation (1.1) are called parasitic capacitances. Much work has been done to create geometries to minimize the parasitic capacitance using intricate micro and nano fabrication schemes incorporated with CMOS on-chip circuitry [22, 23]. Unfortunately, little or no results have come from these efforts. Capacitive detection still remains, however, the most sought out detection scheme for electrically excited cantilevers [24].

CHAPTER 2

GENERAL THEORY

2.1 Mechanics of cantilevered beams

The purpose of this section is to show the details involved with the mechanics and mechanical properties of a micro- or nano- cantilever. The discussion of the mechanical vibrations of a cantilevered beam is usually limited to the spring constant and resonant frequency. Some important topics to understand when measuring the resonance of a cantilever are the shape of its amplitude and phase vs. frequency curves, and the value of the frequencies at which the amplitude is a maximum and how they relate to the Young's modulus and the physical characteristics of the cantilever.

2.1.1 Equation of motion

The simplest example of an oscillatory system is a mass connected to a spring with a single degree-of-freedom, a simple harmonic oscillator. When the mass is set in motion, a restoring force is created by the elastic spring to bring it back to equilibrium. If x is the displacement of the spring, then the motion of the mass is described by

$$m\ddot{x}(t) + kx(t) = 0 \qquad (2.1)$$

and the solution is given by

$$x(t) = x_0 \cos(\omega t + \phi) \qquad (2.2)$$

where $\omega_0 = \sqrt{k/m}$, x_0 is the amplitude of vibration, and ϕ is the phase constant of the oscillation. The amplitude and phase are given by the initial conditions.

The motion of a real system is not governed by such a simple equation, but may involve damping, a time dependent force, and nonlinearities. If we add damping and a driving force to the equation of motion then it becomes

$$m\frac{\partial^2 x(t)}{\partial t^2} + b\frac{\partial x(t)}{\partial t} + kx(t) = F_0 \cos(\omega t). \tag{2.3}$$

Assuming a steady state solution of the form

$$x(t) = A\cos(\omega_0 t + \phi) \tag{2.4}$$

we get an amplitude of

$$A = \frac{F_0/m}{\sqrt{(\omega_0^2 - \omega^2)^2 + 4\omega^2\beta^2}} \tag{2.5}$$

and a phase of

$$\phi = \arctan(\frac{\omega_0^2 - \omega^2}{2\omega\beta}) \tag{2.6}$$

where

$$\beta = \frac{b}{2m}. \tag{2.7}$$

A graph which represents the amplitude and phase from equations 2.5 and 2.6 respectively is shown in Fig. 2.1. The values used to create the graph in Fig. 3 were $F_0/m = 200$, $\beta = 2$, and $\omega_0 = 50$.

With

$$b = \frac{m\omega_0}{Q} \tag{2.8}$$

we get

$$Q = \frac{\omega_0}{2\beta} \tag{2.9}$$

where Q is the quality factor which defines the sharpness of the peak. The quality factor in this case is found to be $Q = 12.5$. Formally, the quality factor compares the frequency of the oscillations to the rate that energy dissipates where

$$Q = \left(\frac{total\ energy\ stored}{energy\ lost\ in\ cycle} \right) \tag{2.10}$$

Generally, the quality factor is defined by $Q = \omega_0 / \Delta\omega$ where $\Delta\omega$ is the full width at half maximum. This is defined by the information in the peak because, in reality, not enough is usually known about the damping of the system to evaluate Q directly from the equation of motion. Additionally, damping is only one of the energy losses in the system. Energy can be lost to internal friction in the cantilever from defects, phonon-phonon interaction, and phonon-electron interactions. Other losses include surface effects such as tension, thermoelastic effects, coupling between the cantilever and its anchor, etc.

A realistic system can have many different types of nonlinearities which further complicate the equation of motion. One such nonlinearity is the so called Duffing effect. This nonlinearity is due to driving the oscillator with an amplitude such that cubic terms in the restoring force become important. The equation of motion which describes the Duffing effect has an additional cubic term, which is written as

$$\frac{\partial^2 x(t)}{\partial t^2} + \frac{\omega_0}{Q} \frac{\partial x(t)}{\partial t} + \omega_0^2 x(t) + g x^3(t) = \frac{F_0}{m} \cos(\omega t) \tag{2.11}$$

which for a cantilever is
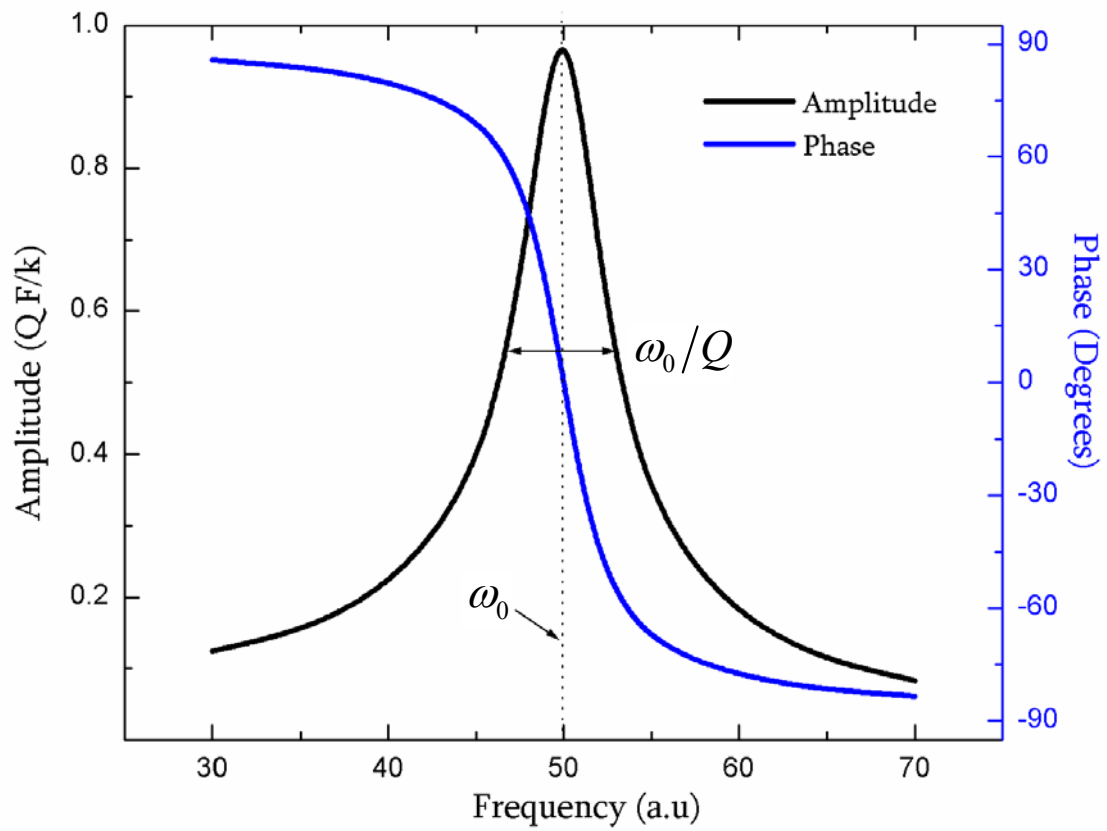
Figure 2.1: This graph represents the amplitude and phase of a forced and damped harmonic oscillator. It was created using equations 2.5 and 2.6. The phase changes by 180^0.

$$g = \frac{E}{18\rho}\left(\frac{2\pi}{L}\right)^4,$$ (2.12)

where ρ, L, and E are the density, length, and Young's modulus of the cantilever respectively. An experimental example of the Duffing effect is presented in Chapter 4.

2.1.2   Spring constant

In this section, the spring constant is derived for a rectangular cantilever with dimensions of length L, width w, and thickness t (Fig. 2.2). The deflection y as a function of position along the cantilever x is given by [25]

$$\frac{\partial^2 y}{\partial x^2} = -\frac{M}{EI}$$ (2.13)

which is obtained by equating the curvature of the lever to the bending moment at each point assuming small oscillations where M is the bending moment, E the Young's modulus, and I the moment of inertia. A force acting perpendicular to the surface at its end according to Hooke's law is related to the spring constant k by

$$F = -ky.$$ (2.14)

The bending moment for this force is given as

$$M = Fx.$$ (2.15)

The boundary conditions associated with this moment are

$$y(0) = 0 \quad \text{and} \quad \frac{dy}{dx}\Big|_{x=0} = 0$$ (2.16)

inserting M into equation (2.13), integrating twice while applying the boundary conditions gives
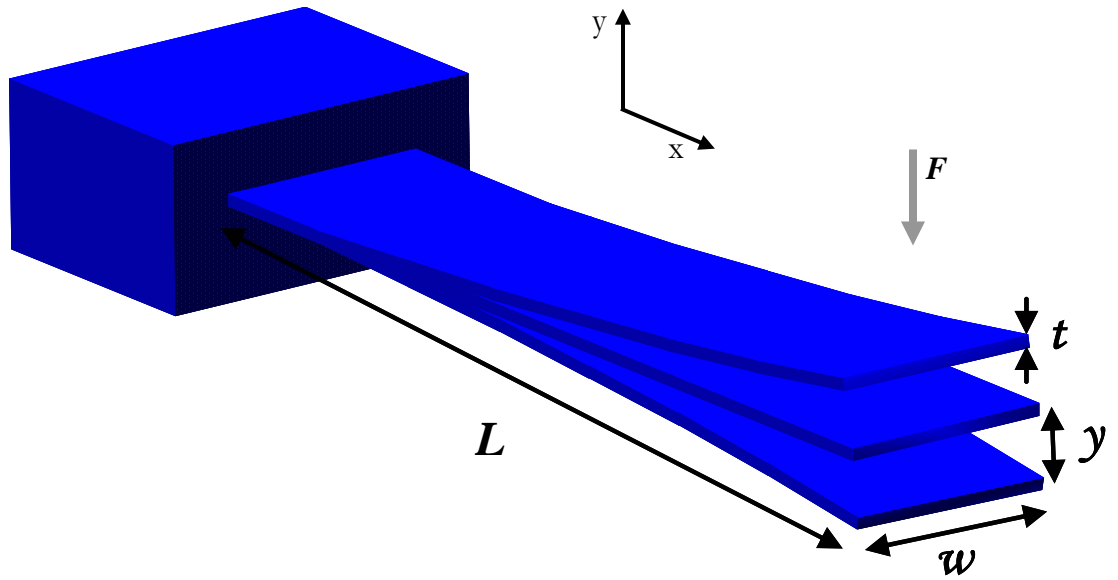
Figure 2.2: Simple cantilever with dimensions length L, width w, and thickness t. The displacement of the bending cantilever is denoted as y. For the derivation of the spring constant, the force F is placed at $x=L$.

$$y(x) = \frac{Fx^2}{6EI}(x - 3a) \qquad (2.17)$$

then the bending at the tip becomes

$$y(L) = -\frac{L^3}{3EI}F \qquad (2.18)$$

and hence the spring constant is [25]

$$k = 3\frac{EI}{L^3}. \qquad (2.19)$$

2.1.3 Elasticity

The modulus of elasticity, or Young's modulus E, describes the relative stiffness of a material when a force is applied to it. In the elastic regime, the Young's modulus has a linear relationship with stress and strain at any given point, which can be expressed as [25].

$$\sigma = E\varepsilon \qquad (2.20)$$

where σ is the stress and ε is the strain. The strain describes the relative elongation δ of a bar of length ℓ, and is defined as

$$\varepsilon = \delta / \ell \ . \qquad (2.21)$$

From here, we would like to find a relationship between the Young's modulus and the resonant frequency. The resonant frequency and its normal modes can be calculated by using either energy considerations or classical methods. With the first method the fundamental frequency is approximated by equating the strain energy of the cantilever to the kinetic energy when the deflection is zero. The classical solution is more exact and produces the fundamental resonance of the cantilever and its associate modes of vibration as follows:

The classical solution is found by balancing bending and shear forces. To develop this, consider a free body diagram (Fig. 2.3) of a segment of the cantilever of length dx in which the shear and moment changes from V and M to $V+dV$ and $M+dM$, respectively. The moment balance around this segment gives

$$\sum M = (M+dM) + (V+dV)\frac{dx}{2} + V\frac{dx}{2} - M = 0 \qquad (2.22)$$

16
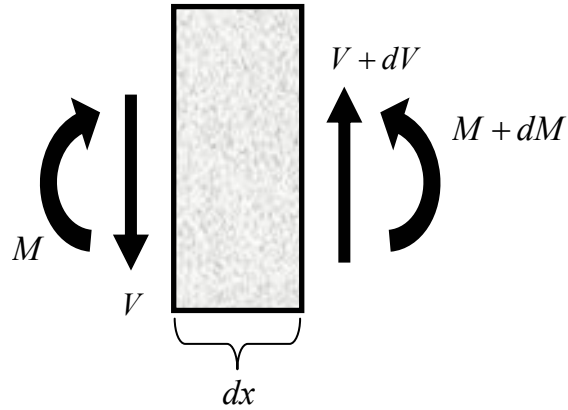
Figure 2.3: Element of the cantilever that shows the balance of the shear forces V with the bending moments M.

As the increment dx is reduced, the term containing the higher-order differential $dVdx$ vanishes in comparison with the others, leaving

$$\frac{dM}{dx} = -V.$$ (2.23)

Following the same coordinates used in Fig. 2.2, we can then equate dV, acting on an element of mass $\rho A dx$, with the acceleration of the element giving

$$dV = -\rho A dx \frac{\partial^2 y}{\partial t^2}.$$ (2.24)

Starting with equation 2.23 we get

$$\frac{\partial V}{\partial x} = -\rho A \frac{\partial^2 y}{\partial t^2}. \tag{2.25}$$

Plugging equation 2.22 into the left side of equation 2.24

$$\frac{\partial V}{\partial x} = -\frac{\partial^2}{\partial x^2} M, \tag{2.26}$$

then plugging M from equation 2.13 into 2.25 we get

$$\frac{\partial V}{\partial x} = \frac{\partial^2}{\partial x^2} \left(EI \frac{\partial^2 y}{\partial x^2} \right) = EI \frac{\partial^4 y}{\partial x^4}. \tag{2.27}$$

Then putting this back into equation 2.24 we can now write the equation of motion of the cantilever as

$$EI \frac{\partial^4 y(x,t)}{\partial x^4} + \rho A \frac{\partial^2 y(x,t)}{\partial t^2} = 0 \tag{2.28}$$

Solving this equation gives the resonant frequencies of the cantilever and its normal modes.

We will find some simple solutions by assuming the solution is of the form $e^{i\omega t} y(x,\omega)$, leading to

$$\rho A (i\omega^2) y(x,\omega) + EI \frac{\partial^4 y(x,\omega)}{\partial x^4} = 0 \tag{2.29}$$

or

$$-\alpha \omega^2 y(x,\omega) + \frac{\partial^4 y(x,\omega)}{\partial x^4} = 0 \tag{2.30}$$

where $\alpha = \sqrt[4]{\frac{\rho A}{EI}}$. The sum of four particular solutions will provide a general solution.

The regular and hyperbolic sin, sinh, cos, and cosh functions reproduce themselves after four derivatives, and thus we may write the solution as [26]

$$y(x,\omega) = A_1 \sin(\alpha\sqrt{\omega}x) + A_2 \cos(\alpha\sqrt{\omega}x) + A_3 \sinh(\alpha\sqrt{\omega}x) + A_4 \cosh(\alpha\sqrt{\omega}x) \qquad (2.31)$$

where the A_i's are determined from the boundary conditions. The solutions provide an orthonormal set of functions that describe the shape of the cantilever. For this case, the cantilever has the end at $x = 0$ clamped and the end $x = L$ free. The appropriate boundary conditions are

$$y(0) = 0 \;\; \text{and} \;\; \frac{\partial y}{\partial x}\Big|_{x=0} = 0$$
$$\frac{\partial^2 y}{\partial x^2}\Big|_{x=L} = 0 \;\; \text{and} \;\; \frac{\partial^3 y}{\partial x^3}\Big|_{x=L} = 0 \qquad (2.32)$$

and after the application of these boundary conditions [26] we get

$$\frac{2 + 2\cos\left(\alpha L\sqrt{\omega}\right)\cosh\left(\alpha L\sqrt{\omega}\right)}{\sin\left(\alpha L\sqrt{\omega}\right) - \sinh\left(\alpha L\sqrt{\omega}\right)} = 0 \qquad (2.33)$$

which yields the characteristic equation for the allowed wavenumbers

$$\cos\left(\alpha L\sqrt{\omega}\right)\cosh\left(\alpha L\sqrt{\omega}\right) + 1 = 0. \qquad (2.34)$$

This equation can be solved numerically to obtain

$$\beta_i = \alpha L\sqrt{\omega_i} = \sqrt{3.5126}, \sqrt{22.034}, \sqrt{61.701} \;\dots\; i = 1, 2, 3, \dots \qquad (2.35)$$

where each value of i represents a different resonant mode. The resonant frequencies ω_i then are

$$\omega_i = \frac{\beta_i^2}{\alpha^2 L^2} = \frac{\beta_i^2}{L^2}\sqrt{\frac{EI}{\rho A}} \;. \qquad (2.36)$$

19

2.1.4 Mechanical properties of carbon nanotubes

Understanding the mechanical properties of nanotubes is the first step towards using the material as a structural element. In the past few years, the extraordinary mechanical properties of carbon nanotubes have been determined by several methods, for example Wong et al. [27] and Poncharal et al. [28]. Wong et al. determined the bending force using an atomic force microscope along the length of an individual multi-walled carbon nanotube (MWNT) pinned at one end to a molybdenum disulfide surface. In the other study, the fundamental and higher harmonic frequency modes were electrically induced in a cantilevered MWNT inside a transmission electron microscope. The elastic bending modulus was found to decrease sharply (from ~1 to 0.1 TPa) with increasing diameter (from 8 to 40 nm), which was attributed to a crossover from a uniform elastic mode to an elastic mode that involves wavelike distortions in the nanotube. Furthermore, the bending modulus of MWNTs was found to depend sensitively on the presence of structural defects present in the nanotubes [29-31]. As a reference, the bending modulus for copper is 130 GPa and 200 GPa for steel.

The strength of a material is intimately connected to its structural imperfections, and in many cases, can depend on its size. For example, graphite whiskers exhibit an elastic modulus as high as 20 GPa, while the typical strength of large fibers is 1 GPa [32]. This is attributed to the fact that the number of imperfections is considerably reduced in the whiskers. As stated previously, it has been suggested that the bending modulus of the nanotubes decrease with an increase in diameter due to the wavelike distortions of the compressed walls in the tube. Here, Poncharal et al. observed no shifts in the resonant frequency at large amplitudes of the vibration for all diameters. If the distortions cause

the modulus dependence with diameter, one would expect a crossover between the small and large vibrations. As this is not the case, it seems more likely that the greater number of imperfections present in the larger diameter nanotubes would be the reason for the strong dependence. Chapter 3 shows a study that compares three different nanotubes with varying imperfections in the walls of the tubes.

To find the Young's modulus of nanotubes we can follow equation 2.35, were the resonant frequency is given as

$$f_i = \frac{\beta_i^2}{2\pi L^2}\sqrt{\frac{EI}{\rho A}} = \frac{\beta_i^2}{8\pi}\frac{1}{L^2}\sqrt{\frac{(D_I^2 + D_O^2)E}{\rho}} \tag{2.37}$$

where D_I and D_O are the inner and outer diameters of the nanotube, ρ is the density, and E is the Young's modulus. Figure 2.4 shows the parameters of a MWNT.
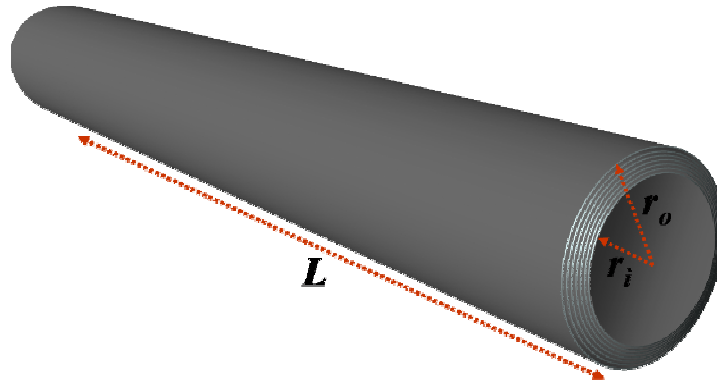
Figure 2.4: Multi-walled carbon nanotube with inner radius r_I, outer radius r_O, and length L where $r_I = \frac{D_I}{2}$ and $r_O = \frac{D_O}{2}$.

2.2 Electrostatic transduction

Electrostatic transduction involves actuating a conductive or conductive coated cantilever into resonance by applying an ac and dc voltage on a nearby electrode parallel to the cantilever and then measuring an electrical signal created by the dynamic capacitance. As pointed out previously [24], sensing motion through dynamic changes of capacitance in MEMS and NEMS is difficult because this dynamic signal is obscured by parasitic capacitances that are many orders of magnitude larger. Techniques for avoiding this problem, such as single electron transistors, [33] often involve low temperatures. Sensing elements such as comb drives along with on-chip circuitry have been added to many micro/nano- fabricated silicon-based NEMS/MEMS resonators to overcome the parasitics [23, 34]. These systems involve intricate multi- element designs which may increase the cost of production and probability for breakdown. An alternative simpler method without all the bells and whistles, therefore, is still desired and is presented in chapter 4.

2.2.1 The force equation

The total voltage applied to the counter electrode is $V(t) = V_{dc} + V_{ac}\cos(\omega t)$, where the V_{dc} term includes the difference between the work potentials of the cantilever and counter electrode. Let $C(t)$ be the capacitance between the cantilever and the counter electrode. The electrostatic energy of the system is then $\frac{1}{2}CV^2$, and the force on the cantilever is $F_c = -\frac{1}{2}\frac{d(CV^2)}{dx} = -\frac{1}{2}V^2\frac{dC}{dx}$. If the vibration amplitude $y(t)$ of the cantilever is small compared to the distance between the cantilever and the counter electrode, then $C(t) \approx C_0 + \frac{dC}{dx}|_{x=0}\, y(t)$, where C_0 and $\frac{dC}{dx}|_{x=0} = -C_0'$ are constants for a

given experimental set up. Thus for small deflections, the Coulomb force on the cantilever is

$$
\begin{aligned}
F_c &= \tfrac{1}{2}C_0'(V_{dc} + V_{ac}\cos(\omega t))^2 \\
&= \tfrac{1}{2}C_0'\{V^2_{dc} + 2V_{dc}V_{ac}\cos(\omega t) + \frac{1}{2}V^2_{ac}[1 + \cos(2\omega t)]\}
\end{aligned}
\tag{2.38}
$$

implying that the cantilever can be viewed as a forced harmonic oscillator driven by a force with two time varying components: $\cos(\omega t)$ and $\cos(2\omega t)$. This means that the cantilever will be driven into resonance at $\omega = \omega_0$ and at $2\omega = \omega_0$, or more clearly, at $\omega = \omega_0/2$. In the past, the study of resonant cantilevers on both the micro- and nano-scale has involved a two term force equation. Chapter 6 shows that resonance occurs at $\omega = \omega_0/n$ and demands a more complete force equation. Using a Fourier expansion, we can write

$$
F(t) \approx F_0 + \sum_{n=1}^{N} F_n \cos(n\omega t + \phi_n) \;,
\tag{2.39}
$$

ad the derivation can be found in chapter 6.

2.2.2   Electrostatic equation of motion

When driven by an oscillatory and static voltage, the cantilever is forced according to equation 2.37. This not only creates a complicated force, but it affects the equation of motion in other ways, such as nonlinearities and a significant change in the spring constant.

For a voltage driven cantilever, we can write, [25]

$$m\frac{\partial^2 y}{\partial t^2} + \gamma\frac{\partial y}{\partial t} + ky = F_0 + \frac{\partial F}{\partial y}y + ... \tag{2.40}$$

From this, we can add the force from equation 2.11 to get

$$m\frac{\partial^2 y}{\partial t^2} + \gamma\frac{\partial y}{\partial t} + ky =$$

$$\frac{1}{2}\left[\left(V_{dc}^2 + \frac{1}{2}V_{ac}^2\right) + 2V_{dc}V_{ac}\cos(\omega t) + V_{ac}^2\cos(2\omega t)\right]\frac{\partial C}{\partial y}\Big|_{y=y_0} \tag{2.41}$$

$$+ \frac{1}{2}\left[\left(V_{dc}^2 + \frac{1}{2}V_{ac}^2\right) + 2V_{dc}V_{ac}\cos(\omega t) + V_{ac}^2\cos(2\omega t)\right]\frac{\partial^2 C}{\partial y^2}\Big|_{y=y_0}y + ...$$

To zeroeth order in y, the equilibrium point is moved from $y=y_0$ to

$$y' = y_0 + \left(V_{dc}^2 + \frac{1}{2}V_{ac}^2\right)\frac{\partial C}{\partial y}\Big|_{y=y_0}/2k \tag{2.42}$$

Let

$$\zeta = y - \left(V_{dc}^2 + \frac{1}{2}V_{ac}^2\right)\frac{\partial C}{\partial y}\Big|_{y=y_0}/2k \tag{2.43}$$

Then

$$m\frac{\partial^2 \zeta}{\partial t^2} + \gamma\frac{\partial \zeta}{\partial t} + k\zeta = \left[V_{dc}V_{ac}\cos(\omega t) + \frac{1}{2}V_{ac}^2\cos(2\omega t)\right]\frac{\partial C}{\partial \zeta}\Big|_{y=y'}$$

$$+ \frac{1}{2}\left[\left(V_{dc}^2 + \frac{1}{2}V_{ac}^2\right) + 2V_{dc}V_{ac}\cos(\omega t) + V_{ac}^2\cos(2\omega t)\right]\frac{\partial^2 C}{\partial \zeta^2}\Big|_{y=y'}\zeta + ... \tag{2.44}$$

or

$$m\frac{\partial^2 \zeta}{\partial t^2} + \gamma\frac{\partial \zeta}{\partial t} + \left\langle\begin{array}{c}\left[k - \frac{1}{2}\left(V_{dc}^2 + \frac{1}{2}V_{ac}^2\right)\frac{\partial^2 C}{\partial \zeta^2}\Big|_{y=y'}\right]\\-\left\{\left[V_{dc}V_{ac}\cos(\omega t) + \frac{1}{2}V_{ac}^2\cos(2\omega t)\right]\frac{\partial C}{\partial \zeta}\Big|_{y=y'}\right\}\end{array}\right\rangle\zeta$$

$$= \left[V_{dc}V_{ac}\cos(\omega t) + \frac{1}{2}V_{ac}^2\cos(2\omega t)\right]\frac{\partial C}{\partial \zeta}\Big|_{y=y'} + ... \tag{2.45}$$

24

Two more orders in ζ on the right will add a cubic term to the left, but first for convenience let's set

$$\kappa = \left\langle \left[k - \frac{1}{2}\left(V_{dc}^2 + \frac{1}{2}V_{ac}^2\right)\frac{\partial^2 C}{\partial \zeta^2}\Big|_{y=y'}\right] - \left\{\left[V_{dc}V_{ac}\cos(\omega t) + \frac{1}{2}V_{ac}^2\cos(2\omega t)\right]\frac{\partial C}{\partial \zeta}\Big|_{y=y'}\right\}\right\rangle$$

(2.46)

and $\qquad \lambda = \frac{1}{2}\left[\left(V_{dc}^2 + \frac{1}{2}V_{ac}^2\right) + 2V_{dc}V_{ac}\cos(\omega t) + V_{ac}^2\cos(2\omega t)\right].$ (2.47)

Then we can write the final equation of motion as

$$m\frac{\partial^2 \zeta}{\partial t^2} + \gamma\frac{\partial \zeta}{\partial t} + \kappa\zeta + \lambda\left(\frac{\partial^3 C}{\partial \zeta^3}\Big|_{y=y'}\zeta^2 + \frac{\partial^4 C}{\partial \zeta^4}\Big|_{y=y'}\zeta^3 + \dots \frac{\partial^n C}{\partial \zeta^n}\Big|_{y=y'}\zeta^n\right)$$
$$= \left[V_{dc}V_{ac}\cos(\omega t) + \frac{1}{2}V_{ac}^2\cos(2\omega t)\right]\frac{\partial C}{\partial \zeta}\Big|_{y=y'}$$

(2.48)

So we now have an equation somewhat similar to equation 2.11, where it contains damping, higher order terms in ζ, and a forcing term. We can see (1) that the spring

constant $\quad \kappa = k - \frac{1}{2}\left(V_{dc}^2 + \frac{1}{2}V_{ac}^2\right)\frac{\partial^2 C}{\partial \zeta^2}\Big|_{y=y'} + \dots$ is affected by the applied ac and dc

potentials; (2) a nonlinear term proportional to ζ^2 and a Duffing term proportional to

ζ^3 in the higher order terms. Let us consider these effects in order.

(1) The change in the resonant frequency from $\omega_0 = \sqrt{k/m}$ to $\omega_0' = \sqrt{\kappa/m}$, and is a

function of the applied voltages. Note that the actual V_{dc} is the sum of the applied dc

voltage and the difference in the work functions of the surfaces of the cantilever and

counter electrode, but since the cantilever and counter electrode are both coated in gold,

this can be neglected. Now let $V'^2 = \left(V_{dc}^2 + \frac{1}{2}V_{ac}^2\right)$. The change in the resonant frequency

with a change in V'^2 is

$$\frac{d\omega_0'}{dV'^2} = \frac{1}{\sqrt{m_t}}\frac{d\sqrt{\kappa}}{dV'^2} \approx \frac{1}{2}\frac{-\frac{1}{4}\frac{\partial^2 C}{\partial \zeta^2}\Big|_{y=y'}}{2\sqrt{m_t\left(k-\frac{1}{4}V'^2\frac{\partial^2 C}{\partial \zeta^2}\Big|_{y=y'}\right)}} \approx -\frac{\frac{\partial^2 C}{\partial \zeta^2}\Big|_{y=y'}}{8\sqrt{m_t k}} \qquad (2.49)$$

where m_t is the total mass of the cantilever. From this, we would expect that any increase in the ac or dc voltage will decrease the resonant frequency.

(2) The term proportional to ζ^2 makes the equation nonlinear. Although this does not lead to a change in resonant frequency it will create a waveform that is not sinusoidal (and hence the presence of higher harmonics). The next term ζ^3 will cause a Duffing effect with the possibility of steps and hysteresis in the amplitude and phase as a function of frequency, and in extreme cases, chaos.

CHAPTER 3

MECHANICAL PROPERTIES OF CVD GROWN MULTI-WALLED CARBON

NANOTUBES

3.1 Introduction

In this chapter, measurements of the bending modulus (Young's modulus) of several chemical vapor deposition grown multi-walled nanotubes (MWNTs) using a vibrating reed technique [21] is described. Three different precursors were used to produce MWNTs with differing densities of defects in the tube walls. Individual MWNTs were electrostatically driven in air over a dark field light microscope and the bending modulus of the nanotubes was determined from the frequency of the first vibrational resonance. A correlation between the defect density and the bending modulus was found which implies that the bending modulus is relatively more sensitive to wall defects than to the nanotube diameter.

In the past few years, the extraordinary mechanical properties of carbon nanotubes have been determined by several methods, for example Wong et al. [27] and Poncaral et al. [28]. Wong et al. determined the bending force using an atomic force microscope along the length of an individual multi-walled carbon nanotube (MWNT) pinned at one end to a molybdenum disulfide surface. In the other study, the fundamental and higher harmonic frequency modes were electrically induced in a cantilevered MWNT inside a transmission electron microscope. The elastic bending modulus was found to decrease sharply (from ~1 to 0.1 TPa) with increasing diameter (from 8 to 40 nm), which

was attributed to a crossover from a uniform elastic mode to an elastic mode that involves wavelike distortions in the nanotube. Further, the bending modulus of MWNTs was found to depend sensitively on the presence of structural defects present in the nanotubes [29-31]. Here, we demonstrate a novel approach that allows a direct measurement of the mechanical properties of individual MWNTs. Our technique is relatively simpler: the resonance frequency of an electrostatically driven MWNT is determined using a dark field optical microscope. MWNTs with differing densities of defects in the tube walls were prepared from a catalytic decomposition of three different precursors using our thermal chemical vapor deposition (CVD) method [35]. Our resistivity measurements confirm the correlation between the precursor and the defect density in the nanotubes. Young's modulus E as determined from our simpler method correlates well with those reported in the literature.

3.2 Experiment

3.2.1 Three defect defined MWNTs

In our first set of experiments, MWNTs were prepared using a xylene/ferrocene mixture as reported previously [35]. Briefly, the MWNTs are grown on bare quartz substrates by injecting a liquid precursor mixture of ferrocene ($C_{10}H_{10}Fe$) and xylene (C_8H_{10}) with 0.6 at. % Fe into a two-stage thermal CVD reactor (Fig. 3.1) consisting of a low temperature (~200 ^{o}C) preheater followed by a higher temperature furnace (~750 ^{o}C). Typical flow rates of the gases are 200 sccm (standard cubic centimeters per minute) for hydrogen and 675 sccm for Ar. In the second set of experiments, a ceramic boat containing melamine ($C_3H_6N_6$) was decomposed along with the xylene/ferrocene

mixture. Details can be found in reference 36. Our third set of MWNTs were prepared from a catalytic decomposition of a trimethylamine $[(CH_3)_3N]$-ferrocene (TMA/ferrocene) mixture. The synthesis conditions for all three sets of experiment were nearly identical. Representative TEM images of the nanotubes produced from each set are shown in Fig. 3.2. Clearly, the xylene/ferrocene/melamine (Fig. 3.2a) nanotubes exhibit the most defects due to the tendency to form nanotubes with bamboo-like morphology [36]. The nanotubes obtained from the TMA/ferrocene mixture (Fig. 3.2c) showed the least defect density while those derived from the xylene/ferrocene mixture contained intermediate defect density (Fig. 3.2b). As we describe later, we have also measured the electrical resistivity of the nanotubes from these batches used in our elastic property measurements in order to qualitatively substantiate the varying defect densities. The schematic in Fig. 3.2b shows our experimental setup in which an individual MWNT is electrostatically driven into resonance. To vibrate a nanotube, it is first pulled from the as-prepared MWNT array using a sharpened tungsten tip while a DC bias voltage is applied between the nanotube and tip [37]. The dark field image in Fig. 3.3a shows a single MWNT attached to a tungsten probe tip. Next, the nanotube is manipulated on top of a Nikon Epiphot 200 dark field light microscope using two micro-manipulators. Because of their high aspect ratio, a MWNT with a 30 nm diameter, but no less than 2 μm in length, can easily be viewed using 500x or higher magnification. Once the MWNT-tip is positioned, the counter electrode is brought parallel to the MWNT (Fig. 3.3a). The resonance frequency of the nanotube is found by tuning the frequency of an ac charge on the counter electrode. A dc offset is also applied to the counter electrode to increase the amplitude of oscillation. Once a resonance frequency f_r is found, we check to
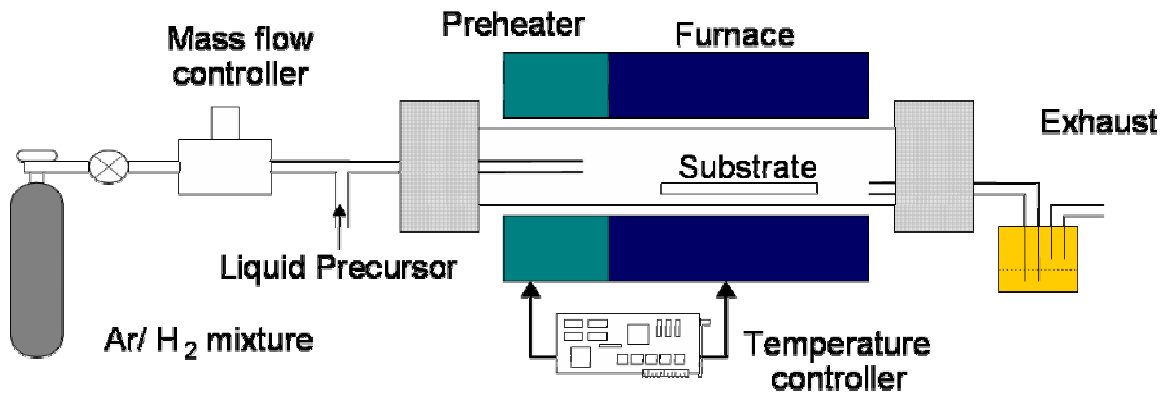
Figure 3.1: A two stage thermal CVD reactor: The MWNTs are grown on bare quartz substrates by injecting a liquid precursor into a two-stage thermal CVD reactor consisting of a low temperature (~200 ^{o}C) preheater followed by a higher temperature furnace (~750 ^{o}C).
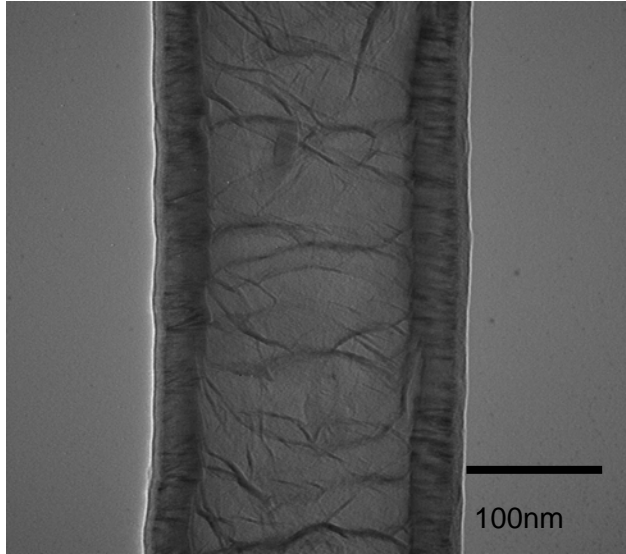
(a)
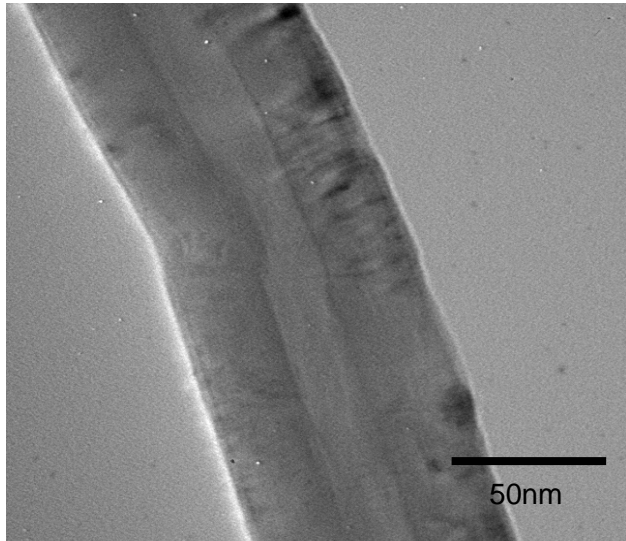
(b)
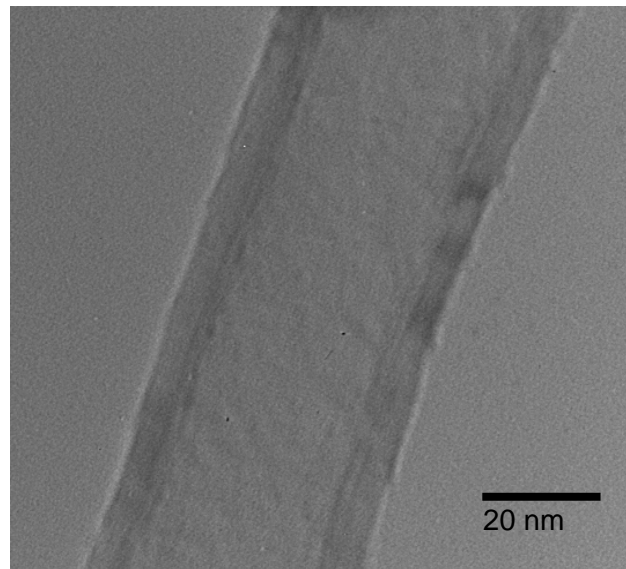
(c)

Figure 3.2 TEM images of three different types of MWNTs produced by thermal CVD. a) A xylene/ferrocene/melamine nanotube, which appears to have the largest defect density in the tube walls. These nanotubes exhibit the so called bamboo-like morphology. b) A xylene/ferrocene nanotube, which has an intermediate defect density. These nanotubes exhibit regions with few wall defects. c) TMA/ferrocene nanotubes with the least amount of wall defects. These nanotubes have few defects in the walls and no major defects for long lengths along the nanotube.

see if the nanotube will also resonate at $f_r/2$ in order to verify that f_r is the fundamental

mode, as discussed previously by Wang et al. [30]. Note that if the voltage on the

counter electrode is $V_0 + V\sin\omega t$, the force on the nanotube is $(V_0 + V\sin\omega t)^2$, which has

Fourier components at both ω and 2ω, as well as a constant term. A plot of the resonance

peak for a TMA/ferrocene derived nanotube is shown in Fig. 3.3c. The amplitude is

plotted as a percentage of the maximum amplitude observed under the dark field

microscope. After determining the fundamental natural frequency, E was calculated for

each nanotube from equation 2.36. Using TEM, an accurate value for the geometric

dimensions of each nanotube was found.

3.3   Mechanical Properties

3.3.1   Defect dependent bending modulus

The data presented in Fig. 3.5 shows a general trend in Young's modulus and its

dependence on the defect density present in the three different types of MWNTs used in

this study. Each MWNT was modeled as a hollow cylinder and its density was computed

using the density of graphite (2.2 g/cm^3) as previously reported, [28] E is expected to

decrease with an increase in tube diameter. The important result here is that the elastic

properties are also sensitive to the defect density. The melamine-doped MWNTs have

periodic defects along their length and the lowest E, ~ 3 GPa. The defects in the

xylene/ferrocene nanotubes are random and occur less frequently which yields an average

Young's modulus of ~ 0.1 TPa while the TMA derived nanotubes (which contained the

least defects) exhibited the highest E, ~ 0.3 TPa. This is the case even though the TMA

derived MWNTs have thinner walls and larger diameters, both of which should generally

(a)

Counter electrode

MWNT

W probe

20 µm

(b)

Counter electrode

W probe

MWNT

Microscope Objective

DC

Function
Generator

(c)

Amplitude (arb. units)

Frequency (kHz)
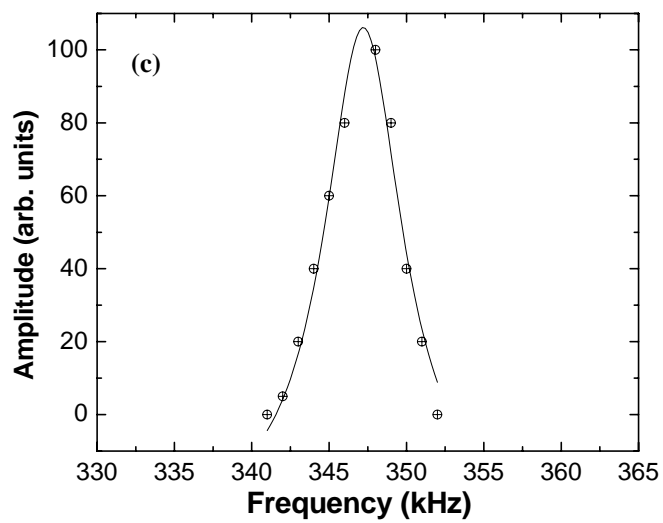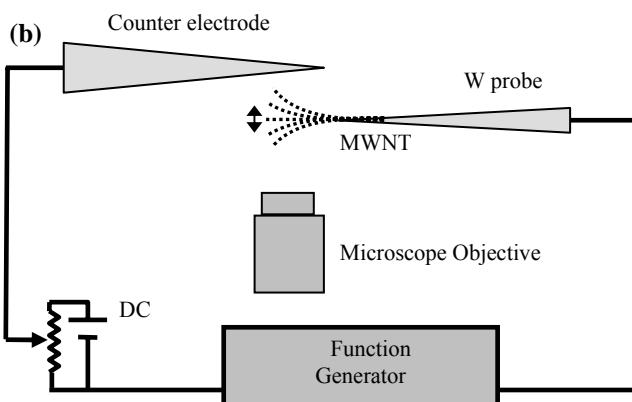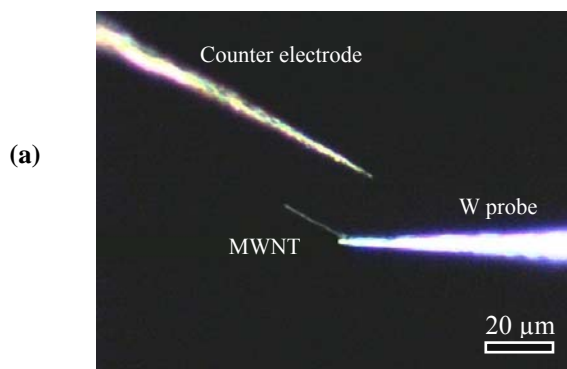
Figure 3.3: a) Dark field image of a MWNT attached to a gold coated tungsten probe with another gold coated counter electrode positioned parallel to the nanotube. When vibrating the nanotube, the counter electrode is ~ 5 μm from the nanotube. b) Schematic of the experimental setup developed for vibrating a MWNT in air over a dark field light microscope. The AC voltage is tuned until the MWNT is found to resonate at its natural frequency. c) Trace of the resonant frequency of an individual MWNT.
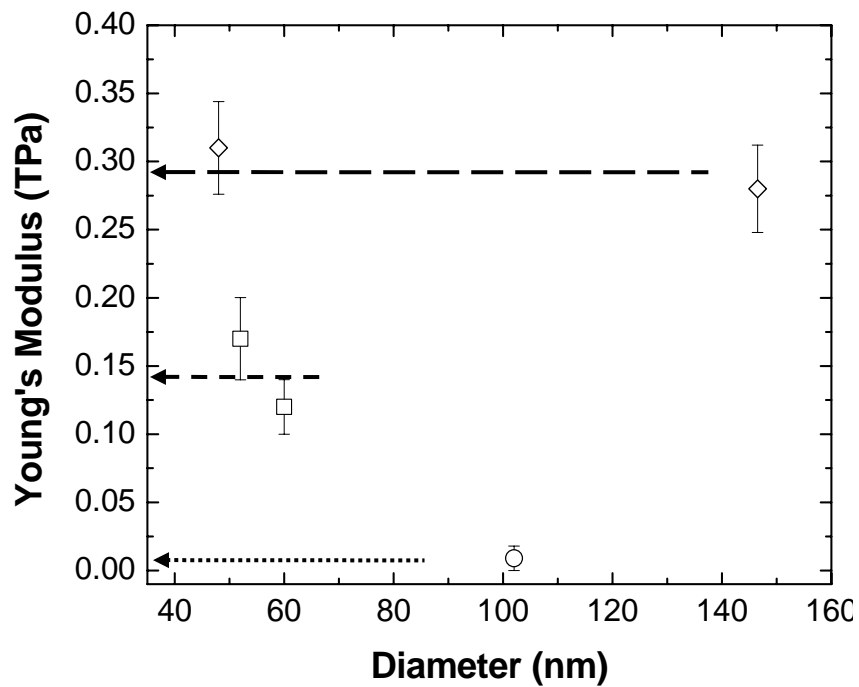
Figure 3.4: Defect dependent Young's modulus of CVD grown MWNTs. The melamine grown nanotubes are found to have the small modulus.

give a lower E. This shows that the defects in the nanotubes play a dominant role in determining the Young's modulus of an individual CVD grown MWNT as measured by bending. It should be mentioned that, in general, Young's modulus is not a structure sensitive property, so that, for example, single crystal Fe has about the same E as lightly doped polycrystalline Fe. Perhaps the effects of these defects extend across the full coss-section of the nanotube, whereas in bulk samples small defects have only localized effects.

3.3.2   Resistivity measurements

The room temperature resistivity of the samples was also measured as a function of length for each nanotube (Fig. 3.6). Individual MWNTs were extracted with a gold coated tungsten tip and a second gold coated tungsten tip was manipulated to contact the nanotube at different distances from the first tungsten tip. The IV measurements were recorded using a Keithley 2400 SMU and the nanotube resistance R determined from the slope of the IV data. TEM images were then obtained for each nanotube to provide the geometric values needed for calculating the resistivity. In agreement with the TEM data with respect to defect density, the xylene/ferrocene/melamine derived nanotubes showed highest resistivity while the xylene/ferrocene/trimethylamine derived tubes showed the least resistivity. Finally, it should be mentioned that the contact resistance in these measurements was about 5 kΩ, which was at least a factor of 5 below the resistance of the nanotubes. The contact resistance was determined by extrapolating the R data set to the zero inter-electrode distance (inset in Fig. 3.6).
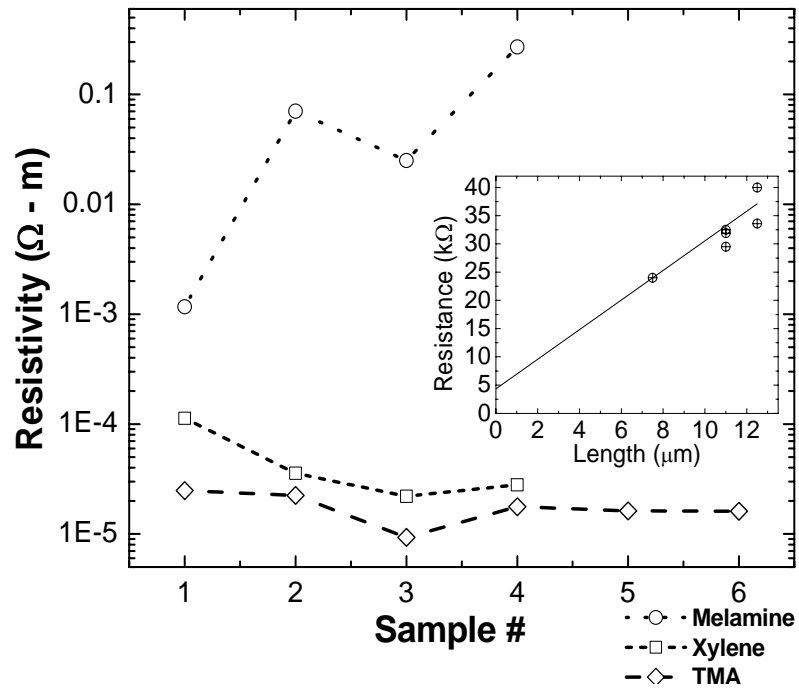
Figure 3.5: Resistivity of individual MWNTs. The structural perfection of each type of nanotube is directly related to its electrical resistivity. This graph confirms that the resistivity does correlate with the structural defects observed in the TEM. The y-intercept of the inset figure is 4.2 kΩ, which gives the value of the contact resistance between the nanotube and the gold contact.

3.4 Conclusions

In conclusion, we have shown that the Young's modulus can be measured in individual MWNTs by electrostatically driving it into resonance and the defects in the nanotubes play a dominant role in determining its Young's modulus as measured by bending.

CHAPTER 4

ELECTRICAL DETECTION OF OSCILLATIONS IN MICRO- AND NANO-

CANTILEVERS

4.1 Introduction

Precise determination of the resonant frequency, phase and quality factor in micro- and nano-mechanical oscillators would permit, among other things, (i) the detection of trace amounts of adsorbed molecules through a shift in the resonant frequency, and (ii) pressure variations in the environment which affect the mechanical damping of the oscillator. The major difficulty in making these measurements in many cases is the ancillary equipment such as lasers or high magnetic fields that must be used. Being able to make precise measurements with a fully electrical actuation and detection method would greatly extend the usefulness of these oscillators. Detecting the oscillation through changes in the capacitance between the oscillator and a counter electrode is difficult because the static capacitance between them as well as the parasitic capacitance of the rest of the circuitry overwhelm the detection. We have found that the charge on a micro- or nano- cantilever when driven by a nearby counter electrode contains higher harmonics of the driving signal with appreciable amplitude. This allows detection at frequencies well removed from the driving frequency, which increases the signal-to-background ratio, SBR, by ~ 3 orders of magnitude. This chapter details clear electrical detection of mechanical oscillations in ambient conditions for two systems: Si-based

micro- and MWNT based nano-cantilevers [38].

Micro- and nano-cantilevers have been proposed for measuring mass, adsorbents, viscosity, etc., as well as acting as resonators [2, 22, 39]. Electrically induced mechanical oscillations in such cantilevers have been recorded using *non-electrical* detection methods that involve the use of a transmission electron microscope [17], scanning electron microscope [18], field emission microscope [19], or an optical microscope [20, 21]. For the applications mentioned above, the resonating system must be *portable* and therefore a capacitive readout of the mechanical motion is ideal. As pointed out previously [24], sensing motion through dynamic changes of capacitance in MEMS and NEMS is difficult because this dynamic signal is obscured by parasitic capacitances that are many orders of magnitude larger. Techniques for avoiding this problem, such as single electron transistors [33], often involve low temperatures. Sensing elements such as comb drives along with on-chip circuitry have been added to many micro/nano- fabricated silicon-based NEMS/MEMS resonators to overcome the parasitics [23, 34]. These systems involve intricate multi-element designs which may increase the cost of production and probability for breakdown. Accordingly, individual cantilever structures which make up the simplest MEMS/NEMS structures that can be easily machined and mass produced [40] would be ideal. Here we show that the charge on a micro- or nano-cantilever when driven by a nearby counter electrode can have a rich harmonic structure. *Measuring these harmonics avoids the parasitic capacitance problem.* We show that this enables easy determination of the resonance frequency of individual micro- and nano- cantilevers with a substantial signal to background ratio.

4.2   Harmonic Detection of Resonance (HDR)

In our studies, we manipulate a cantilever over a dark field microscope as reported previously [21]. In most cases, this allows for simple manipulation of the cantilever near the counter electrode without the need for time consuming lithographic processes. We define a cantilever to be either a silicon microstructure shaped like a diving board, or a cantilevered multi-walled carbon nanotube (MWNT). We place the cantilever parallel to and within 1-10 μm from a counter electrode depending on its dimensions. It is forced into resonance by applying an ac voltage (V_{ac}) with a dc offset (V_{dc}) on the counter electrode under ambient conditions [21]. An electrical readout system electrostatically actuates the cantilever and measures the electrical signal due to the modulated charge created by the dynamic capacitance as well as the applied ac electrostatic driving signal. Our system consists of an A250 charge amplifier, an oscillator, a dc power supply, and a lock-in amplifier (Fig. 4.1). We also employ a localized Faraday cage (Fig. 4.1), which surrounds the metal contact for the counter electrode and extends around the probe tip leaving about 2 mm of the tip exposed. This avoids crosstalk between the metal contacts which hold the cantilever and the counter electrode. It helps to increase the signal to background ratio SBR for the cantilever and is crucial when working at the nanoscale. The lock-in amplifier detects the output of the A250 at a harmonic of the oscillator frequency. As described below, harmonics of the applied ac voltage are essential to our method, which is henceforth referred to as the *harmonic detection of resonance* (HDR) method.
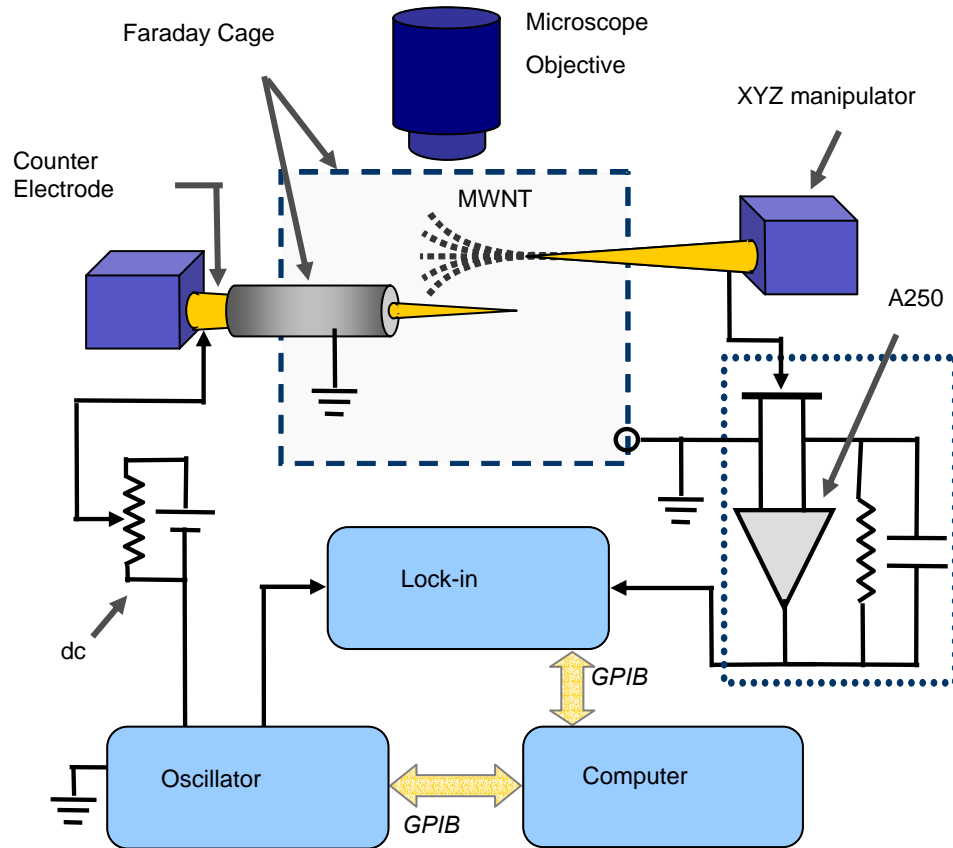
Figure 4.1. A schematic of our setup for the harmonic detection of resonance (HDR) in micro- or nano-sized cantilevers. The excitation voltage from the oscillator and dc source applied to the counter electrode drives the MWNT into oscillation. The induced charge on the cantilever is amplified by the A250 which feeds an oscillating voltage to the lock-in amplifier. The lock-in is set to measure a harmonic of the oscillator frequency.

4.3 Theory of modulated charge

The total voltage applied to the counter electrode is $V(t) = V_{dc} + V_{ac}\cos(\omega t)$, where the V_{dc} term includes the difference between the work potentials of the cantilever and counter electrode. Let $C(t)$ be the capacitance between the cantilever and the counter electrode. The electrostatic energy of the system is then $\frac{1}{2}CV^2$, and the force on the cantilever is $F_c = -\frac{1}{2}\frac{d(CV^2)}{dx} = -\frac{1}{2}V^2\frac{dC}{dx}$. If the vibration amplitude $y(t)$ of the cantilever is small compared to the distance between the cantilever and the counter electrode, then $C(t) \approx C_0 + \frac{dC}{dx}|_{x=0}\, y(t)$, where C_0 and $\frac{dC}{dx}|_{x=0} = -C_0'$ are constants for a given experimental set up. Thus for small deflections, the Coulomb force on the cantilever is

$$\begin{aligned} F_c &= \tfrac{1}{2}C_0'(V_{dc} + V_{ac}\cos(\omega t))^2 \\ &= \tfrac{1}{2}C_0'\{(V_{dc})^2 + 2(V_{dc})V_{ac}\cos(\omega t) + \frac{1}{2}V_{ac}^2[1 + \cos(2\omega t)]\} \end{aligned}$$

(4.1)

implying that the cantilever can be viewed as a forced harmonic oscillator driven by a force with two time varying components: $\cos(\omega t)$ and $\cos(2\omega t)$. When the frequency of the applied voltage ω is close to a normal mode frequency ω_0 of the free cantilever, and the damping γ is small, the steady state solution for $y(t)$ is

$$y(t) = \frac{QC_0'V_{dc}V_{ac}\cos(\omega t - \phi_1)}{k'\sqrt{Q^2[1-(\frac{\omega}{\omega_0'})^2]^2 + \frac{\omega^2\omega_0^2}{\omega_0'^4}}}, \quad \tan\phi_1 = \frac{\omega_0'\omega}{Q(\omega_0'^2 - \omega^2)}$$

(4.2)

where $\omega_0'^2 = \frac{k'}{m}$, $k' = k - \frac{dF_c}{dx}$, m is the inertial term of the vibrational mode, k the spring constant of the cantilever, and $Q = \gamma/(\omega_0 m)$ the quality factor of the mode in the environment of the experiment [25]. The electrostatic correction term $\frac{dF_c}{dx}$ is usually small, so that ω_0' is not very different from ω_0. Since F_c also has a term that oscillates

at 2ω, when 2ω is close to ω_0 a similar analysis gives:

$$y(t) = \frac{QC_0'V_{ac}^2 \cos(2\omega t - \phi_2)}{4k'\sqrt{Q^2[1-(\frac{2\omega}{\omega_0'})^2]^2 + \frac{4\omega^2\omega_0^2}{\omega_0'^4}}} \quad , \qquad \tan\phi_2 = \frac{2\omega_0\omega}{Q(\omega_0'^2 - 4\omega^2)} \tag{4.3}$$

Since $q(t) = C(t)V(t)$, to first order in $x(t)$ and for ω near ω_o, we obtain for the time dependent part of q (t)

$$q(t) = \left[C_0 - \frac{QC_0'^2 V_{dc}V_{ac}\cos(\omega t - \phi_1)}{k'\sqrt{Q^2\left[1-(\omega/\omega_0')^2\right]^2 + \omega^2\omega_0^2/\omega_0'^4}} \right][V(t)] = \left[C_0 - K_1 V_{dc}V_{ac}\cos(\omega t - \phi_1)\right]\left[V_{dc} + V_{ac}\cos(\omega t)\right] \tag{4.4}$$

where

$$K_1 = \frac{QC_0'^2}{k'\sqrt{Q^2\left[1-\left(\frac{\omega}{\omega_0'}\right)^2\right]^2 + \frac{\omega^2\omega_0^2}{\omega_0'^4}}} \qquad \omega \text{ near } \omega_0. \tag{4.5}$$

Since

$$K_1 V_{dc}V_{ac}^2 \cos(\omega t - \phi_1)\cos(\omega t) = \frac{K_1 V_{dc}V_{ac}^2}{2}\left[\cos(2\omega t - \phi_1) + \cos(\phi_1)\right] \tag{4.6}$$

the charge can be written as:

$$q(t) = C_0 V_{dc} - \frac{K_1 V_{dc}V_{ac}^2}{2}\cos(\phi_1) + C_0 V_{ac}\cos(\omega t) - K_1 V_{dc}^2 V_{ac}\cos(\omega t - \phi_1) - \frac{K_1 V_{dc}V_{ac}^2}{2}\cos(2\omega t - \phi_1) \tag{4.7}$$

Following a similar rationale for 2ω near ω_o (or ω near $\omega_o/2$) the charge can be written as:

$$q(t) = \left[C_0 - \frac{QC_0'^2 V_{ac}^2 \cos(2\omega t - \phi_2)}{4k'\sqrt{Q^2\left[1-(2\omega/\omega_0')^2\right]^2 + 4\omega^2\omega_0^2/\omega_0'^4}} \right][V_{dc} + V_{ac}\cos(\omega t)] =$$

$$\left[C_0 - K_2 V_{ac}^2 \cos(2\omega t - \phi_2)\right]\left[V_{dc} + V_{ac}\cos(\omega t)\right] \tag{4.8}$$

where

$$K_2 = \cfrac{QC_0'^2}{4k'\sqrt{Q^2\left[1-\left(\cfrac{2\omega}{\omega_0'}\right)^2\right]^2 + \cfrac{4\omega^2\omega_0^2}{\omega_0'^4}}} \qquad \omega \text{ near } \omega_0/2. \qquad (4.9)$$

Since

$$K_2 V_{ac}^3 \cos\left(2\omega t - \phi_2\right)\cos\left(\omega t\right) = \frac{K_2 V_{ac}^3}{2}\left[\cos\left(3\omega t - \phi_2\right) + \cos\left(\omega t - \phi_2\right)\right] \qquad (4.10)$$

the charge $q(t)$ can be expressed as

$$q(t) = C_0 V_{dc} + C_0 V_{ac}\cos\left(\omega t\right) - \frac{K_2 V_{ac}^3}{2}\cos\left(\omega t - \phi_2\right) - K_2 V_{ac}^2 V_{dc}\cos\left(2\omega t - \phi_2\right) - \frac{K_2 V_{ac}^3}{2}\cos\left(3\omega t - \phi_2\right) \qquad (4.11)$$

One can see that multiplication of the driving frequency by the resulting oscillations of the cantilever provides automatic up-conversion of the input frequency. For example, when the applied ac voltage $V(t)$ oscillates at an angular frequency ω that is close to $\omega_0/2$, the resulting charge oscillation $q(t)$ has Fourier components not only at ω, but also at 2ω and 3ω.

4.4   Resonant detection using HDR

4.4.1   Higher harmonics

In Fig. 4.2, we present typical data recorded by our system for a commercially available tipless Al coated silicon cantilever whose cataloged resonant frequency $\omega_0 \sim 30$ kHz (Mikro Masch).   In all cases, measurements were taken at atmospheric pressure and room temperature. For this cantilever, our measurements show the resonance to occur at 28.6 kHz. When measuring at the higher harmonics, we found resonant peaks to occur at both ω_0 and $\omega_0/2$. It must be made clear in this case that we are measuring only the first

(fundamental) mode of the cantilever and its higher harmonics and a super harmonic ($\omega_0/2$) and its higher harmonics. Notice that any resonance detected at the first harmonic is overwhelmed by the background signal due to the parasitic capacitance (—□— in Fig. 4.2a). There is an obvious signal at the second harmonic (—△— in Fig. 4.2a), and a smaller signal at the third harmonic (—○— in Fig. 4.2a) at $\omega_0/2 \sim 14.5$ kHz. The response of the system when the driving frequency ω is equal to $\omega_0 \sim 28.6$ kHz is larger for all harmonics. Thus, if the output signal of the A250 is detected at the second or third harmonic instead of at the driving frequency, the signal stemming from the parasitic capacitance is *avoided,* permitting the detection of ω_0 with a superior SBR. Weak peaks present between $\omega_0/2$ and ω_0 are attributed to residual extraneous electrical pick-up. We note that our theory predicts a resonant peak for all three harmonics at $\omega_0/2$ (Eqn. 4.11), and a peak for only the first two harmonics at ω_0 (Eqn. 4.7). We attribute the lack of an observable signal at the first harmonic at $\omega_0/2$ to the presence of a relatively large masking signal from the parasitic capacitance. Furthermore, the presence of a third harmonic signal at ω_0 is attributed to higher order terms that we have neglected in our theory above. These terms involve higher order derivatives of the capacitance with respect to the separation of the cantilever and the counter electrode which will be treated in Chapter 6.

4.4.2 Quality factor (Q) and signal-to background ratio (SBR)

In Fig. 4.2a, each linewidth at ω_0 decreases with each higher harmonic, particularly from the 2nd to 3rd harmonic. We believe this is due to the much lower background signal at the higher harmonics, which comes from experiencing less parasitic

(a)

(b)

48
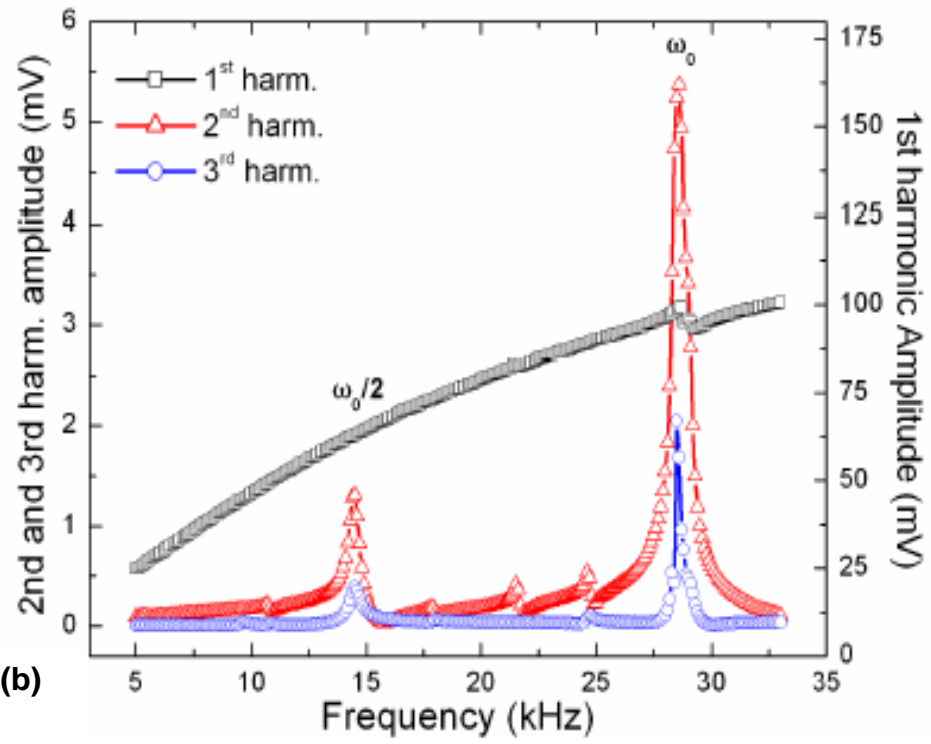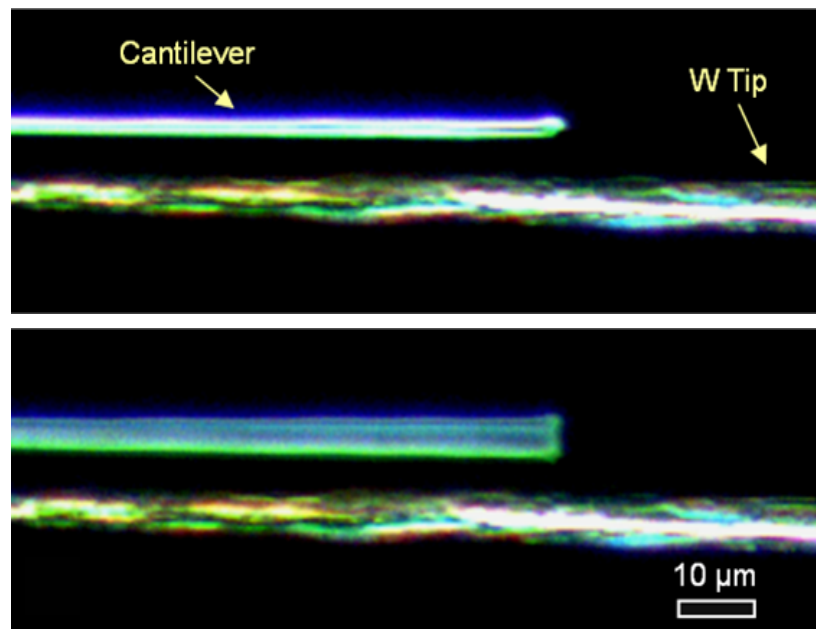
Figure 4.2. (a) The amplitude signal from the lock-in amplifier when set to the 1st, 2nd and 3rd harmonics of the oscillator output for a tipless silicon cantilever (250 μm long, 35 μm wide, and 2 μm thick). The 1st harmonic has a background that gradually increases with the oscillator frequency ω and shows a small peak when $\omega = \omega_0 = 28.6$ kHz, the resonance frequency of the cantilever. Most of this background comes from the parasitic capacitance. The 2nd and 3rd harmonic signals exhibit higher signal to background ratios making them suitable for highly sensitive detection of ω_0. The peak at $\omega_0/2$ for the 2nd and 3rd harmonic is at 14.5 kHz. (b) Typical dark field optical microscope image of a tipless silicon cantilever in (bottom) and out (top) of resonance. We estimate the amplitude to be ~ 1/10 the thickness of the cantilever or about 0.2μm. For clarity, the cantilever was driven into resonance using a larger voltage than used in any of our electrical measurements.

pickup, as we measure further from the driving frequency. To quantify the sharpness of the resonant peak at ω_0 measured at higher harmonics, we define an *effective* quality factor $Q_{eff} \equiv f_0/\Delta f$, where Δf is the FWHM, full width at half maximum, of the resonant peak in the frequency domain. At ω_0, Q_{eff} changes from 40 to 120 for the 2nd and 3rd harmonics respectively. Since the influence of the background signal is small at higher harmonics, it is advantageous to evaluate the SBR at ω_0, which we define as $\Delta S/ S_{baseline} = (S_{peak\ max} - S_{baseline})/ S_{baseline}$. For the sample in Fig. 4.2, the SBR at ω_0, is 0.065 for the first harmonic, 45 for the second, and 56 for the third. It is clear that we obtain a SBR almost 3 orders of magnitude better by measuring at higher harmonics.

4.4.3   Amplitude and phase

In another measurement, we determined the resonance spectrum and phase for a different Si micro-cantilever. Figure 4.3 shows that the amplitude peak is accompanied by a phase change of ~180^0. Ideally, we expect a 180^0 phase change, as discussed in eqns. (4.2) and (4.3). The ω_0 of the system can be tuned by V_{ac} and V_{dc} without appreciable change in Q_{eff}. A decrease in ω_0 is observed when the ac voltage is increased (inset figure in Fig. 4.3). This decrease is due to a softening in the effective spring constant of the system from k to k' where $k' = k - \frac{dF_c}{dx}$ [25], where

$$\frac{dF_C}{dx} = -\frac{1}{2}\left[\frac{d^2C}{dx^2}\right]_{x=0} \{V_{dc}^2 + 2V_{dc}V_{ac}\cos(\omega t) + \frac{1}{2}V_{ac}^2[1+\cos(2\omega t)]\}. \qquad (4.12)$$

The time dependent terms will average out so that the resulting change in the observed frequency is proportional to the second derivative of the capacitance of the system with respect to x, and to $[V_{dc}^2 + \frac{1}{2}V_{ac}^2]$. We find that there is a decrease in the resonance

frequency as V_{ac} is varied (inset figure in Fig. 4.3), in agreement with this treatment. It is difficult to define the capacitance of our system well enough to calculate d^2C/dx^2. This is because the diameter of the tungsten needle used as a counter electrode and the placement of the cantilever with respect to the counter electrode are not known well enough to compare experiment to theory quantitatively.

4.4.4 HDR versus AFM

Using another Si cantilever, we compare in Fig. 4.4 the resonant frequency obtained from the HDR system to that determined from a well-established optical technique which is routinely used in atomic force microscopy (Veeco di-CP II). The agreement between the AFM and HDR measurements is a further indication of the efficacy of our HDR technique. For the cantilever in Fig. 4.4, we obtain a quality factor of Q_{eff} = 200 for 2nd harmonic detection of the fundamental mode frequency, which should be compared to 60 obtained using laser detection. When the resonance spectrum is obtained with the AFM, the excitation is applied by a piezoelectric source, and hence no peak at $\omega_0/2$ is seen in the AFM data. The small differences in the resonance frequencies are attributed to differences in the excitation methods, piezoelectric vs. electrostatic. As mentioned above, our resonant peak is slightly downshifted; an effect not present if the resonance is excited by the vibrations of a piezoelectric mount. One method to obtain a more accurate value of the resonance is to extrapolate the peak in the resonance curve as a function of applied voltages to zero ac and dc voltages [23].
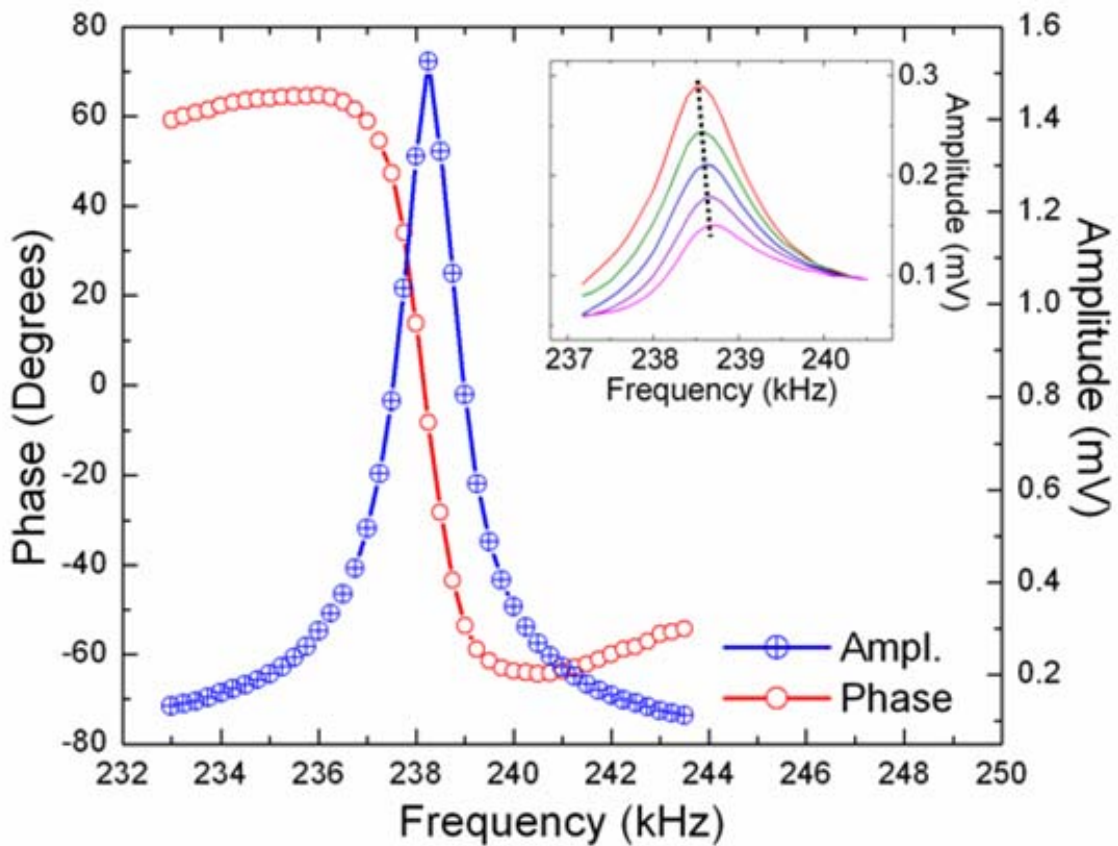
Figure 4.3: The amplitude and phase measured by our HDR system for a cantilever (110 μm long, 35 μm wide and 2 μm thick). As expected, the phase decreases by ~180⁰ around resonance. The inset shows the downshift in resonance frequency with no significant change in Q_{eff} as the ac voltage is varied from 3 (violet, bottom) to 5 (red, top) volts in 0.5 V increments. This shift is caused by the decrease in the effective spring constant as the ac voltage is increased. The black dashed line is a guide to the eye.
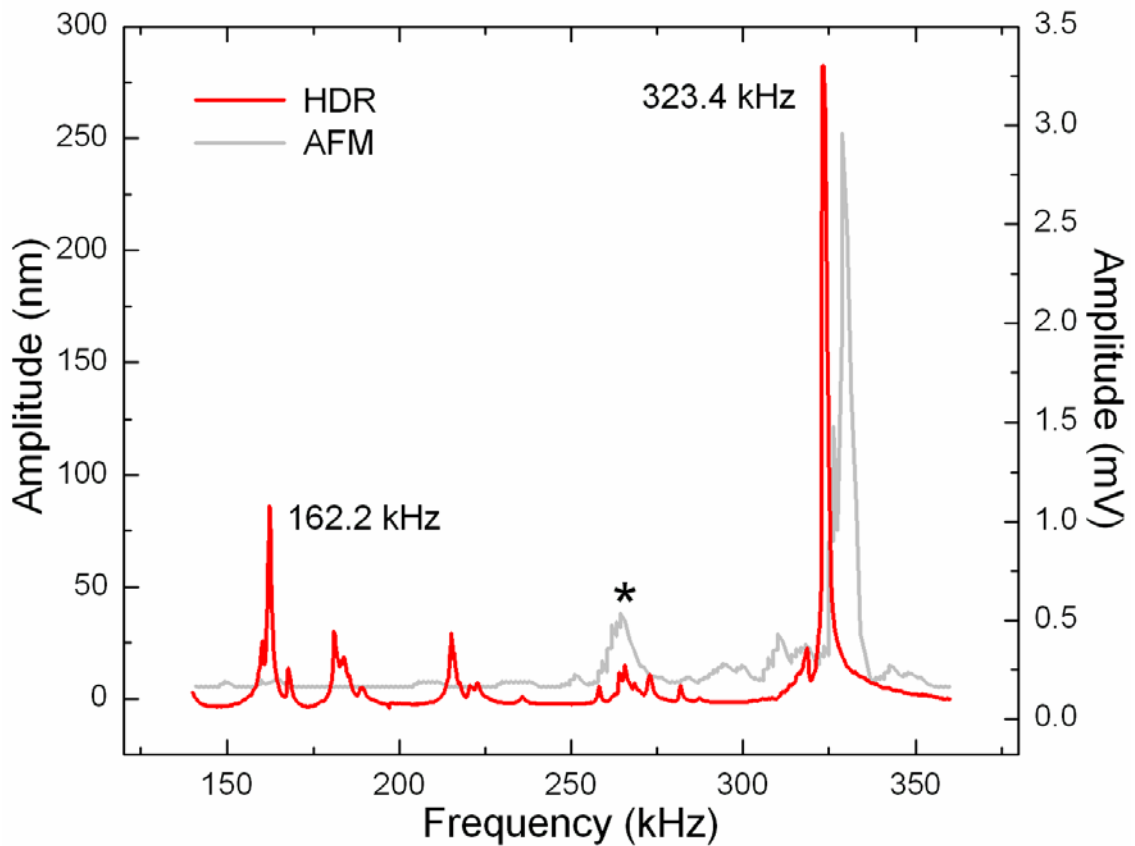
Figure 4.4: Resonance spectra for a Si cantilever (90 μm long, 35 μm wide and 2 μm thick), measured using a conventional AFM (grey) and with our HDR system (black) at the second harmonic. The prominent peaks near ~323 kHz due to the spring softening of the cantilever with voltage, spectrum since the AFM correspond to the natural frequency ω_0 of the cantilever. Notice that the large peak present at $\omega_0/2$ ~162 kHz in the black spectrum is absent in the gray, which uses a piezoelectric driver and has no excitation at $\omega_0/2$. The resonant frequency measured by our HDR system is slightly lower than that measured by the AFM. This is a result of a small decrease in the effective spring constant due to the applied electrostatic field. The peak indicated by the * corresponds to a peak also observed in the AFM spectrum.

4.4.5   Voltage effects on the frequency, amplitude, and phase

In this section, the effects of ac and dc voltage on the resonance will be presented. We can start by looking at how the ac voltage changes the frequency spectrum for the peaks at ω_0 and $\omega_0/2$, as well as the false peaks, which in this case, is good for the discussion. As a note, for any sections or chapters after this section, the noise that caused the false peaks was eliminated, but for ac and dc dependence measurements, they inadvertently serve as a guide to compare to the real peaks.

Figure 4.5 shows a spectrum from 0-50 kHz, where the ac voltage was changed from 3 to 5 volts. This image mostly serves as a full look of the spectrum. A measurement was also taken on a shorter cantilever which is used to indicate where the false peaks occur (Fig. 4.6). Notice that the amplitudes of the false peaks are approximately the same for both scans, but the amplitudes at ω_0 and $\omega_0/2$ are different. We expect to have smaller amplitudes for the shorter cantilevers since both the amplitude of vibration and the overlap between the cantilever and counter electrode is smaller. Figures 4.7 and 4.8 give a closer view for ω_0 and $\omega_0/2$ respectively. Notice that at 3 V_{ac}, the resonance of the ω_0 and $\omega_0/2$ peaks have a 24.36**:**12.22 or 1.993:1 relationship, but at 5 V_{ac} they have a 24.22**:**12.17 or a 1.990**:**1 ratio. Theoretically, the relationship should be 2**:**1. It seems that this ratio may reach the theoretical value at very low excitation or a larger gap distance between the cantilever and counter electrode where additional nonlinearities begin to disappear. One way to look at the how the frequency shift should react due to spring softening is to compare equation (4.12) with the data qualitatively. Let's evaluate equation (4.12) as V_{ac} changes for both ω_0 and $\omega_0/2$. To start with we know that $k \propto \omega_0^2$ where any mass or effective mass would cancel below. From equation
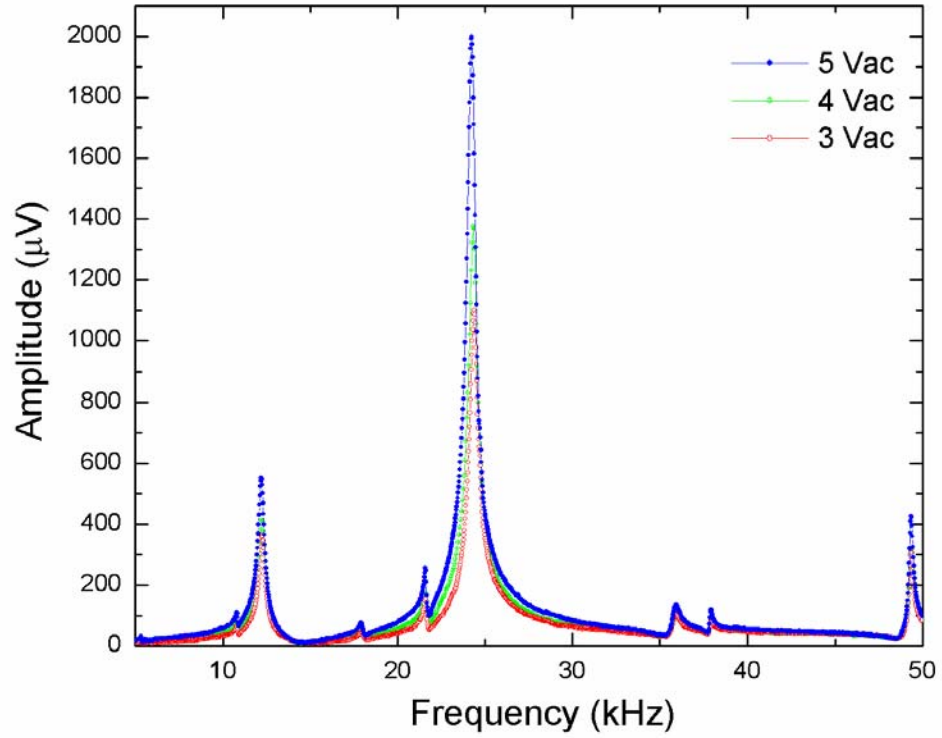
Figure 4.5: Frequency-amplitude spectrum for a tipless silicon cantilever (350 μm long, 35 μm wide, and 2 μm thick). Large peaks are observed at ~12 kHz, ~25 kHz, and ~49 kHz.
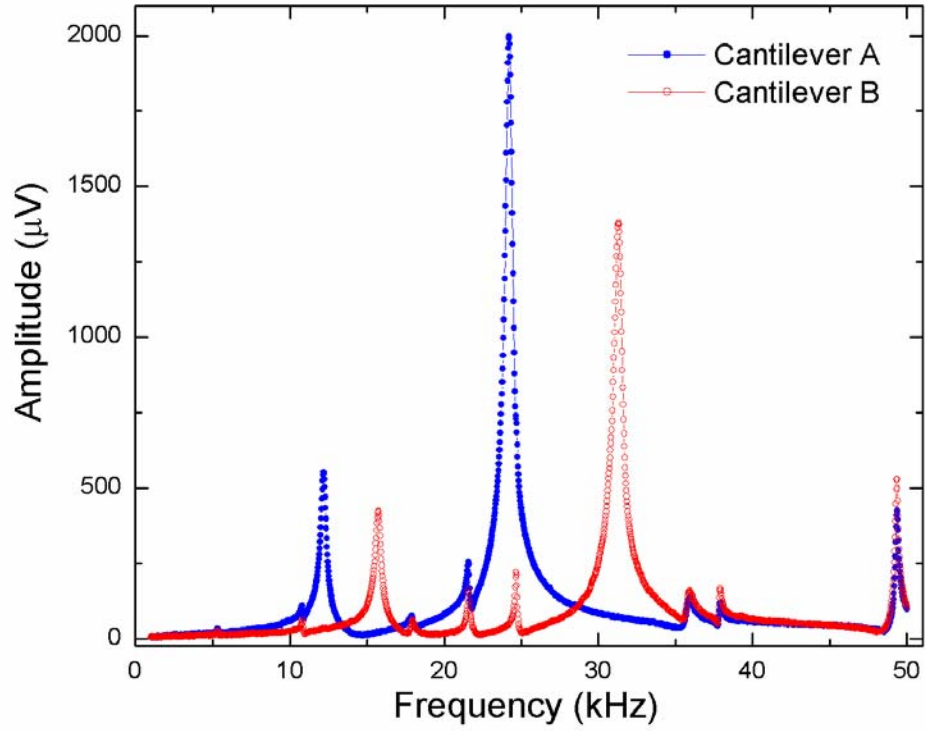
Figure 4.6: 2nd harmonic frequency-amplitude spectra for two silicon cantilevers with dimensions 350 μm long, 35 μm wide, and 2 μm thick (blue trace, closed circles) and 300 μm long, 35 μm wide, and 2 μm thick (red trace, open circles).

Figure 4.7: Ac voltage change from 3 to 5 V_{ac} at ω_0. The resonant peak is at 24.4 kHz for 3 V_{ac}. This peak at ω_0 shows a considerable change in a downshift in the frequency as the ac voltage is increased. The phase in each curve gives a better indication of the shift.

Figure 4.8: Ac voltage change from 3 to 5 V_{ac} at $\omega_0/2$. The resonant peak is at 12.2 kHz for 3 V_{ac}. This peak at $\omega_0/2$ shows less of a change in a downshift in the frequency as the voltage is increased compared to ω_0.

(4.12), the percent difference from 3 to 5 V_{ac}, while using 8 V_{dc}, for the value of the associated terms for ω_0 and $\omega_0/2$ is as follows:

at ω_0 ; $\quad \dfrac{V_{dc}V_{ac1} - V_{dc}V_{ac2}}{V_{dc}V_{ac1}} \times 100\% = \dfrac{(8)(5)-(8)(3)}{(8)(5)} \times 100\% = \dfrac{2}{5} \times 100\% = 40\%$

at $\dfrac{\omega_0}{2}$; $\quad \dfrac{V_{ac1}^2 - V_{ac2}^2}{V_{ac1}^2} \times 100\% = \dfrac{(5)^2-(3)^2}{(5)^2} \times 100\% = \dfrac{16}{25} \times 100\% = 64\%$

From this we can just say, qualitatively, that the spring constant should soften more due to an increase in ac voltage at $\dfrac{\omega_0}{2}$ according to equation (4.12). Evaluating the data at ω_0 and $\omega_0/2$ in the same way but for ω_0^2 we get

at ω_0

$$\frac{\omega_0^2(3Vac) - \omega_0^2(5Vac)}{\omega_0^2(3Vac)} \times 100\% = \frac{(24.36)^2 - (24.22)^2}{(24.36)^2} \times 100\% = \frac{6.8}{593.4} \times 100\% = 1.1\%$$

and at $\dfrac{\omega_0}{2}$

$$\frac{\dfrac{\omega_0^2}{2}(3Vac) - \dfrac{\omega_0^2}{2}(5Vac)}{\dfrac{\omega_0^2}{2}(3Vac)} \times 100\% = \frac{(12.22)^2 - (12.17)^2}{(12.22)^2} \times 100\% = \frac{1.22}{149.3} \times 100\% = 0.8\% \cdot$$

So we expect the $\omega_0/2$ effects to be greater than for ω_0. It seems that the peak at ω_0 is affected by something else. Most likely, the reason is that since the cantilever's deflection amplitude at ω_0 is much larger than at $\omega_0/2$, making nonlinearities in the vibration, which includes the Duffing effect, play a greater role on ω_0. However, as indicated by the shift in phases in Fig. 4.7, the curve does downshift, a characteristic not indicative of Duffing. Figure 4.9 shows a peak leaning past its midpoint due to Duffing nonlinearities. The shift

may come from the quadratic terms in the spring constant. By observing the phase, Fig. 4.10 shows a transition from linear effects to nonlinear effects where the Duffing begins to dominate. The idea here is that by changing the ac voltage, we must be careful not to assume that a shift in resonance is solely due to linear spring softening or hardening.

Two of the false peaks from Fig. 4.5 are shown in Fig. 4.11. There is no noticeable shift in the peaks. This indicates that for measurements taken with HDR, we can trust that a shift in resonance with ac voltage is a good indication that we are looking at a real peak.

Next we can investigate how the dc voltage affects the resonance. For an electrostatic system, the dc voltage is generally referred to as the polarization voltage. It deflects the position of the cantilever to a new equilibrium position, while the ac component vibrates the cantilever around this position. Figure (4.12) shows a full spectrum for 3 and 5 dc volts. As has been seen in many other experiments in our lab with different gap distances and overlaps, the dc voltage considerably increases the amplitude of the signal as more than the ac voltage at the second harmonic. For the amplitudes with the ac spectrum and comparing 5 V_{ac} to 3 V_{ac}, there is a 45% change at ω_0, a 34.5% change at $\omega_0/2$, and a 24.5% change for the false peaks. Now for the amplitudes of the dc spectrum, we have a 64% change at ω_0, a 65% change at $\omega_0/2$, and a 73% change for the false peaks. This shows that a change in the dc voltage seems to have a greater affect on the amplification over the full spectrum and particularly at resonance as compared to ac amplification.
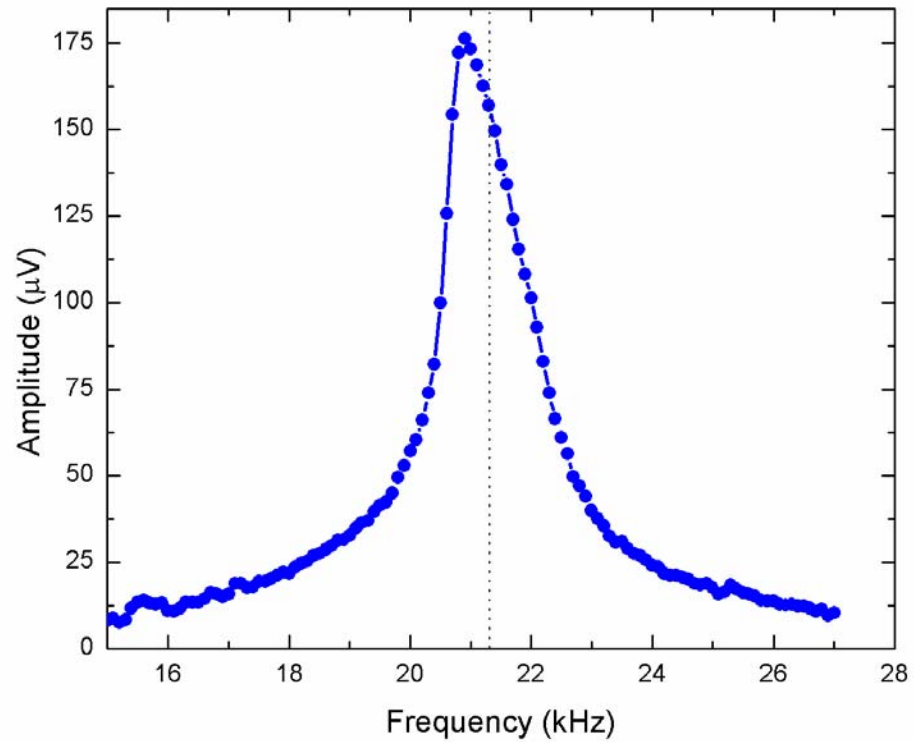
Figure 4.9: Experimental data showing the peak leaning over due to the Duffing effect. In this experiment, the overlap between the cantilever and counter electrode is much less than for previous measurements, attributing to the lower signal. The cantilever was placed close to the counter electrode giving it a large amplitude of vibration. The dashed line serves as a guide for the eye.
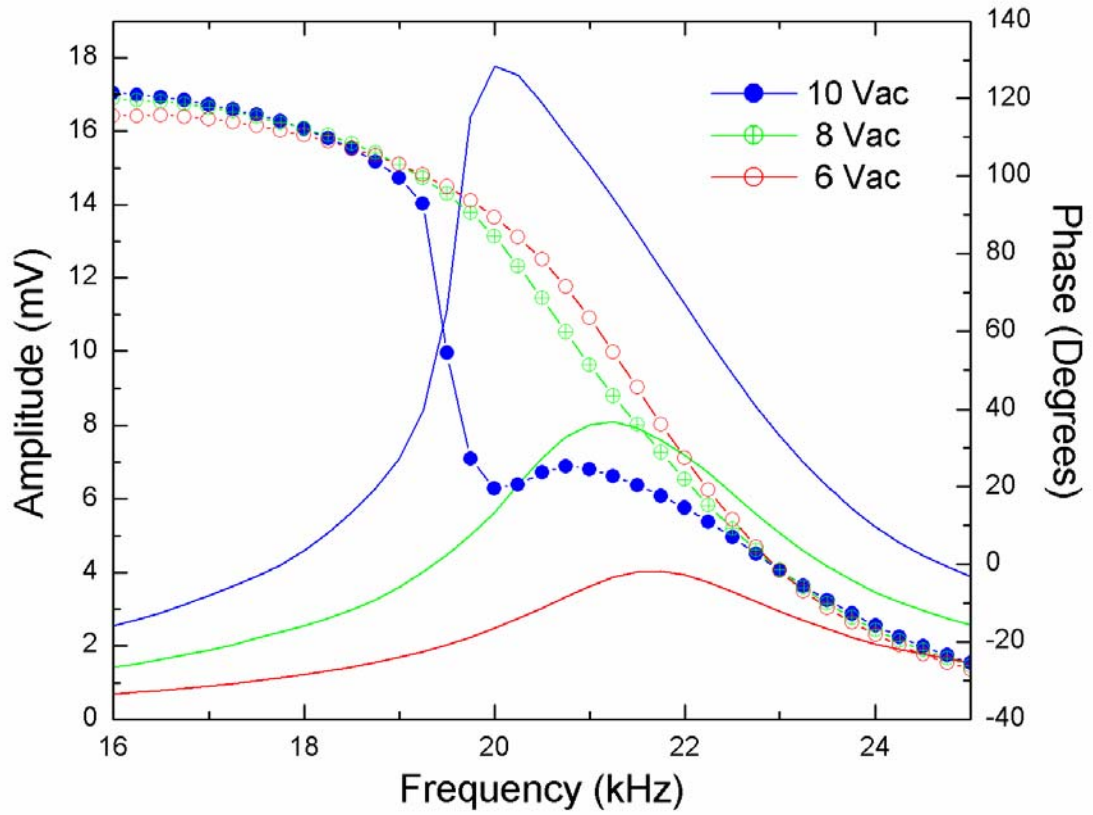
Figure 4.10: This graph shows the relationship with the Duffing effect and phase. The sudden change in phase at 10 V_{ac} indicates a transition of the cantilever's motion into the nonlinear regime.
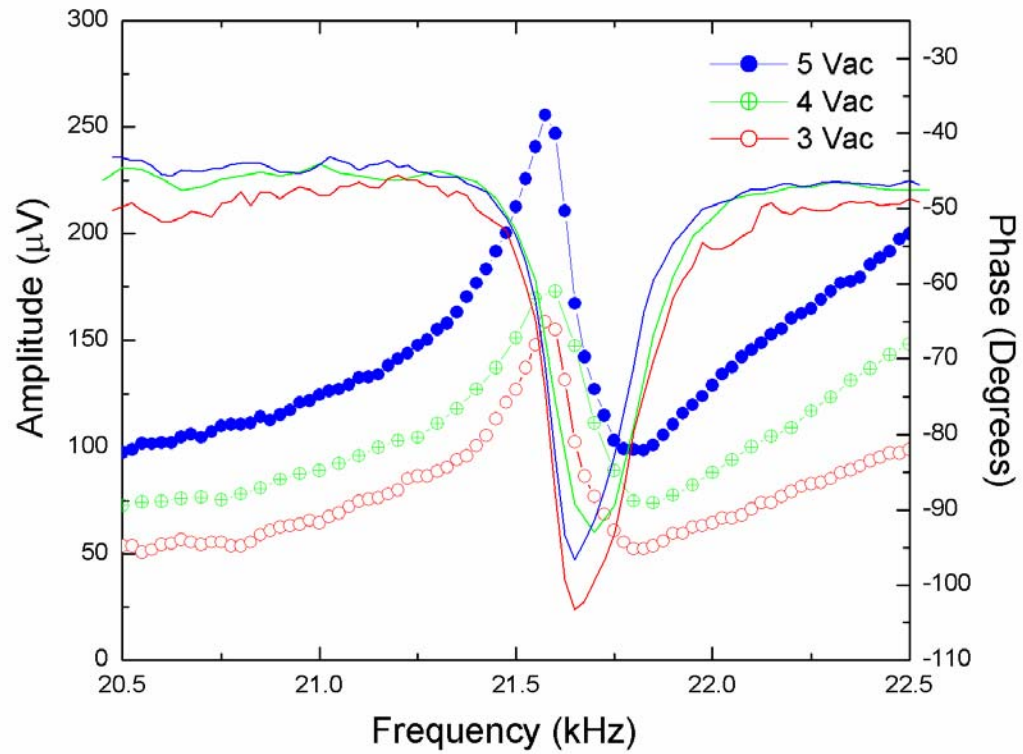
Figure 4.11: False peaks from the data shown in Fig. 4.5. Notice the lack of a downshift in frequency and phase with the change in ac voltage.

According to equation (4.13), the *linear* spring constant is not changed by the dc voltage at $\omega_0/2$. The dc voltage, however, may in fact change due to the *nonlinear* terms in the spring constant. To investigate this, we can follow equation (2.47) where we can absorb the nonlinear terms into the spring constant as follows

$$m\frac{\partial^2\zeta}{\partial t^2}+\gamma\frac{\partial\zeta}{\partial t}+\kappa\zeta+\lambda\frac{\partial^3 C}{\partial\zeta^3}\Big|_{y=y'}\zeta^2+\lambda\frac{\partial^4 C}{\partial\zeta^4}\Big|_{y=y'}\zeta^3+...\lambda\frac{\partial^n C}{\partial\zeta^n}\Big|_{y=y'}\zeta^n$$
$$=\Big[V_{dc}V_{ac}\cos(\omega t)+\tfrac{1}{2}V_{ac}^2\cos(2\omega t)\Big]\frac{\partial C}{\partial\zeta}\Big|_{y=y'} \tag{4.13}$$

$$m\frac{\partial^2\zeta}{\partial t^2}+\gamma\frac{\partial\zeta}{\partial t}+\left(\kappa+\lambda\frac{\partial^3 C}{\partial\zeta^3}\Big|_{y=y'}\zeta+\lambda\frac{\partial^4 C}{\partial\zeta^4}\Big|_{y=y'}\zeta^2+...\lambda\frac{\partial^n C}{\partial\zeta^n}\Big|_{y=y'}\zeta^{n-1}\right)\zeta$$
$$=\Big[V_{dc}V_{ac}\cos(\omega t)+\tfrac{1}{2}V_{ac}^2\cos(2\omega t)\Big]\frac{\partial C}{\partial\zeta}\Big|_{y=y'} \tag{4.14}$$

setting

$$\kappa'=\left(\kappa+\lambda\frac{\partial^3 C}{\partial\zeta^3}\Big|_{y=y'}\zeta+\lambda\frac{\partial^4 C}{\partial\zeta^4}\Big|_{y=y'}\zeta^2+...\lambda\frac{\partial^n C}{\partial\zeta^n}\Big|_{y=y'}\zeta^{n-1}\right) \tag{4.15}$$

we get

$$m\frac{\partial^2\zeta}{\partial t^2}+\gamma\frac{\partial\zeta}{\partial t}+\kappa'\zeta=\Big[V_{dc}V_{ac}\cos(\omega t)+\tfrac{1}{2}V_{ac}^2\cos(2\omega t)\Big]\frac{\partial C}{\partial\zeta}\Big|_{y=y'}$$

(4.16)

and again

$$\lambda=\tfrac{1}{2}\Big[\left(V_{dc}^2+\tfrac{1}{2}V_{ac}^2\right)+2V_{dc}V_{ac}\cos(\omega t)+V_{ac}^2\cos(2\omega t)\Big]$$

which is now absorbed into κ' to show that the dc voltage can affect $\omega_0/2$ through nonlinearities. Comparing Figs. 4.13 and 4.14, the linear spring constant κ is affected by a shift in the resonance for ω_0 and maybe only for the quadratic term for $\omega_0/2$ since we know that the cubic term is known not to shift the resonance [41]. In other words, we
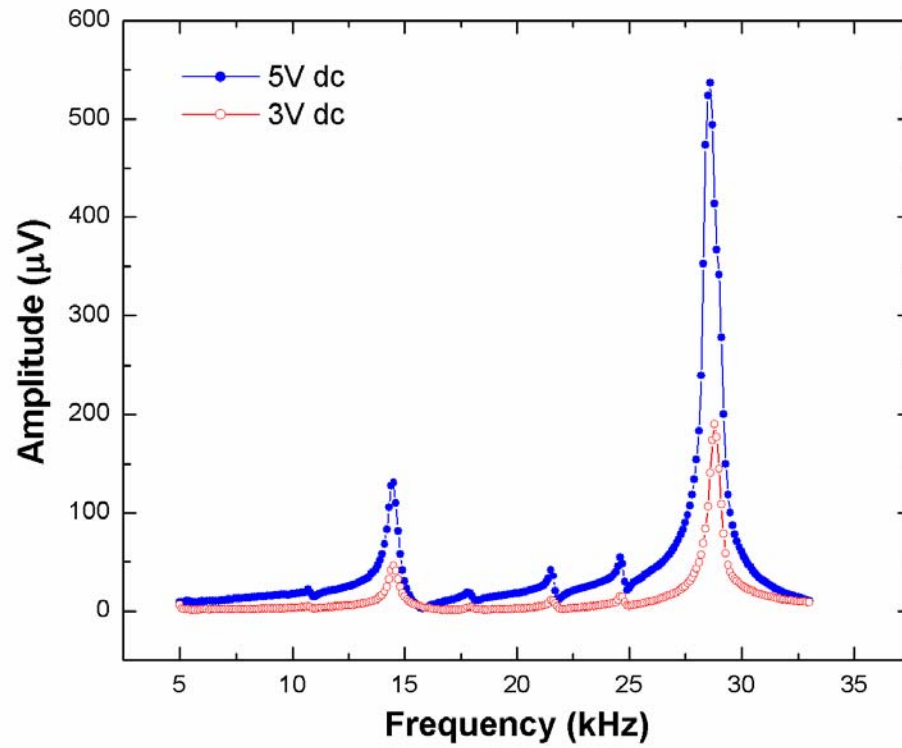
Figure 4.12: Frequency-amplitude spectrum for a tipless silicon cantilever (300 µm long, 35 µm wide, and 2 µm thick).
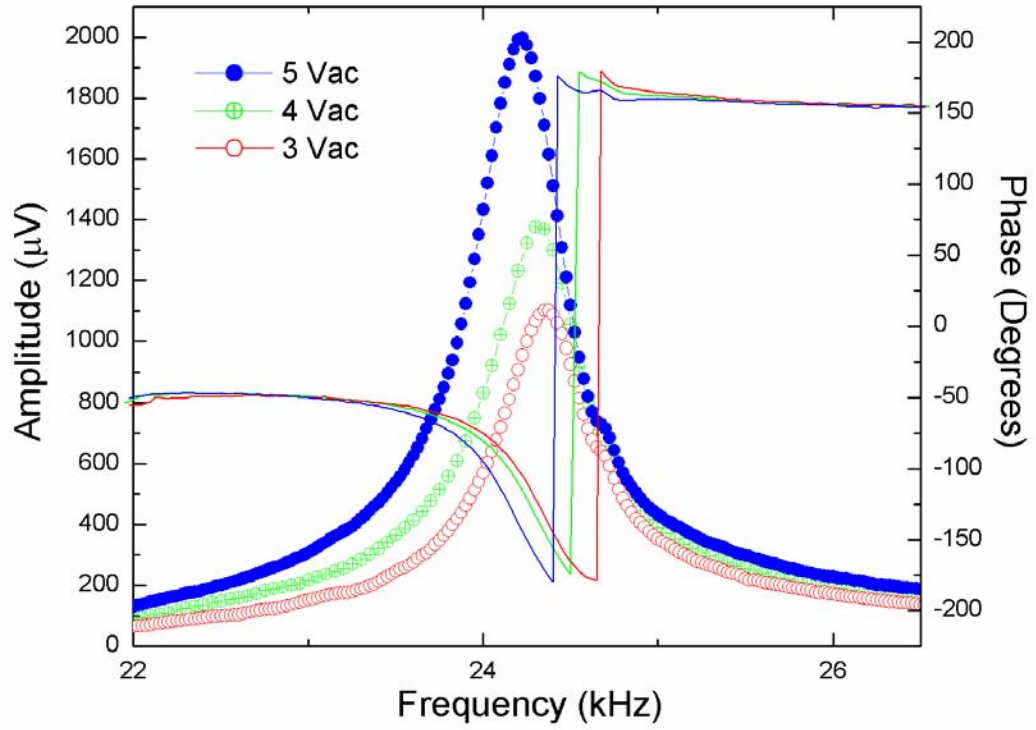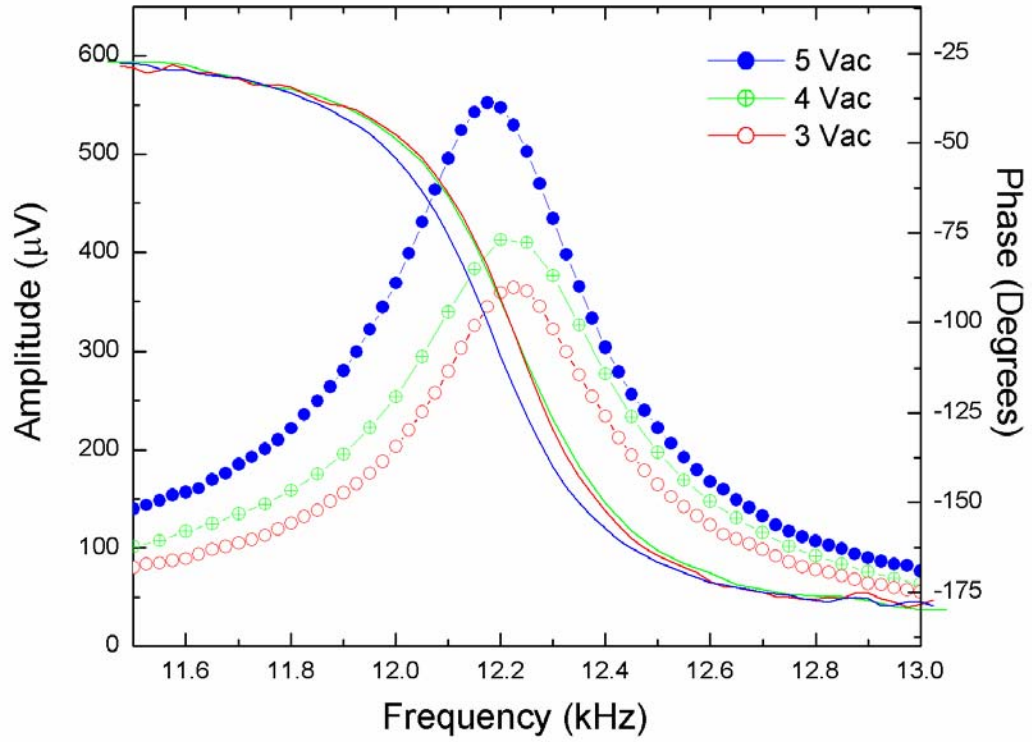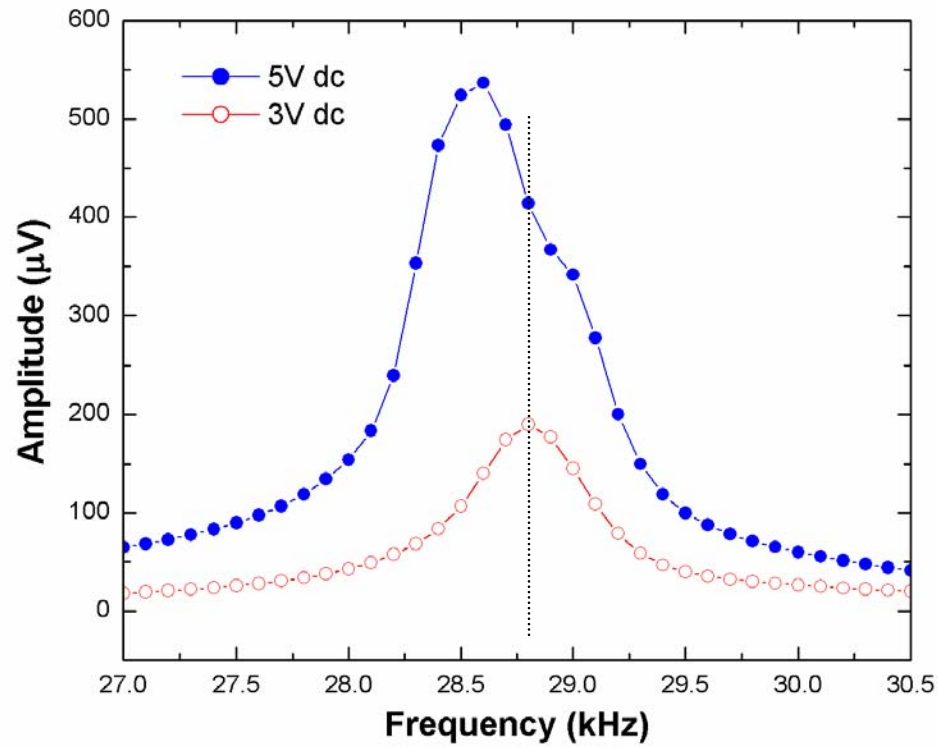
Figure 4.13: Dc voltage change from 3 to 5 V_{ac} at ω_0. The resonant peak is at 28.8 kHz for 3 V_{ac}. This peak at ω_0 shows a considerable downshift in the frequency as the V_{dc} is increased.
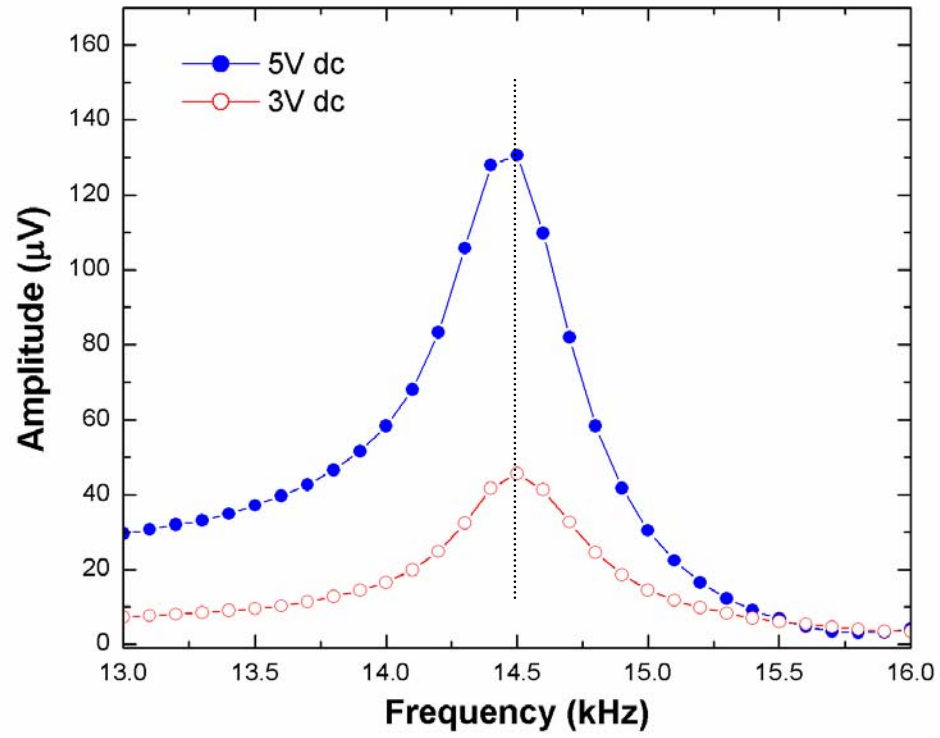
Figure 4.14: dc voltage change from 3 to 5 V_{ac} at $\omega_0/2$. The resonant peak is at 14.5 kHz for 3 V_{ac}. This peak at $\omega_0/2$ shows considerably smaller downshift in the frequency as compared to the downshift at ω_0.

notice that the shift in frequency at $\omega_0/2$ is small and is due to nonlinearities in the spring constant and not due to the Duffing effect. Throughout the experiments it has been observed, qualitatively speaking, that the value chosen for the ac voltage can range from 2-10 ac volts and not affect the experiment significantly, but anything below 3 V_{dc} and preferably below 8 V_{dc} is affect it substantial. Understanding these voltage dependences are important because they give insight into what to expect as we go into the future with HDR-cantilever applications that require knowledge of the parameters needed to understand the experiment.

4.4.6   HDR under vacuum

A small vacuum cell was built to measure the response of the cantilever at low pressures (see Appendix A). The most common method used to actuate cantilevers in the past has been the piezoelectric method. As mentioned in section 4.4.4 and shown in Fig. 4.4, the quality factor Q measured in the second harmonic using HDR in air is significantly better than when exciting the cantilever piezoelectrically. Mertens et al. presented the quality factor of a cantilever which resonates at ~ 25 kHz via piezoelectric actuation [42]. For this cantilever, they showed that the Q-factor changed from ~ 30 in air to ~ 800 at 3×10^{-3} torr. Figure 4.15 details data with resonance at $\omega_0 \cong 22.3$ kHz which has a Q-factor of ~ 40 in air and a remarkable ~ 6,840 at 3.2×10^{-3} torr using HDR. This is almost an order of magnitude better by using our actuation and detection scheme.
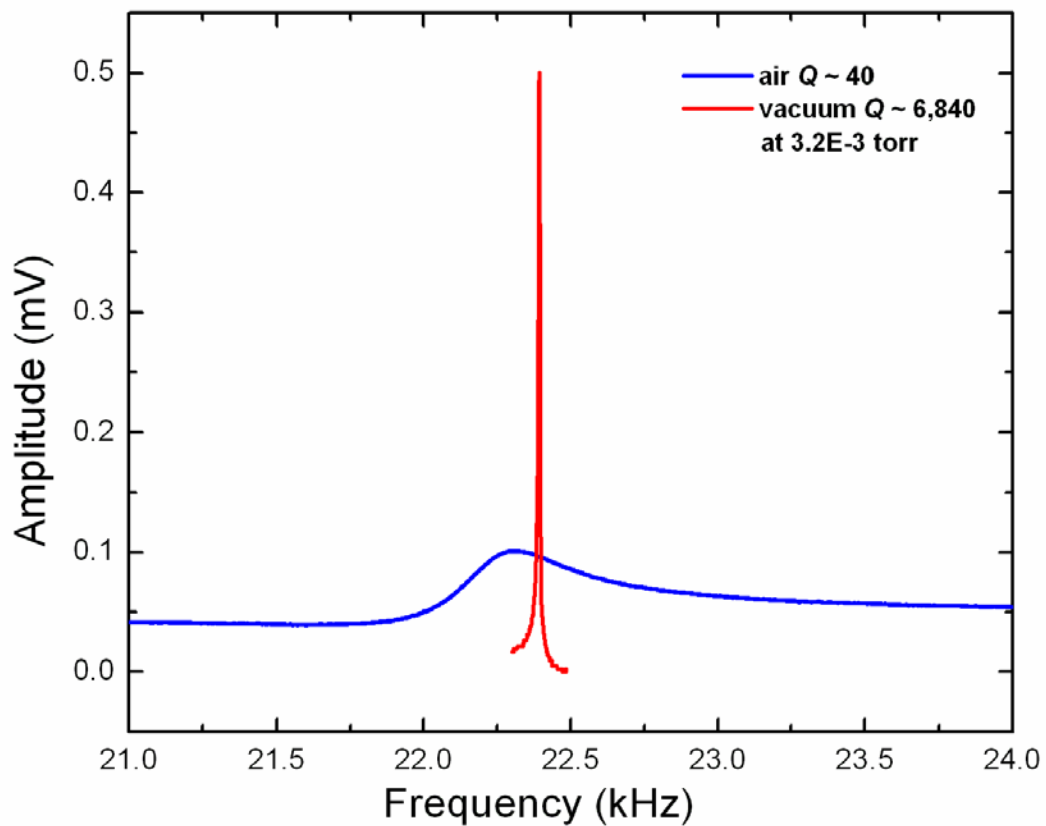
Figure 4.15: Vacuum measurement for a tipless silicon cantilever (350 µm long, 35 µm

wide, and 2 µm thick). The Q-factor changes from 40 to 6,840 with a change in pressure.

4.4.7   Gap dependence for cantilever and counter electrode

To gain further insight into the behavior of electrostatic actuation, measurements were taken for different gap distances between the cantilever and counter electrode. Since the value of the gap distances are not known, the conclusions here are just qualitative. To change the gap, the cantilever was mounted on a piezotube (see Appendix B). The piezotube has five quadrants to give $\pm$ x, $\pm$ y, and + z positional capabilities. For these experiments, the $\pm$ x and $\pm$ y quadrants were grounded while the z quadrant, which is a complete tube coaxially inside the outer four quadrants, is given a plus or minus voltage. The gap distance is then parallel to the z direction. A positive voltage is set to decrease the gap distance, and a negative voltage is set to increase the distance. The results are shown in Figs. 4.16 and 4.17. Smaller increments were used for the positive voltage as an extra precaution to prevent a collapse of the cantilever into the counter electrode.

As seen in Figs. 4.16 and 4.17, adjusting the gap distance changes the amplitude, phase, and the frequency. It is an easy assumption that a decrease in the gap distance will increase the signal. We know that the signal measured at the lock-in is dependent on the amount of charge modulated on the cantilever. Since the capacitance increases with a decrease in gap distance, we know that the signal should increase from the linear relationship between the capacitance and charge. On the contrary, the increase is mostly due to the increase in deflection in the cantilever's motion. This is because we are measuring at the 2nd harmonic and thus the parasitic signals coming from the static capacitance are small. Some small signal does come from the static capacitance at the 2nd harmonic, but almost completely disappears at the third as can be seen by evaluating the
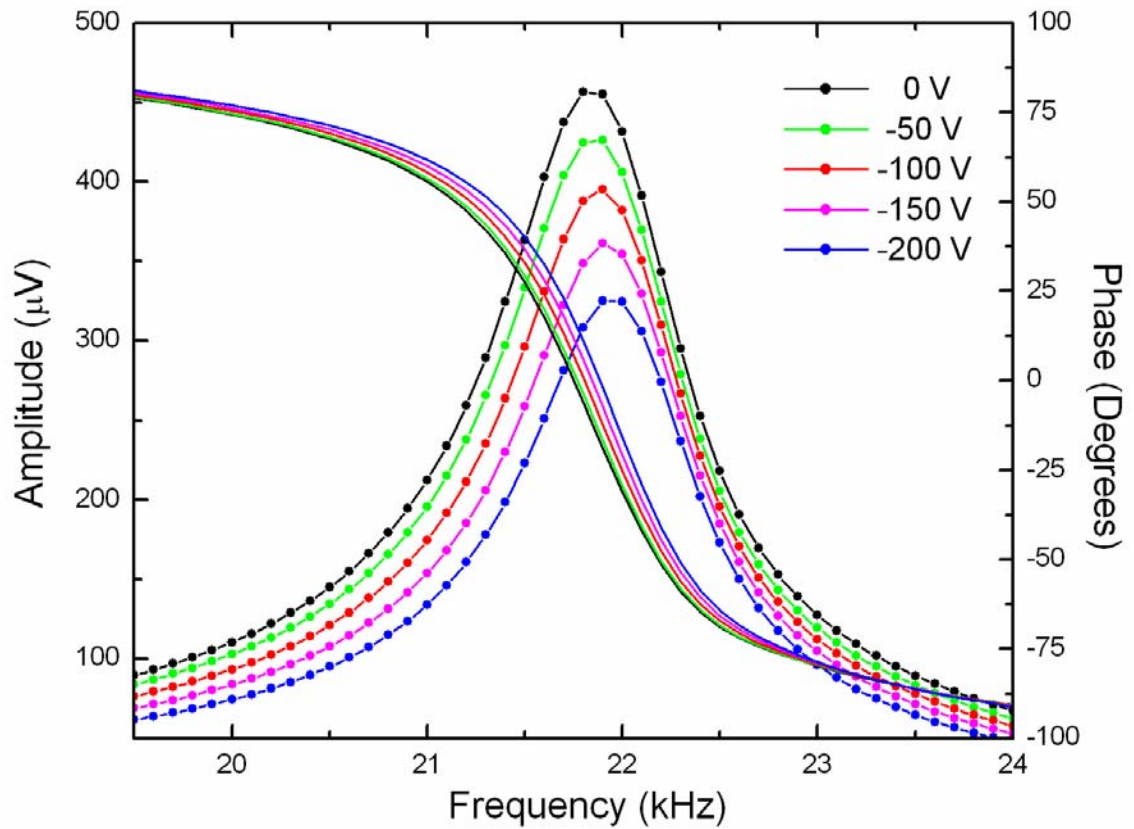
Figure 4.16: Gap dependence measurements for a tipless silicon cantilever (350 µm long, 35 µm wide, and 2 µm thick). The gap between the cantilever and counter electrode is increased by applying increments of - 50 volts to the piezotube in which the cantilever is mounted.
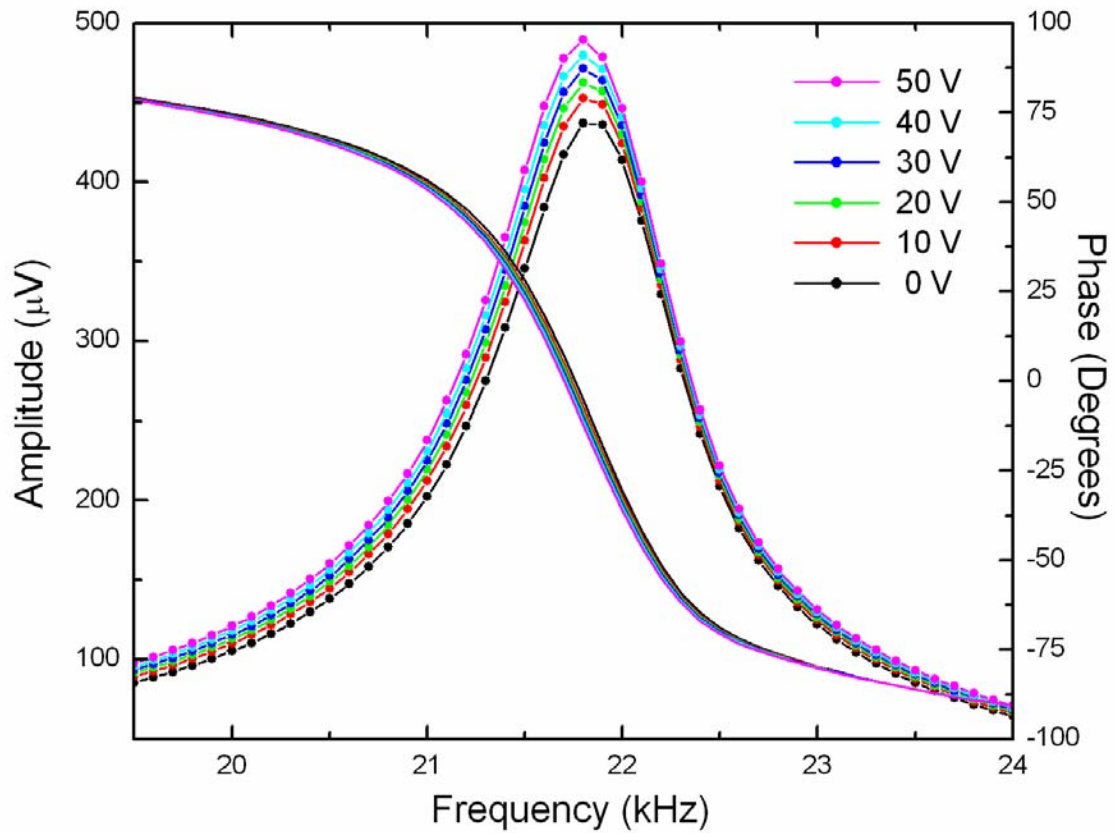
Figure 4.17: Gap dependence measurements for a tipless silicon cantilever (350 μm long, 35 μm wide, and 2 μm thick). The gap between the cantilever and counter electrode is decreased by applying increments of 10 volts to the piezotube in which the cantilever is mounted.

baselines in Fig. 4.2a From the images there also is also an obvious downshift in frequency with a decrease in gap distance. This is simply due to spring softening from the increase in deflection.

4.4.8   Measuring a nanocantilever (MWNT) using HDR

To demonstrate measurements at the nanoscale and test the limits of sensitivity offered by our HDR technique, we measured the resonant frequency and phase for cantilevered MWNTs. This was done by mounting a MWNT on a sharpened gold-coated tungsten probe and manipulating it ~1 µm away from and parallel to a gold-coated tungsten counter electrode with a tip radius of ~ 50nm. The MWNTs used in this study were grown by a chemical vapor deposition method reported previously with an average diameter of ~ 50 nm [35]. Figure 4.18 displays typical resonance and phase spectra. The amplitude of the vibration of the nanotube was barely discernable in the dark field microscope, implying that it was less than 200 nm. For comparison, the signal in Fig. 4.18 was also collected in the absence of the MWNT for the same tungsten probe geometry. Similar to the Si micro-cantilever, we observe an accompanying change in phase of 50^0. It is reasonable that in the presence of noise, a phase change of less than 180^0 will be observed, as discussed below. For the MWNT in Fig. 4.18, we calculated Q_{eff} as 30 and an SBR of ~ 0.5. The ac voltage was changed to show a shift in the resonant frequency (Fig. 4.19).
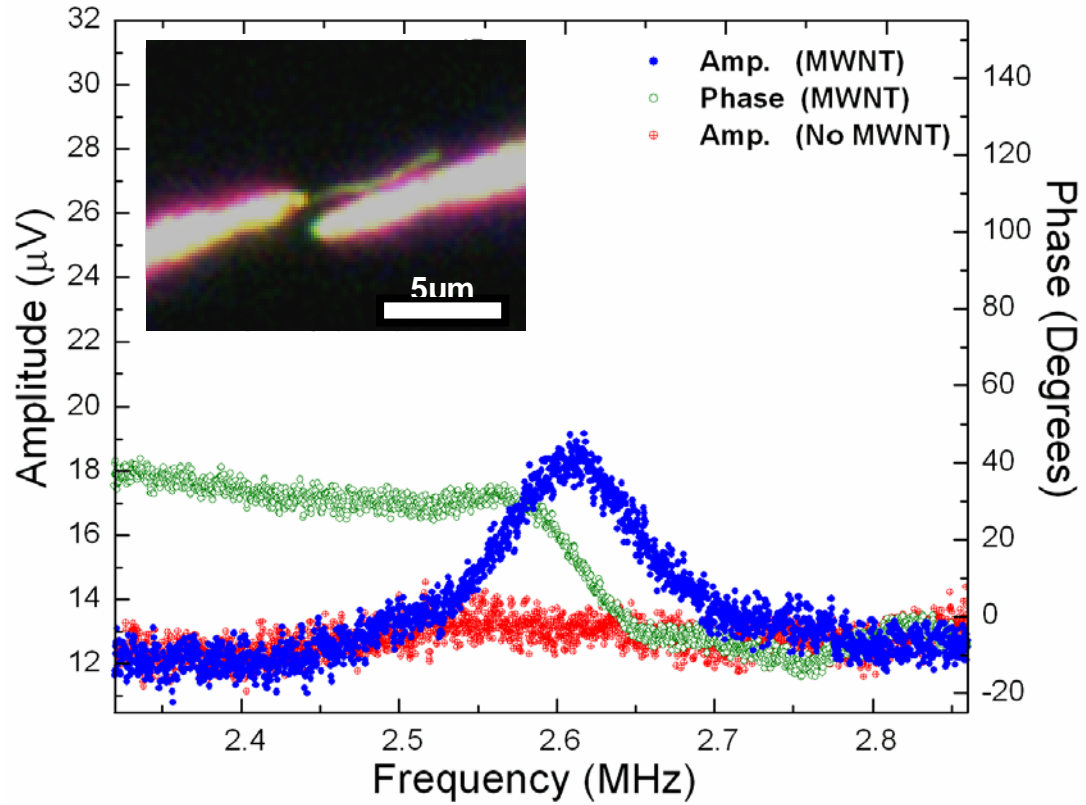
4.18: Electrical data for the amplitude (solid circles) and phase (open circles) of a MWNT (7 μm long and 50 nm in diameter) near resonance measured under ambient conditions. Even for such a small cantilever vibrating in air, the resonance spectrum is well resolved with a $Q_{eff} \sim 30$. The inset shows an optical darkfield image of the MWNT placed parallel to the counter electrode.
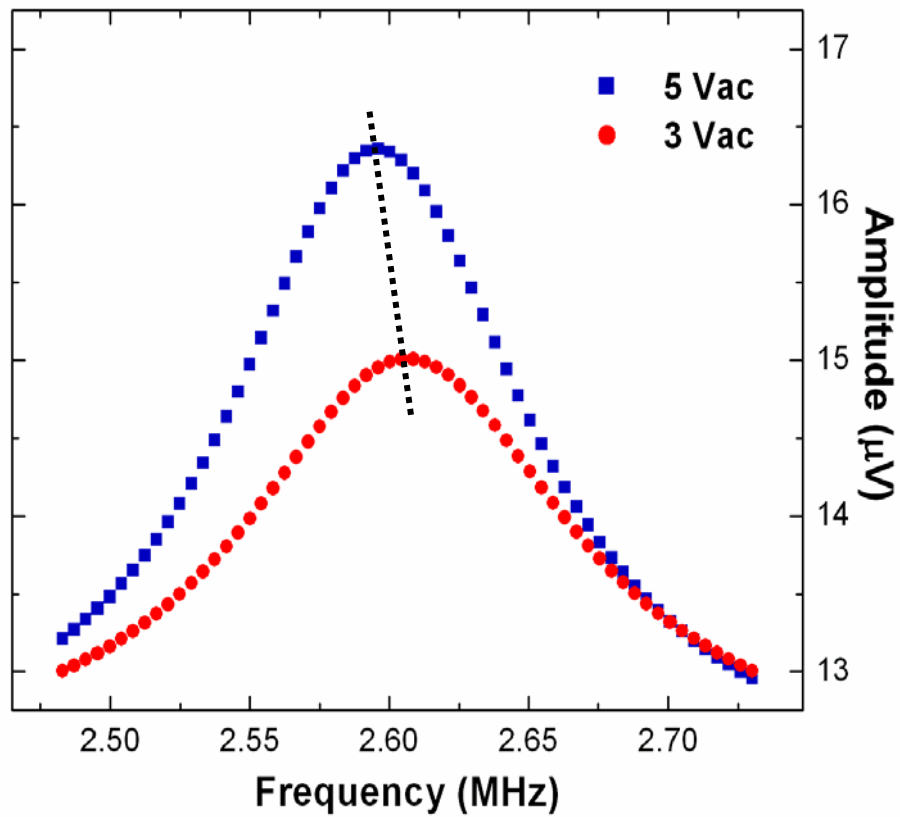
Figure 4.19: Lorenzian fit to an ac dependence of the MWNT at resonance. The resonance frequency downshifts as the applied ac voltage is increased from 3 to 5 volts, insuring that we are observing a resonance peak of the MWNT. The black dashed line serves as the guide to the eye.

In Fig. 4.20 we show a polar plot with the amplitude as r and the phase as θ, with the frequency as a parameter. If there were no background, the plot would be a clockwise circle with the start and finish close to the origin. This fact is exemplified by the data obtained for a micro-cantilever as discussed in Fig. 4.20. The presence of the background signal for the nano-cantilever data of Fig. 4.18 shifts the start of the polar plot in Fig. 4.20, but it is obvious that the resonance draws a near circle on the polar plot, so that the true phase change due to the transition in the absence of background signals would be $\sim 180^0$.

4.5 Conclusions

We assert that our HDR method works well for resonance studies of micro- and nano- sized cantilevers, and can be readily integrated into devices using standard silicon based fabrication techniques. The HDR technique can be used to detect higher harmonics of the oscillations with sufficient increase in the signal to noise ratio at high repeatability, and facilitates measurements of oscillations in nano-cantilevers as a function of external parameters such as pressure or temperature in real time. Finally, we note that (i) in vacuum, the Q_{eff} of these micro- and nano-systems can be expected to be significantly higher than that presented in this manuscript, and (ii) the high resonance frequencies may permit devices to operate in the radio frequency range. These attributes of our HDR method helps us move a step closer to realizing nano-cantilever based devices for diverse applications.
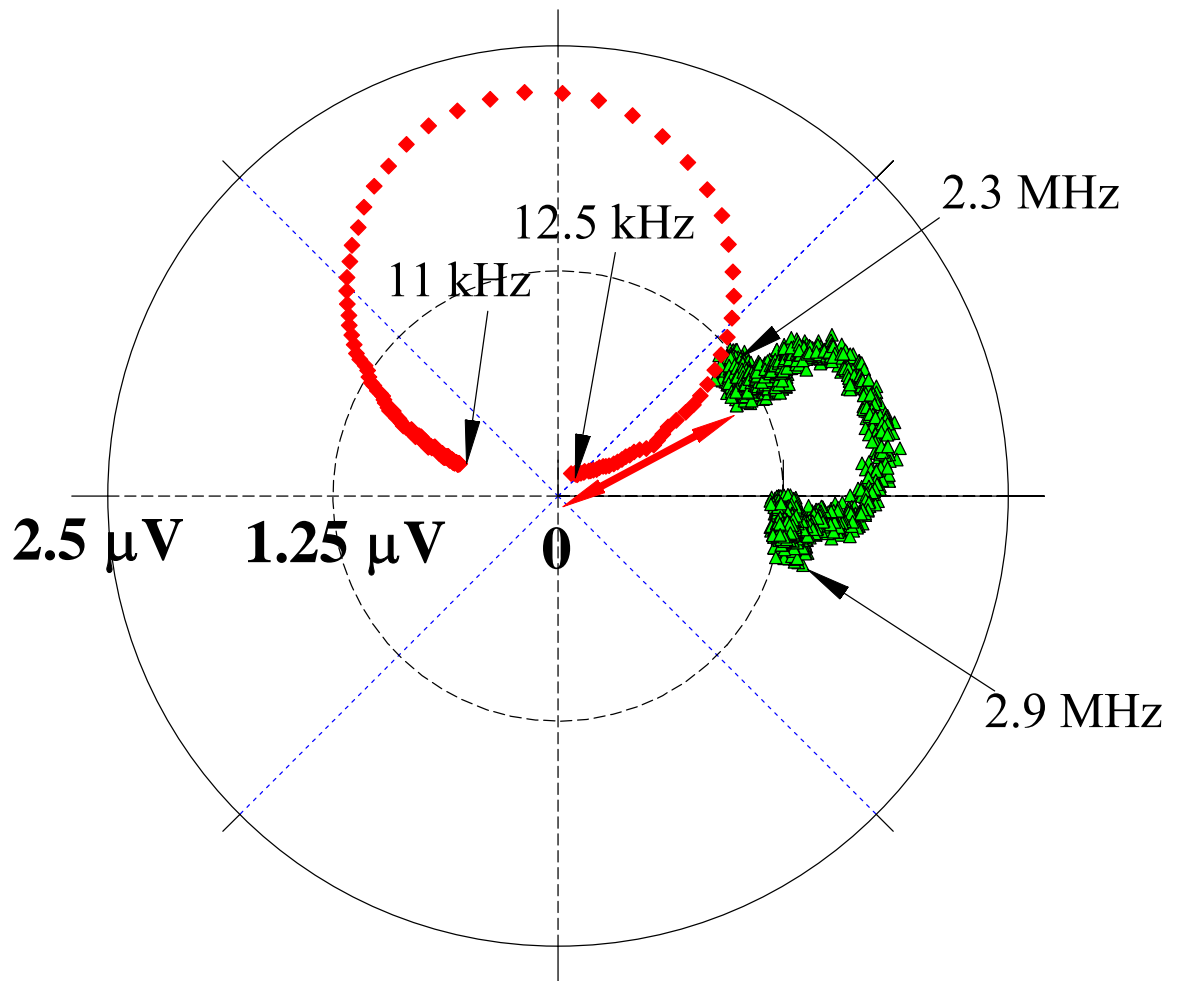
Figure 4.20: A polar plot using the amplitude of the vibration of each of two cantilevers as r and the phase of their vibrations as θ. The frequency is a parameter, with the beginning and ending frequencies indicated. For the silicon cantilever with dimensions of 300 x 35 x 2 µm (diamonds), the frequency steps are 100 Hz, and for the MWNT of Fig. 5 (triangles) the steps are 250 Hz. The plot for the silicon micro-cantilever, for which the amplitude is 20 times the indicated scale, illustrates the circle that a resonance shows on a polar plot. The much smaller signal from the MWNT shows the effect of a background signal of the same order of magnitude as the resonant signal. The double-headed arrow indicates the background signal amplitude and phase. One can see that although the nanotube resonance shows a nearly complete circle on the polar plot, the offset provided by the background signal leads to an apparent phase change ($\Delta\theta$ from the start to the finish of the resonance) of only ~30^0.

CHAPTER 5

DETERMINATION OF THE BENDING MODULUS OF AN INDIVIDUAL MULTI-

WALLED CARBON NANOTUBE USING HDR

5.1 Introduction

In the following chapter, the bending modulus of an individual MWNT is determined using HDR [43, 44], with the driving force possibly parametric As shown previously, we excite the oscillations electrostatically, and demonstrate that we can detect the amplitude and phase of the resulting oscillation electrically. The MWNT and counter electrode are placed in a tip-to-tip configuration for these experiments. Measurements are presented for the fundamental and first two overtones of the diving board resonance of a MWNT at 0.339, 2.42, and 5.31 MHz in ambient conditions. Corresponding quality factors are 67, 36 and 25, respectively.

There is extensive experimental and theoretical interest in the mechanical properties of carbon nanotubes. This is due, in part, to the presence of strong covalent bonds in these nearly 1D structures. The first experimental determination of the bending modulus (E_b) for an individual MWNT used the intrinsic thermal vibrations analyzed under a transmission electron microscope (TEM) [45]. Wong et al. [27] measured the lateral force needed to bend a MWNT clamped at one end, while Yu et al.[46] measured the stress-strain curves for individual MWNTs clamped between two atomic force microscope (AFM) cantilevers inside a scanning electron microscope (SEM). Cooling-

induced compressive deformation of MWNTs embedded in an epoxy matrix was monitored in a temperature-dependent micro-Raman study [47]. Finally, E_b has also been determined from electric field induced mechanical oscillations in cantilevered MWNTs from the amplitude-frequency response: (i) recorded using a TEM [17], (ii) SEM [48], (iii) field emission microscopy [49], and (iv) an optical microscope [50, 51].

5.2 Experiment

A MWNT is first placed on a sharpened gold-coated tungsten probe tip by applying a dc voltage between the coated tungsten probe and a mat of MWNTs attached to SEM tape [51]. Another gold-coated tungsten probe tip serves as the counter electrode, and is brought in close proximity to and aligned with the MWNT (Fig. 5.1a). The alignment of the MWNT with the counter electrode was carefully monitored using a dark field optical microscope (Nikon Epiphot 200) equipped with a digital camera (MOTICAM 1000). An ac voltage, V_{ac}, as well as a dc voltage, V_{dc}, induces charges on the MWNT [17]. The electrostatic force, F_e, between the charges residing on the MWNT and the counter electrode causes the MWNT to oscillate (Fig. 5.1b). When $V_{ac} = 0$, the total potential difference between the MWNT and the counter electrode is $\dfrac{W_{Au} - W_{MWNT}}{e} + V_{dc}$, where W_{Au} and W_{MWNT} are the work functions for the counter electrode and the MWNT. The modulated charge on the MWNT is detected using the HDR method. The output signal of the A250 is coherently detected using a lock-in amplifier set for 2nd harmonic detection. Again, we find a higher signal to noise ratio using detection at the 2nd harmonic rather than detection at the same frequency as the oscillator. As mentioned previously, we attribute this to avoiding the much larger interfering signal at the driving

frequency. All measurements reported here were performed in air under ambient conditions. A computerized data acquisition system collected the excitation frequency (f_E) provided by the signal generator, and the amplitude and phase of the A250 output signal as measured by the lock-in amplifier.

5.3 Theory for a tip-to-tip geometry

The charges accumulated at the tip of the MWNT and on the counter electrode can be assumed to be quasi point charges, Q, which can be expressed as [52]:

$$Q = \alpha\left[(W_{Au} - W_{MWNT}) + e(V_{dc} + V_{ac}\cos 2\pi f_E t)\right] \tag{5.1}$$

where α is a geometrical factor related to the counter electrode geometry and the charges are separated by a distance R (Fig. 5.1b). The Coulomb force, F_e, between the charges on the counter-electrode tip and MWNT is given by:

$$F_e = \frac{1}{4\pi\varepsilon_o\varepsilon_r R^2}Q^2 = \frac{\alpha^2}{4\pi\varepsilon_o\varepsilon_r R^2}\left[A_{DC} + A_{f_E}\cos 2\pi f_E t + A_{2f_E}\cos 4\pi f_E t\right] \tag{5.2}$$

where $A_{DC} = \left[(W_{Au} - W_{MWNT}) + eV_{dc}\right]^2 + e^2\dfrac{V_{ac}^2}{2}$; $A_{f_E} = 2eV_{ac}\left[(W_{Au} - W_{MWNT}) + eV_{dc}\right]$ and

$A_{2f_E} = e^2\dfrac{V_{ac}^2}{2}$. Typical experimental parameters V_{dc}, V_{ac} and R were 9 V, 5 V (peak to peak) and 200 nm which resulted in small oscillations of the MWNT, not observable in the optical microscope, presumably along the y direction. For small oscillations, the excitation y of each normal mode can be expressed [53] as a forced oscillator with damping $b\dfrac{\partial y}{\partial t}$

$$m_e\frac{\partial^2 y}{\partial t^2} + b\frac{\partial y}{\partial t} + k_e y = F_e, \tag{5.3}$$

81
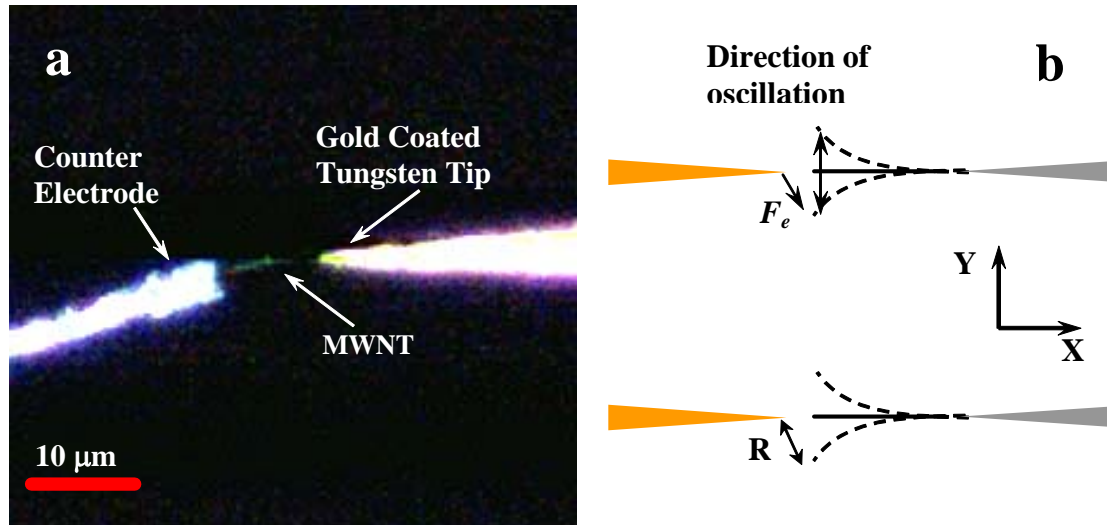
Figure 5.1 (a) Dark field microscope image of the geometrical setup for the MWNT and the counter electrode assembly. The MWNT is in very close proximity of the counter electrode (see text). (b) A schematic of mechanical oscillations induced in a MWNT by the electric force F_e when the MWNT and the counter electrode are separated by a distance R.

where the m_e, k_e and F_e are the mass, elastic constant and force for an equivalent oscillator driven at frequency f_E. When the resonance frequency f_i of a mode is near f_E, the steady state solution for equation 3 can be written as:

$$y = \frac{\alpha^2}{4\pi\varepsilon_o\varepsilon_r R^2} \frac{A_{f_E}}{2\pi\sqrt{m_e^2\left(f_E^2 - f_i^2\right)^2 + b^2 f_E^2}} \sin\left(2\pi f_E t - \delta\right),$$ (5.4)

where the phase shift δ for the mode with frequency f_i is given by :

$$\delta = \cos^{-1}\left(\frac{b f_E}{\sqrt{m_e^2\left(f_E^2 - f_i^2\right)^2 + b^2 f_E^2}}\right)$$ (5.5)

The resonance frequencies of the cantilevered MWNT are obtained by finding the excitation frequencies that match natural mode frequencies. Note that similar expressions can be obtained for a steady state solution when f_E is near $\frac{1}{2} f_i$.

5.4 Results and discussion

Figure 5.2a shows typical resonance spectra for a CVD grown MWNT with $L = 10\ \mu m$, $D_i = 17$ nm, and $D_o = 57$ nm [21]. The initial gap distance R_i (i.e., $V_{ac} = V_{dc} = 0$) is estimated to be ~ 200 nm, which is the resolution limit of our optical system. In accord with equations 4 and 5, f_i for the MWNT is identified with the frequency for which the amplitude reaches its local maximum (Fig. 5.2a, light circle trace). The light triangle trace in Fig. 5.2a shows the associated 160^0 change in δ. Amplitude (dark circles) and phase (dark triangles) signals obtained for the same geometry of the electrodes in the absence of the MWNT are also plotted in Fig. 5.2a. The maximum amplitude and phase change occur when the excitation frequency reaches 2.420 MHz. No noticeable changes
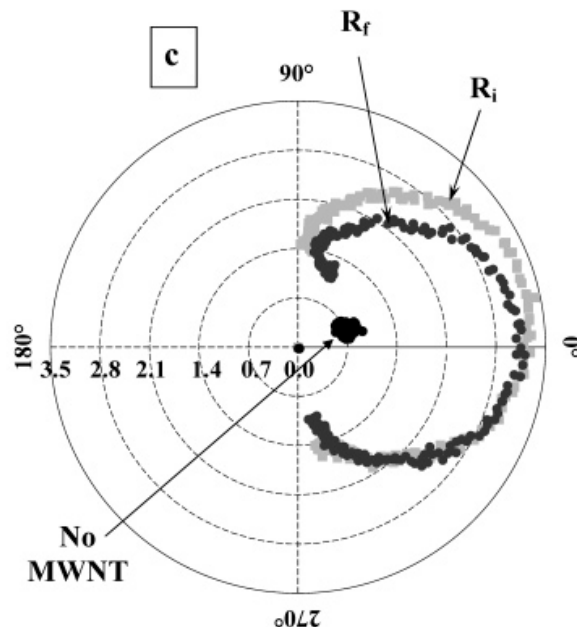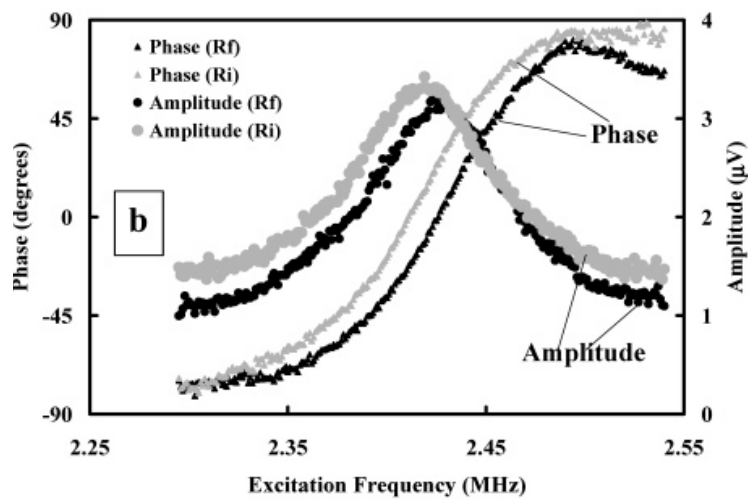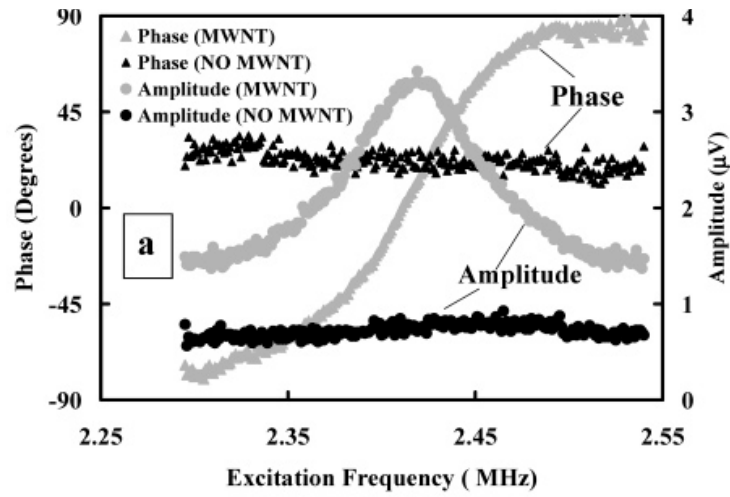
Figure 5.2 (a) Frequency dependence for the amplitude (circles) and phase (triangles) signals obtained from the output of the lock-in amplifier in the presence (light) and absence (dark) of a MWNT. (b) The amplitude (circles) and phase (triangles) signals plotted as a function of frequency for two different distances of the MWNT from the counter electrode: R_i (light), R_f (dark) where $R_f > R_i$. (c) A polar plot (where the radius is the amplitude and the angle is the phase) of the data presented for the two resonances shown in Fig. 5.2b. As expected from theory, the plot is a circle displaced from the origin by the background signal. The resonance frequency is determined to be at the place on the circle where the distance between data points on the circle is a maximum.

in the traces for the amplitude and phase can be discerned in the frequency range between 2.250 to 2.550 MHz when the MWNT is absent.

As a further verification that the local maximum observed using electrical detection of resonance in the cantilevered MWNT corresponds to a resonance frequency of the MWNT, we re-measured f_i and δ after moving the manual micromanipulator to increase R. The motion was less than the resolution of the optical system, so we estimate the difference between R_i and R_f to be less than 200 nm. It is not essential for our method to know the exact change in order to show qualitatively that increasing R increases f_i. Figure 5.2b depicts the results for two gap distances: R_i and $R_f > R_i$. The frequency shifts from 2.420 MHz to 2.425 MHz in the amplitude traces (Fig. 5.2b) but the polar plot (Fig. 5.2c), which involves both the amplitude and phase, shows that the actual shift is from 2.420 MHz to 2.436 MHz. The slight increase of f_i when R is increased (i) confirms that the resonance data shown in Fig. 5.2 corresponds to a mechanical resonance of the cantilevered MWNT, and (ii) provides evidence for parametric and/or nonlinear effects [17, 25, 48]. Furthermore, the phase change remains constant (around 160º) when the distance R is varied, also consistent with equation 5.5. Finally, it should be mentioned that the quality factor, which is a measure of how mechanical energy is transferred into electric energy, decreases from 37 to 31 when R increases (see Fig. 5.2b).

For a MWNT clamped at one end, the frequency of the ith mode of vibration is given by [17, 44, 45]:

$$f_i = \frac{\beta_i^2}{8\pi} \frac{1}{L^2} \sqrt{\frac{\left(D_o^2 + D_i^2\right)E}{\rho}} \ .$$

(5.6)

We measured the density of MWNT to be 2100 kg/m³ [56]. Note that we measure the bending modulus of the nanotube. As long as the nanotube does not change its geometry by buckling [17] or any other such deformation, the bending modulus is equal to Young's modulus [55]. The length and outside diameter for the MWNT whose resonance spectra are discussed in Fig. 5.2 were determined from scanning electron microscope images to be: L =10 μm, D_o = 57 nm, the inner diameter was determined numerically using the algorithm described below. The resonance spectra two other MWNTs were measured electrically and its L, D_o and D_i determined using transmission electron microscopy. Table 5.1 summarizes the measurements performed on these two MWNTs.

The experimentally determined resonances for the MWNT discussed in Fig. 5.2 were found at f_{1e}= 0.339 MHz, f_{2e}= 2.42 MHz and f_{3e}= 5.31 MHz (Figs. 5.3a and 5.3b). The bending modulus, E, was computed using a multi-step procedure. At each step, the f_i's were computed using equation 5.6 starting with the measured values for D_o, D_i and L and a range of values for E. Then the mean squared error (*MSE*) for a particular E was computed as:

$$MSE = \frac{1}{3}\sum_{i=1}^{3}(f_i - f_{ie})^2 \qquad (5.7)$$

Table 5.1: The geometric parameters of the MWNTs investigated in this study. L, D_o, D_i, and f_{1e} correspond respectively to the length, outer and inner tube diameters, and the fundamental resonant frequency.

Sample	L (μm)	D_o (nm)	D_i (nm)	f_{1e} (MHz)
1	10	57	17	0.34
2	8.9	86.6	11.4	0.45
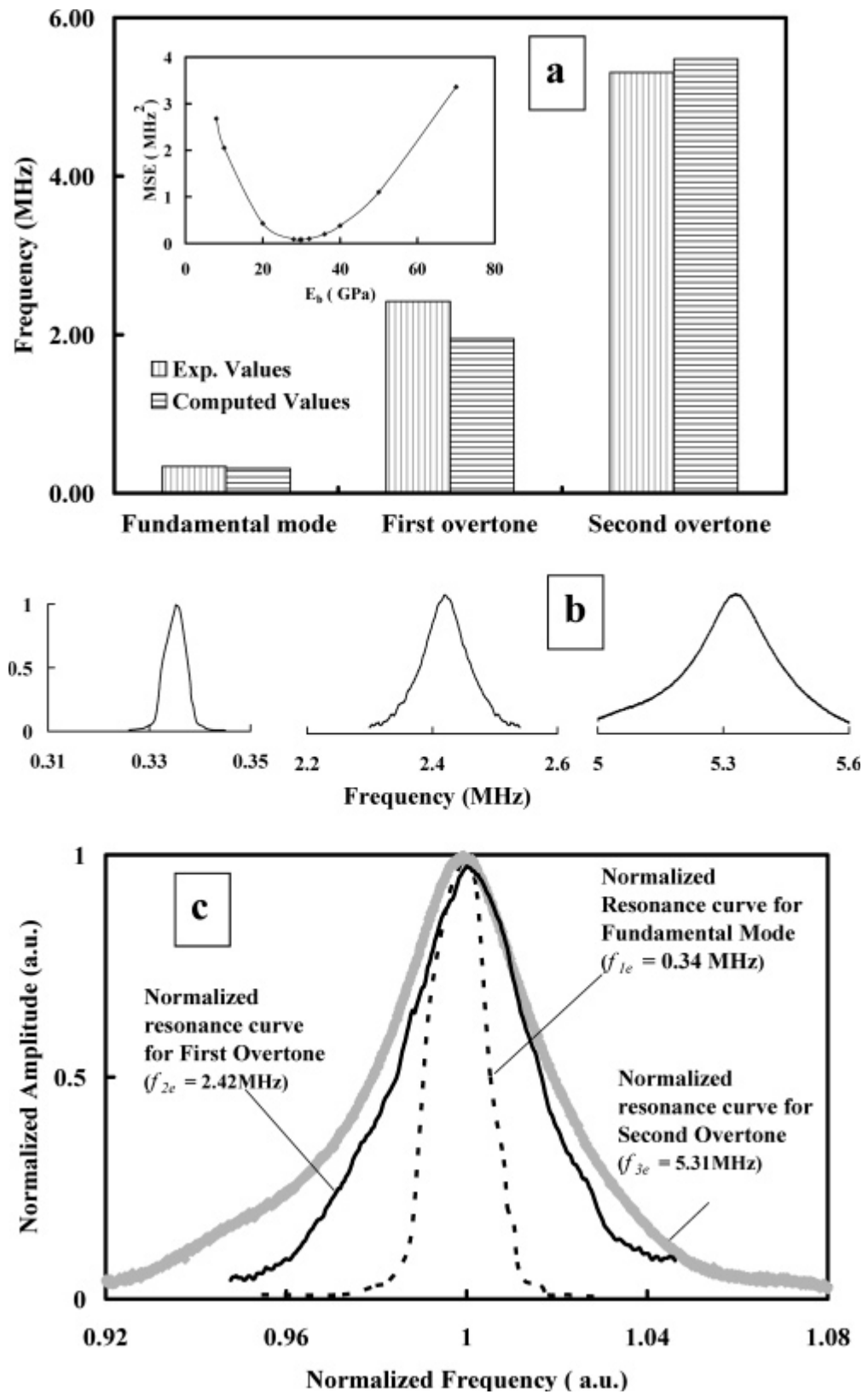
Figure 5.3 (a) Experimental (vertical stripes) and computed (horizontal stripes) frequencies for the fundamental, first and second overtones in a MWNT. The inset is a plot of the mean squared error between the experimental and computed values for bending modulus (see text). (b) The measured amplitude for the fundamental, first and second overtones in a MWNT. For clarity, these amplitudes are plotted on a normalized ordinate. (c) Same as (b), but plotted on a normalized frequency scale.

As the inset in Fig. 5.3a shows we find a minimum in *MSE* for *E* = 29.6 GPa.
Then the values of *L* and D_o were perturbed by about ±10% and the minima in *MSE*
recomputed to assure ourselves that the minimum was global rather than local. A
comparison between experimentally determined frequencies (vertical stripes) and
computed values (horizontal stripes) for *E* = 29.6 GPa is also shown in Fig. 5.3a. The
average error in frequency estimation is about ~10% (ranging from 18% for the first
overtone to 3% for the second overtone). Our value for the bending modulus *E* = 29.6 ±
2.9 GPa is in excellent agreement with those reported in the literature for MWNTs with
comparable dimensions [17]. The quality factor for each of the three resonances is 67, 36
and 25 for the fundamental and first two overtones respectively (see Fig. 3c). Recently, a
doubly clamped single walled carbon nanotube was electrically actuated and its resonant
frequency was detected using a mixer technique by McEuen and coworkers [57].
Although their technique is valuable for a beam in a guitar-like configuration, it cannot
be applied to a cantilevered nanostructure. Our values for the quality factor compare well
with the quality factors ~10-40 reported in the doubly clamped geometry at room
temperature and low pressure (less than 10 torr).

5.5 Conclusions

In conclusion, we describe a method for exciting and measuring the resonance
frequencies of an individual MWNT electrically. Our method detects the resonance
using higher harmonics of the exciting frequency and provides both the amplitude and
phase information. As a first application of our technique we obtain a bending modulus
of 29.6 GPa from the three experimentally observed resonances using an iterative

algorithm. This bending modulus is in excellent agreement with those reported in the literature from stress-strain measurements of MWNTs with comparable dimensions. This fully electrical approach for exciting and measuring the resonance frequencies is convenient and advantageous in devices that use MWNTs as the circuit elements or detectors.

CHAPTER 6

HARMONIC DETECTION OF SUPERHARMONICS OF ORDER ω_0/n IN

MICROCANTILEVERS VIA ELECTROSTATIC ACTUATION/ DETECTION

6.1 Introduction

In nonlinear dynamics, mechanical motion can be made up of a complicated

mixture of vibrations. Particularly, in resonating structures, nonlinearities are ubiquitous

and more often than not are undesirable [58]. Conversely, nonlinear dynamics and chaos

in electrostatic MEMS has been shown to be useful for various applications, including

secure communications, MEMS filters, and scanning force microscopy [59]. Exploiting

these dynamics opens the door for NEMS by providing signals with higher quality factors

(*Q*) and better signal-to-background ratios (*SBR*) [38,43]. In cantilever-based MEMS,

nonlinear dynamics usually involve harmonically forced [38,60] excitation in which *only*

the second superharmonic has been theorized[61,25] or detected[38,62]. Note that the

second superharmonic is the resonance measured at ω_0/2. Here we measure the

nonlinearly modulated charge on a silicon microcantilever up to the sixth superharmonic

of the fundamental resonant mode via electrostatic actuation/detection. In agreement with

experiment, simulated results reveal that the modulated charge with the cantilever's

motion carries a set of harmonics for each superharmonic of order ω_0/n. We propose that

using a system of superharmonics of the cantilever increases applications for cantilevered

and doubly-clamped microbeams, and that exploiting the nonlinearities in the modulated charge provides a valuable tool for the study of the dynamics in electrostatic transduction.

Theory predicts that the cantilever can be excited at the second superharmonic or subharmonic of the fundamental resonance. Second superharmonic and subharmonic resonance occurs at $\omega_0/2$ and $2\omega_0$ respectively. The harmonic excitations have been limited to their second term due to the two term excitation in the force equation. Parasitic crosstalk limits experimental study of these nonlinearities to measuring only the deflection of the cantilever beam by either external detection schemes or smart systems such as an integrated piezo resistor [62]. As far as known to the author superharmonics beyond $\omega_0/2$ have not been previously reported experimentally.

6.2 Superharmonic setup

The electrostatic device used in these studies is, as mentioned in previous chapters, a gold coated silicon micro-cantilever and a movable gold coated tungsten probe tip. We investigate the harmonics of the cantilever's motion and the modulated charge using the HDR method. The probe tip is placed parallel and center to the cantilever's surface where the gap distance can be adjusted using a micromanipulator. An adjustable gap distance provides additional insight into the nonlinearities of this system. In our experiments, a sinusoidal and static voltage is applied to the counter electrode in order to excite the harmonic motions. The charge is then measured by the lock-in at higher harmonics using the same capacitive transducer system. This provides additional harmonic information not measured by external or parasitically plagued detection

schemes; particularly, it reveals the harmonics stemming from nonlinearities and modulated charge at each superharmonic.

6.3 Superharmonics at ω_0/n

The microcantilever and counter-electrode constitute a dynamic capacitance (Fig. 6.1). The electrostatic force on the microcantilever is given by

$$F(t) = -\frac{dW}{dy} = -\frac{1}{2}\frac{dC}{dy}V(t)^2 \tag{6.1}$$

The capacitance is nonlinear in the deflection and thus we proceed by expanding the capacitance in a power series

$$C(y) \approx C_0 + C_1 y(t) + C_2 y(t)^2 + ... \tag{6.2}$$

Therefore

$$\frac{dC}{dy} \approx C_1 + C_2 y(t) + ... \tag{6.3}$$

Substituting this into the expression for the force yields

$$F(t) = \frac{1}{2}\left[C_1 + C_2 y(t) + ...\right]V(t)^2 \tag{6.4}$$

It is appropriate to assume that the response, y(t), can be expressed as a Fourier series with a fundamental natural frequency equal to the excitation frequency ω, which can be written as

$$y(t) \approx A_0 + \sum_{n=1}^{N} A_n \cos(n\omega t + \phi_n) \tag{6.5}$$
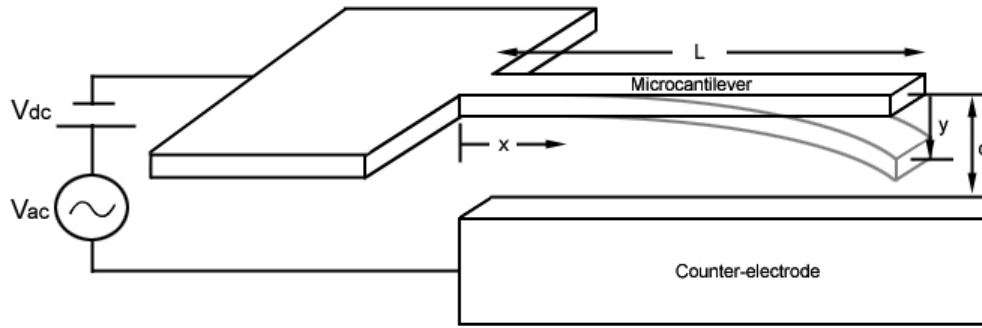
Figure 6.1: Schematic of microcantilever system.

The frequency component $n = 1$ is known as the fundamental harmonic. The components for $n > 1$ are known as the nth higher harmonics. This equation describes the motion of the cantilever at any point of resonance. Substituting this solution into equation (6.4) and simplifying using trigonometric identities we get

$$F(t) \approx F_0 + \sum_{n=1}^{N} F_n \cos(n\omega t + \phi_n)$$ (6.6)

From equation (6.6) it is obvious that at any excitation frequency $\omega = \omega_0/n$, where ω_0 is the natural resonant frequency of vibration of the microcantilever, there is a component of the force F_n that excites the microcantilever at the resonant frequency. Thus there are n super-harmonic resonant peaks in the frequency response of this system. Figure 6.2 shows a simulation using Matlab of the equations above.
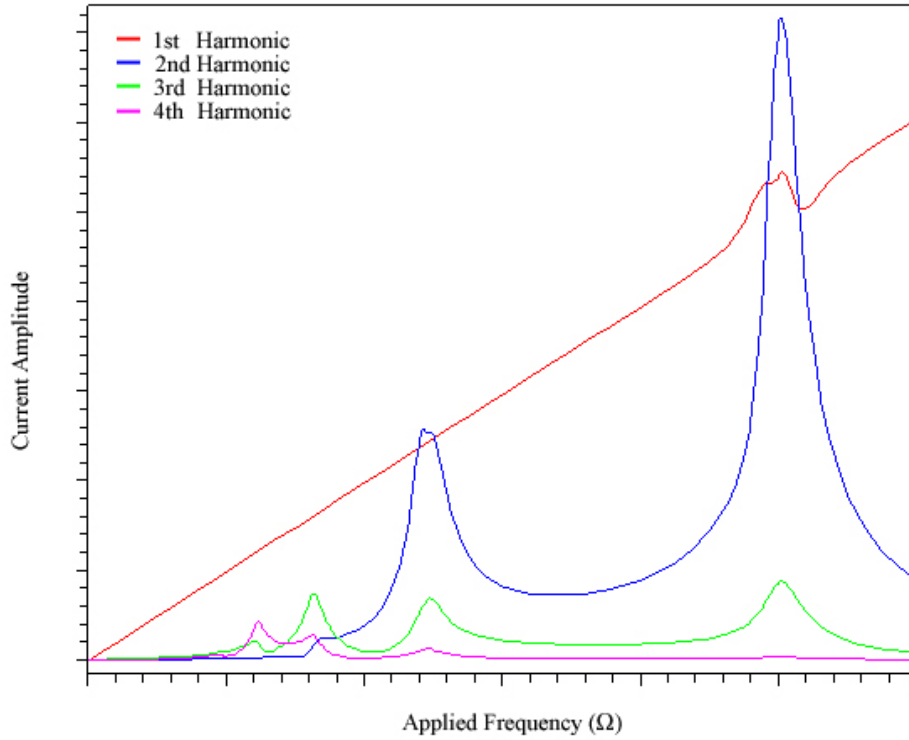
Figure 6.2: Simulation of equations (6.5) and (6.6). The parasitic signal present in the first harmonic has a linear relationship with the frequency. A general trend of $\omega_0/2$ peaks are present in the first four harmonics.

6.4 Results and discussion

Figure 6.3 shows the resonance spectrum for the first four harmonics. The dominate fundamental peak is at ~21.5 kHz. The cantilever measured in this experiment are of dimensions (350 μm long, 35 μm wide, and 2 μm thick). As expected the peaks decrease for each consecutive harmonic at every superharmonic. As can be seen in Fig. 6.3, we measure n resonant superharmonic peaks for the each nth harmonic. In a regime where the cantilever has a small deflection, peaks only appear at

$$\frac{n\omega_0}{m} \quad \text{where } n = 1, 2, 3, \dots \text{ and } m = 1, 2, 3, \dots, n \tag{6.7}$$

where n is the harmonic being *measured*. In other words, each harmonic will only carry the number of superharmonics for the value of the measured harmonic. Figure 6.4 further illustrates this concept. Notice that the 3$^{\text{rd}}$ harmonic has three peaks and the 4$^{\text{th}}$ harmonic has four peaks. No other peaks were detected for the scans shown in Fig. 6.4. In the darkfield microscope, only the resonance that occurs at ω_0 can be seen for the small deflections.

Now in the regime where the deflection is large, and thus the deflection can be seen at other superharmonics (Fig. 6.5), we can rewrite equation (6.7) as

$$\frac{n\omega_0}{m} \quad \text{where } n = 1, 2, 3, \dots \text{ and } m = 1, 2, 3, \dots \tag{6.8}$$

where the peaks are *measured*. We can now simplify this equation to where resonant peaks are being *driven* as

$$\frac{\omega_0}{n} \quad \text{where } n = 1, 2, 3, \dots \tag{6.9}$$

where ω_0/n occurs at the nth superharmonic of the fundamental resonance. The data which relates to equation (6.8) and Fig. 6.5 is shown in Fig. 6.6. To obtain these peaks,
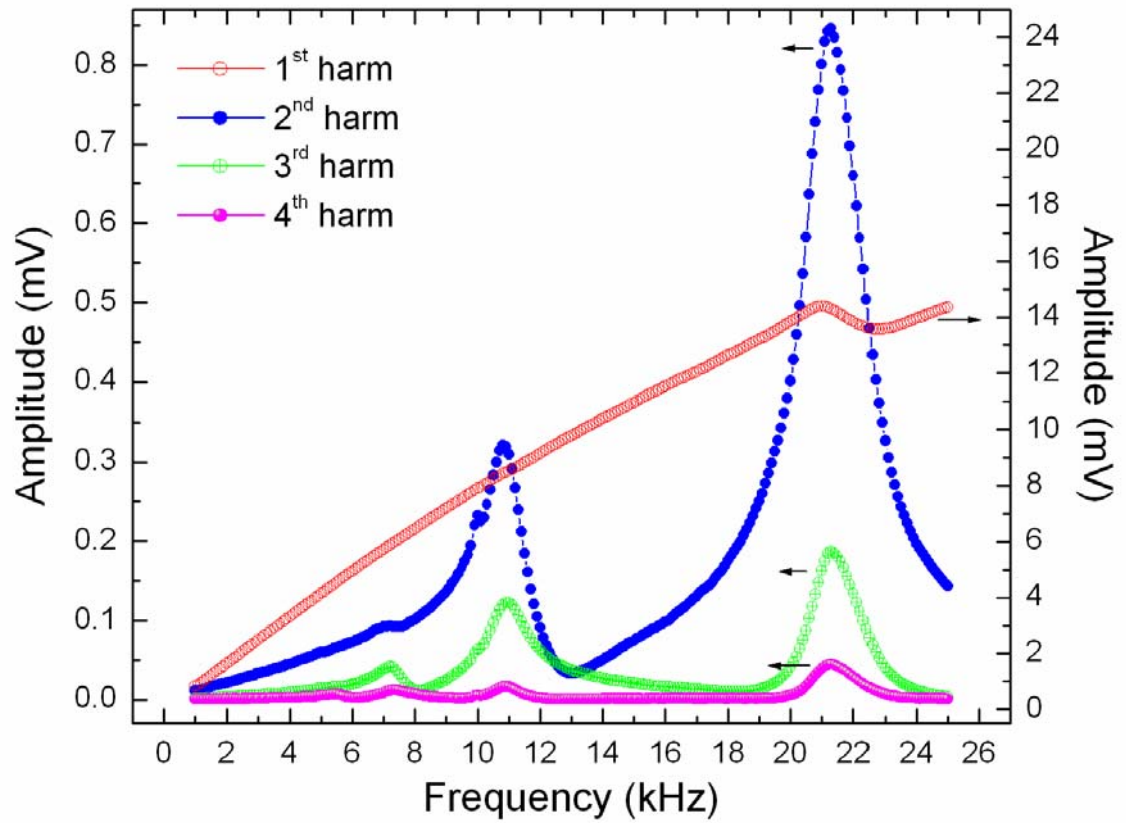
Figure 6.3: Full spectrum of the first four harmonics of a cantilever of dimensions (350 μm long, 35 μm wide, and 2 μm thick).
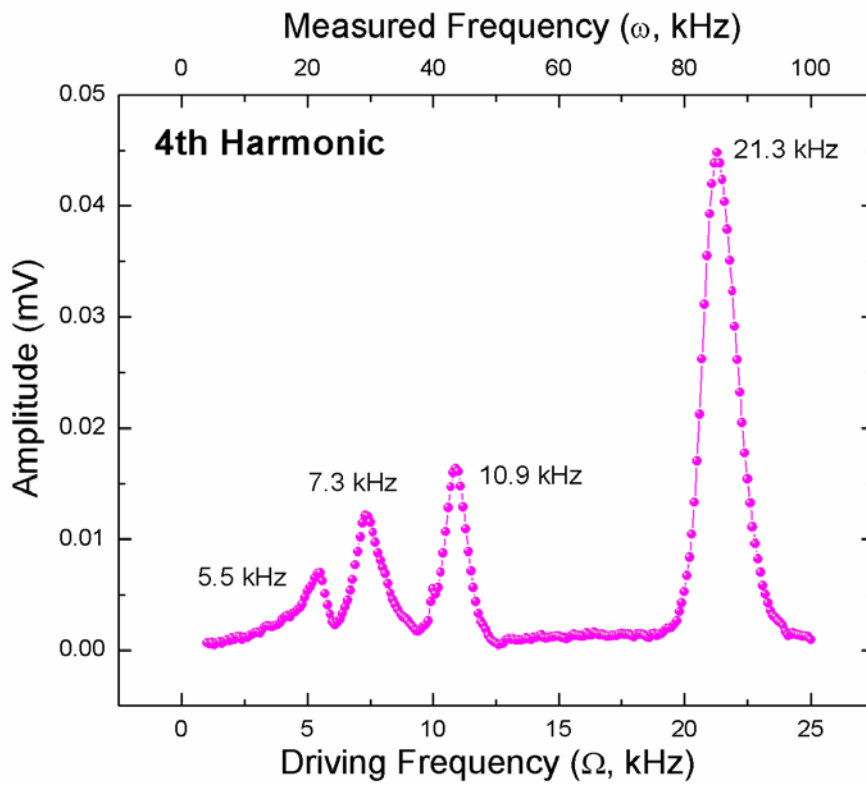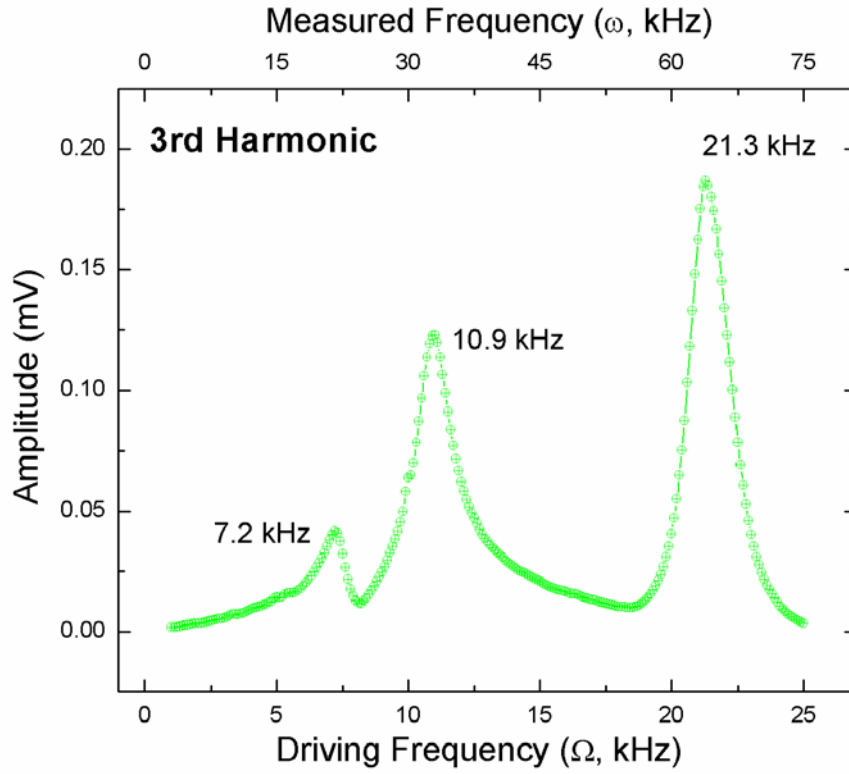
Figure 6.4: Full spectrum of the 3rd and 4th harmonics from Fig. 6.3. One can discern n resonant peaks for the nth harmonic. For example, the 3rd harmonic has three peaks and the 4th harmonic has four peaks.
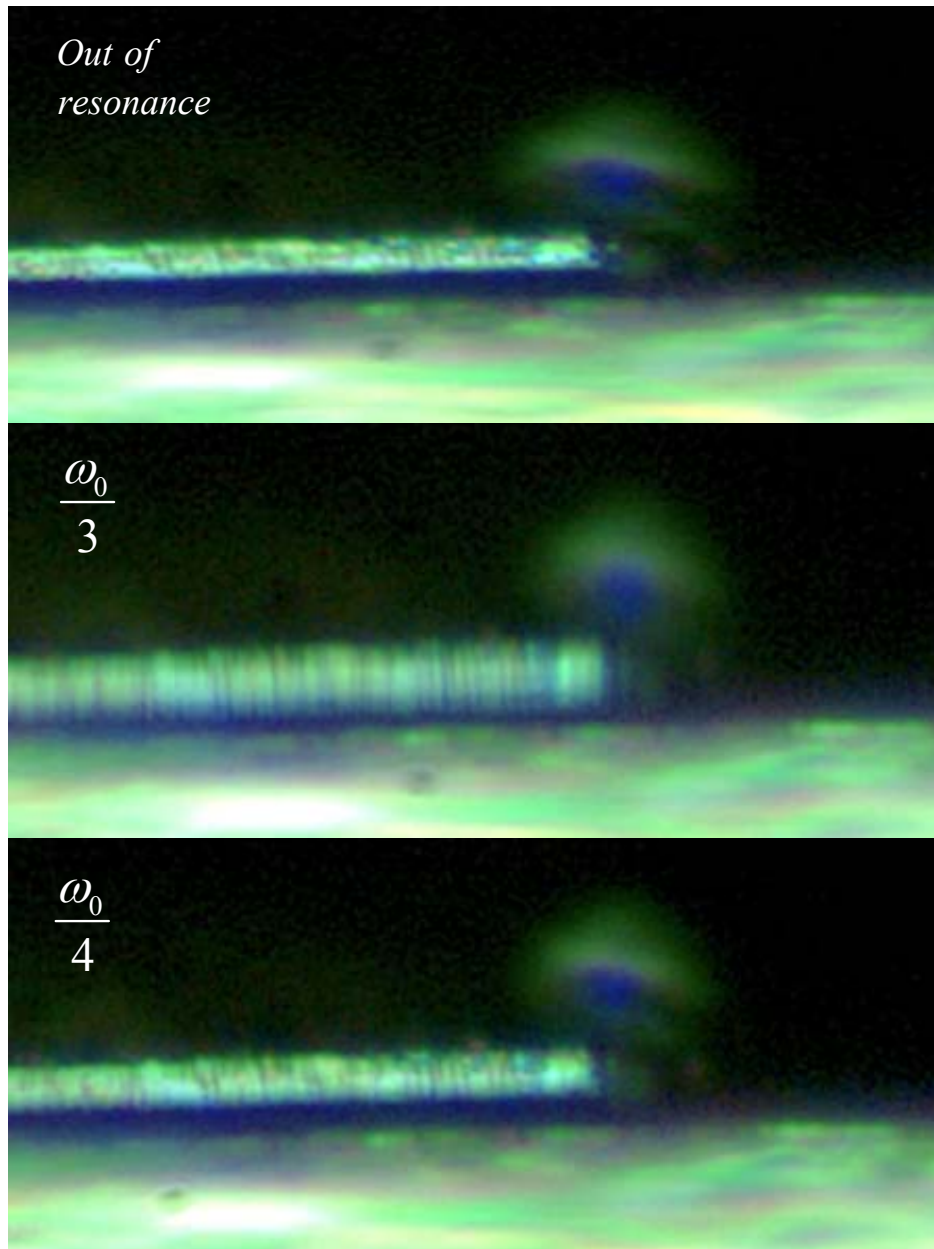
Figure 6.5: Darkfield optical microscope images of a cantilever in resonance at $\omega_0/3$, $\omega_0/4$, and out of resonance. Note that the cantilever is 2 μm thick.
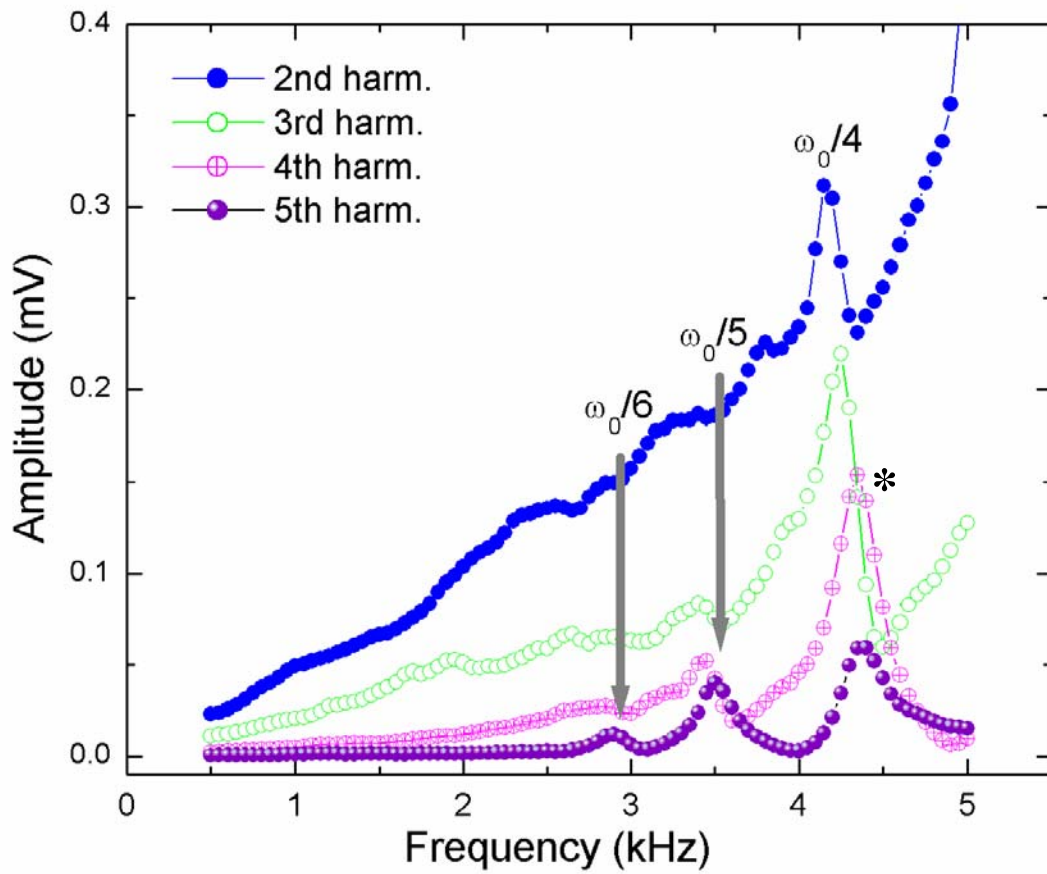
Figure 6.6: Spectrum below 5 kHz for the first five harmonics.

the cantilever was brought to about two microns away from a large counter electrode. An excitation voltage of 1 V_{ac} and $3V_{dc}$ was used. Any larger voltage would have collapsed the cantilever into the counter electrode. As can be seen in Fig. 6.6, a resonance peak is visible at the sixth superharmonic $\omega_0/6$.

By overdriving the cantilever, a peak also appeared at $\omega_0/4$ when measuring at the second harmonic. This peak illustrates the transition from equation (6.70) to equation (6.9). The reason for this transition is not entirely clear. It is either from (1) amplification of the signal due to decreasing the gap distance or (2) from a transition from nonlinearities in the force to addition nonlinearities from the overdriven mechanical motion of the cantilever. Further evidence supports the second case. Nonlinearities in the mechanical motion would add more disorder in the wave that describes the motion of the cantilever. This may superimpose another set of harmonics which can then be measured at any harmonic instead of only at the restricted set given by equation (6.7). The dominant mode of vibration in a set of harmonics, which can be convoluted to describe the real motion at any particular superharmonic, is still at

$$\frac{n\omega_0}{m} = \omega_0 \tag{6.10}$$

where again n is the harmonic being *measured*, but addition peaks due to nonlinearities begin to appear at values above these peaks. For example, the star * in Fig. 6.6 is next to a peak that is at $\omega_0/4$ and measured at the 4th harmonic. At $\omega_0/4$, the cantilever is in resonance. It can only vibrate at resonance at the frequency of ω_0. This is what equation (6.10) describes. With the cantilever resonating in some nonlinear wave shape at ω_0, we can expect to deconvolute that wave starting with the peak indicated by the star into

harmonics starting with $\dfrac{n\omega_0}{m} = \omega_0$ as the first harmonic and then $\dfrac{(n+1)\omega_0}{m} = \omega_0$ as the second and so on to get

$$\frac{(n+q)\omega_0}{m} = \omega_0 \quad \text{where} \quad q = 0,1,2,... \quad \text{and} \quad n = m. \tag{6.11}$$

So then why are there peaks above the star at $\omega_0/4$? This is due to the additional nonlinearities in the motion of the cantilever as mentioned above. So the peak at the 3rd harmonic at $\omega_0/4$ is measured at $\frac{3}{4}\omega_0$ and corresponds to a part of the complicated vibration of the cantilever and due to the nonlinearities of the deflection and not from the nonlinearities in the electrostatic force. It is reasonable to assume that these purely mechanical nonlinearities are absorbed into the signals that are from the electrostatic nonlinearities in equation (6.11). Figure 6.7 shows a scan at the 2nd harmonic where there is a peak that appears in the upper trace due to extra excitation.

6.5 Conclusions

The data shown throughout this chapter illustrates the power of HDR with its ability to probe multiple levels of nonlinearities. The data presented here demonstrates that peaks from electrostatic actuation/detection can be detected at $m\omega_0/n$ and the cantilever can be driven into resonance at superharmonics of order ω_0/n. As micro- and nano- cantilevers become more implemented as sensors, mechanical resonators, etc., a need for exploiting the usefulness of these oscillators becomes important. And by using HDR, the ability to monitor multiple peaks may facilitate this usefulness.
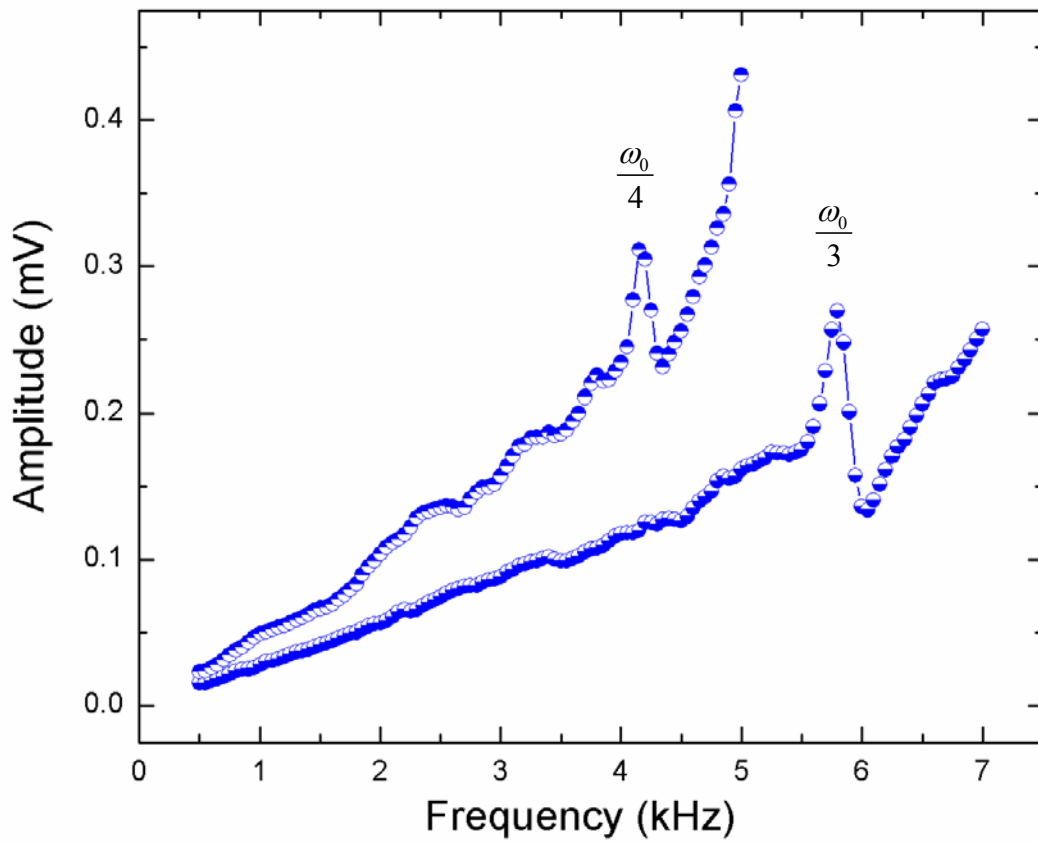
Figure 6.7: Two spectra taken at the 2nd harmonic. A peak appears at $\omega_0/4$ with more excitation.

APPENDICES

Appendix A

HDR in air and vacuum

A Nikon Epiphot 200 darkfield/brightfield microscope (Fig. A.1) is used to make the measurements in air while viewing each cantilever. The microscope is equipped with a 150 watt light source in order to see at smaller dimensions. The HDR setup includes two lock-in amplifiers, a box containing the charge sensitive amplifier, a floating battery powered dc power supply, and the signal generator.

We use two different lock-in amplifiers depending on the frequency range. A lower frequency lock-in measured the larger cantilevers with a limit between 0-100 kHz. An RF lock-in allowed us to perform measurements between 100 kHz and 200 Mhz. All of the nanotube measurements were taken with the RF lock-in. This lock-in is limited, however, to the first and second harmonic. Therefore, all superharmonic measurements were limited to frequencies between 0 and 100 kHz.

The silicon cantilever or nanotube could be manipulated using XYZ Newport micromanipulaters near a counter electrode. Once mounted on the gold coated tungsten tip, the nanotubes are manipulated either a parallel or tip-to-tip configuration. The silicon cantilever is attached to a rectangular chip which is mounted on a short rod. The counter electrode, a sharpened Au coated tungsten tip, is surrounded by a nonconductive material and then this is wrapped in copper tape up to the very tip of the counter electrode (see bottom of Fig. A.2). As shown in Fig. A.2, a special holder was built to minimize drift that occurred frequently when using alligator clips to hold the cantilever and counter

electrode. The holders are made out of nylon where the connecting wires inside is coaxial to copper tape that is wrapped around the nylon. The copper acts as a Faraday cage to prevent electrical crosstalk noise between the contacts that connect to each side and from room noise that could be picked up by the cantilever, which is connected directly to the FET on the A250 board thereby basically acting as an antenna without shielding.

Figure A.1: Digital image of the experimental setup used to make the HDR measurements.
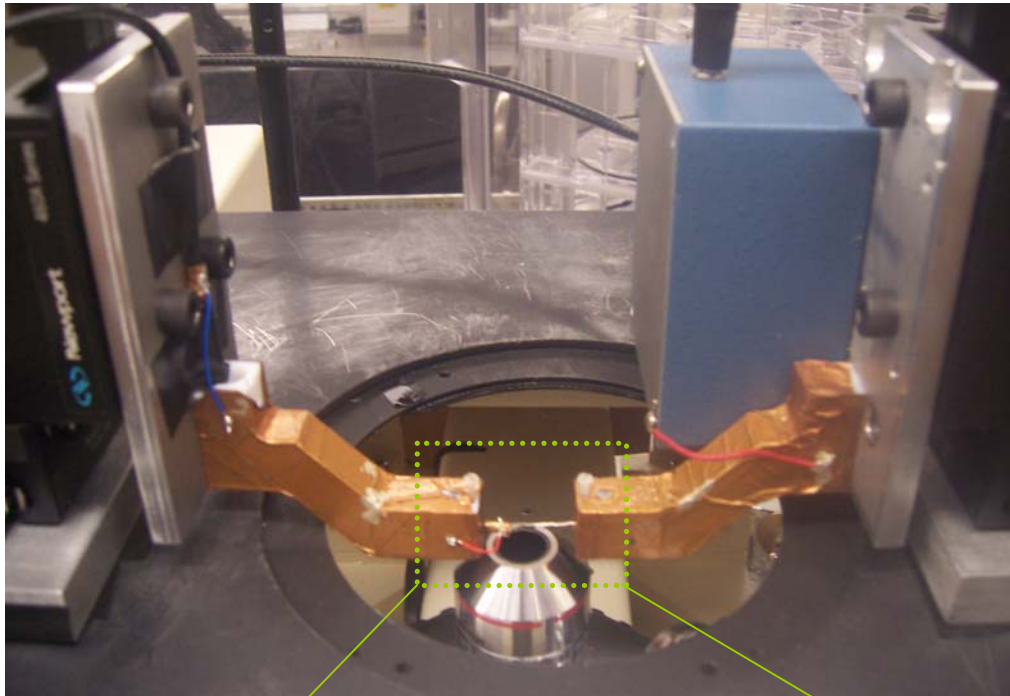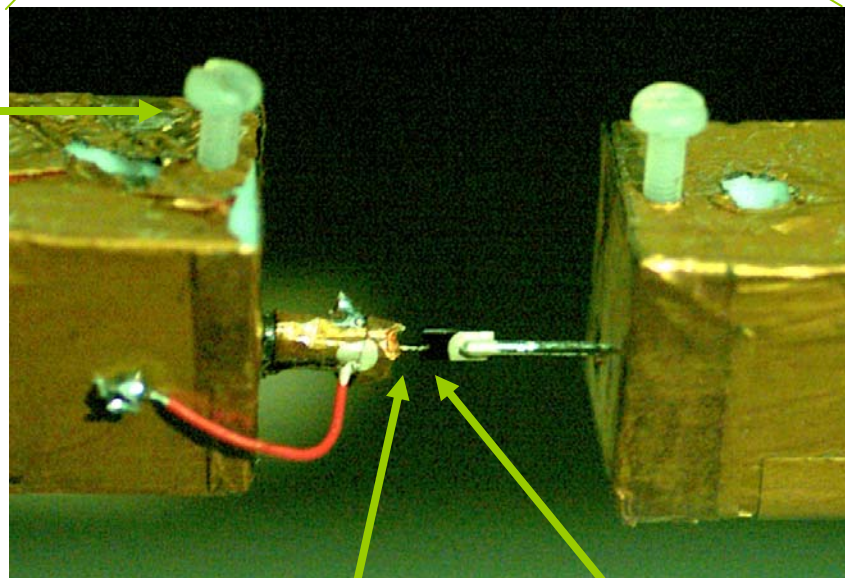
Figure A.2: Digital image of the holders that are used to make HDR measurements over the optical microscope. In the bottom image, the cantilever is on the right while the counter electrode is on the left.

Figure A.3 shows the system built for vacuum measurements. Inside is a removable stage that has an XYZ piezotube. A silicon cantilever is mounted to the piezotube and the tungsten tip is glued to a clear movable block. The block was manipulated using the Newport micromanipulators until the cantilever was aligned parallel to the cantilever. An image which captures this process is shown as Fig. A.4. Once the block was in place it was glued using a five minute epoxy. The five minute epoxy was found to be a remarkable but simple tool to use for keeping small structures in place. The epoxy is easy to remove if the structure needs to be reused.
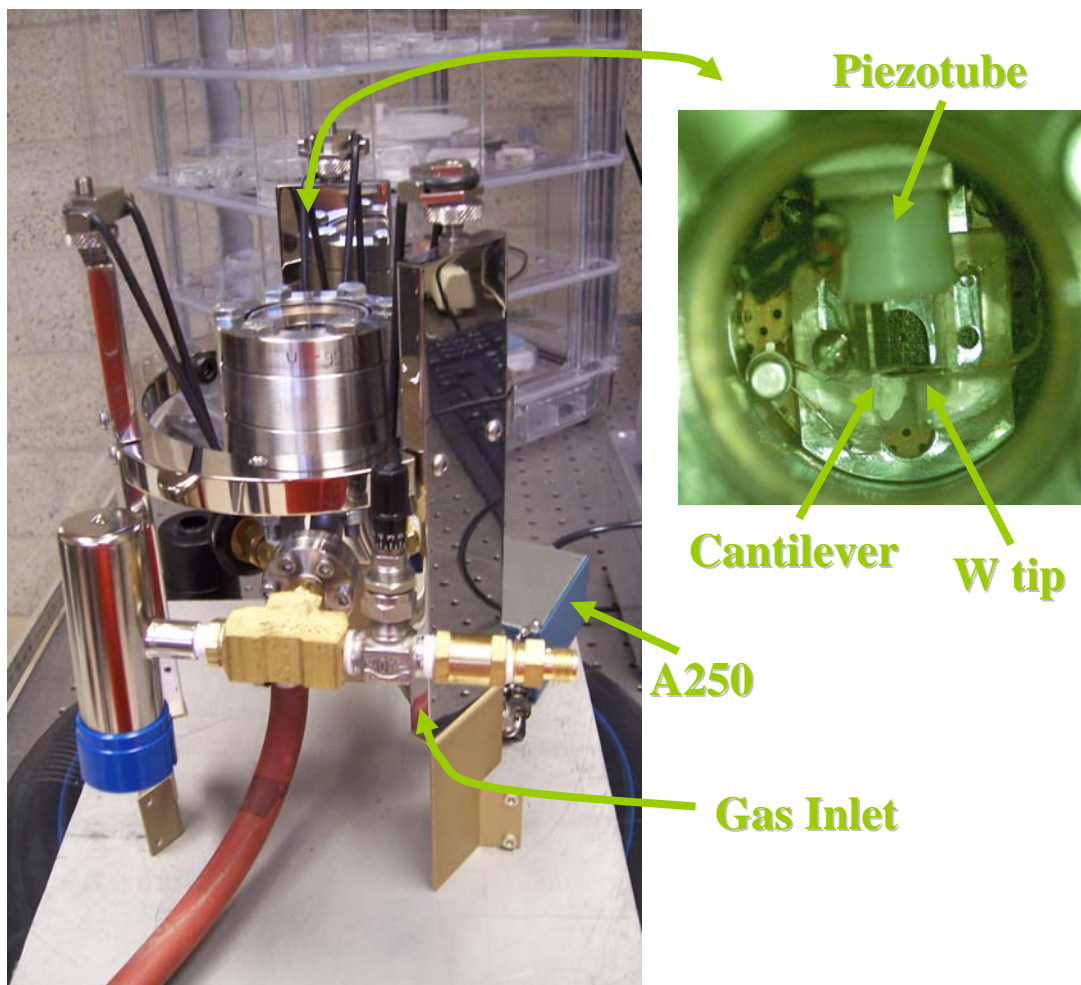
Figure A.3: Vacuum system used for measurements presented in Chapter 4.
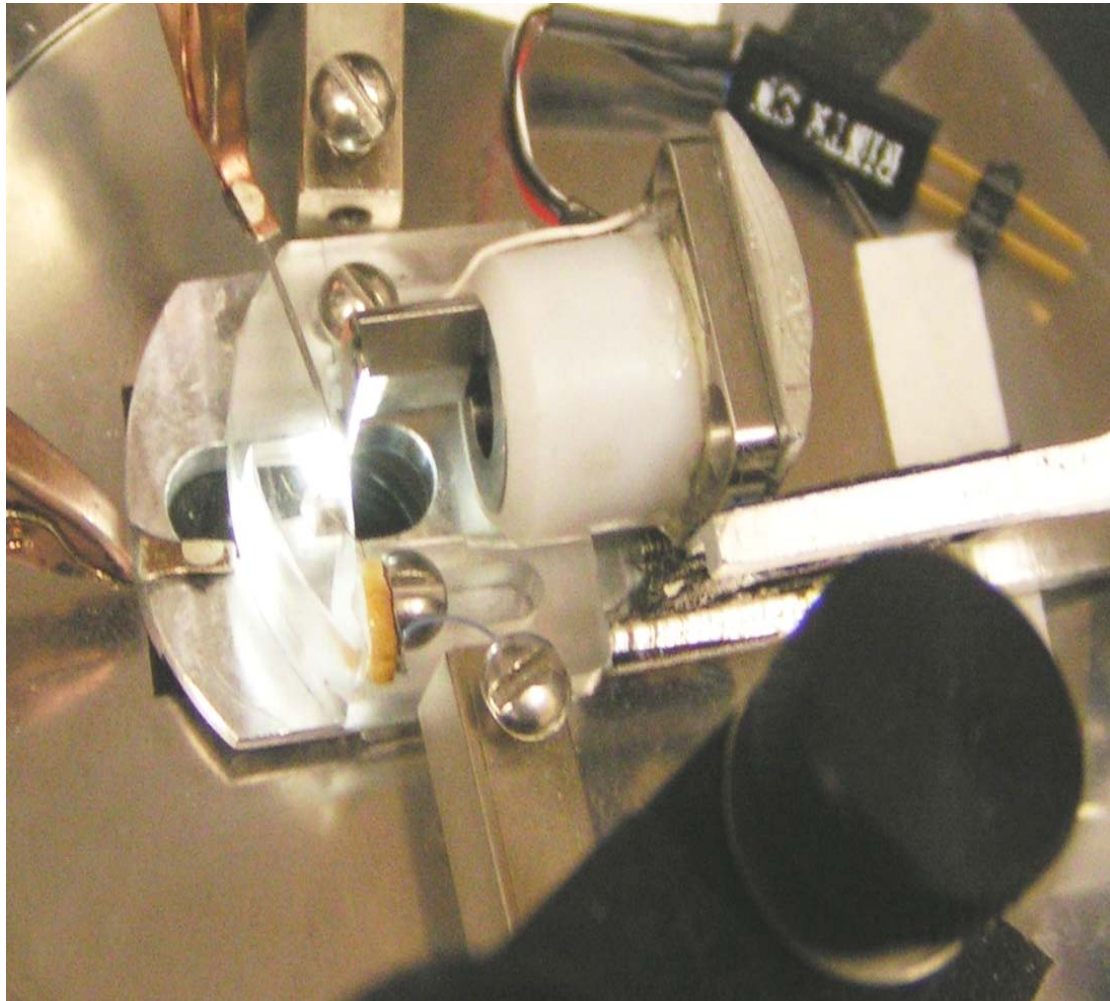
Figure A.4: This image illustrates steps taken to create a portable stage which holds the piezotube with the cantilever and counter electrode.

Appendix B

Procedure for etching tungsten probe tips

The schematic for etching the tungsten tip is illustrated in Fig. B.1. A 2 molar solution of NaOH and de-ionized water is added to a beaker with a carbon rod used as an electrode. The tip of a 0.1 mm tungsten wire is dipped into the solution at a depth of about 1 inch. A variac is used to control the ac voltage across the carbon and tungsten wire. The ac voltage is usually about 5 volts. A current flows between the wire and rod. During the etching process, bubbles rapidly form around the immersed wire. After about 30 seconds of etching, the wire begins to thin and shorten. Once it shortens to about 2-5 mm below the surface, the tip should be very sharp. This method can easily etch the ends of the tips to 100nm in diameter and has been etched in our lab to 15 nm in diameter. The process takes less than a minute, which allows the user to etch a large number of tips in a short period of time. Each tip is ready for use after undergoing a three step cleaning process. Deionized water is used first to dilute the NaOH. Acetone then is used to further clean off the NaOH, and then another bottle of purified water is used to clean off the acetone (since acetone leaves behind residue).

Figure B.1: Schematic drawing of W wire immersed in NaOH solution. The carbon rod serves as an electrode while the tungsten tip etches in the solution from the bottom of the wire to the desired length.
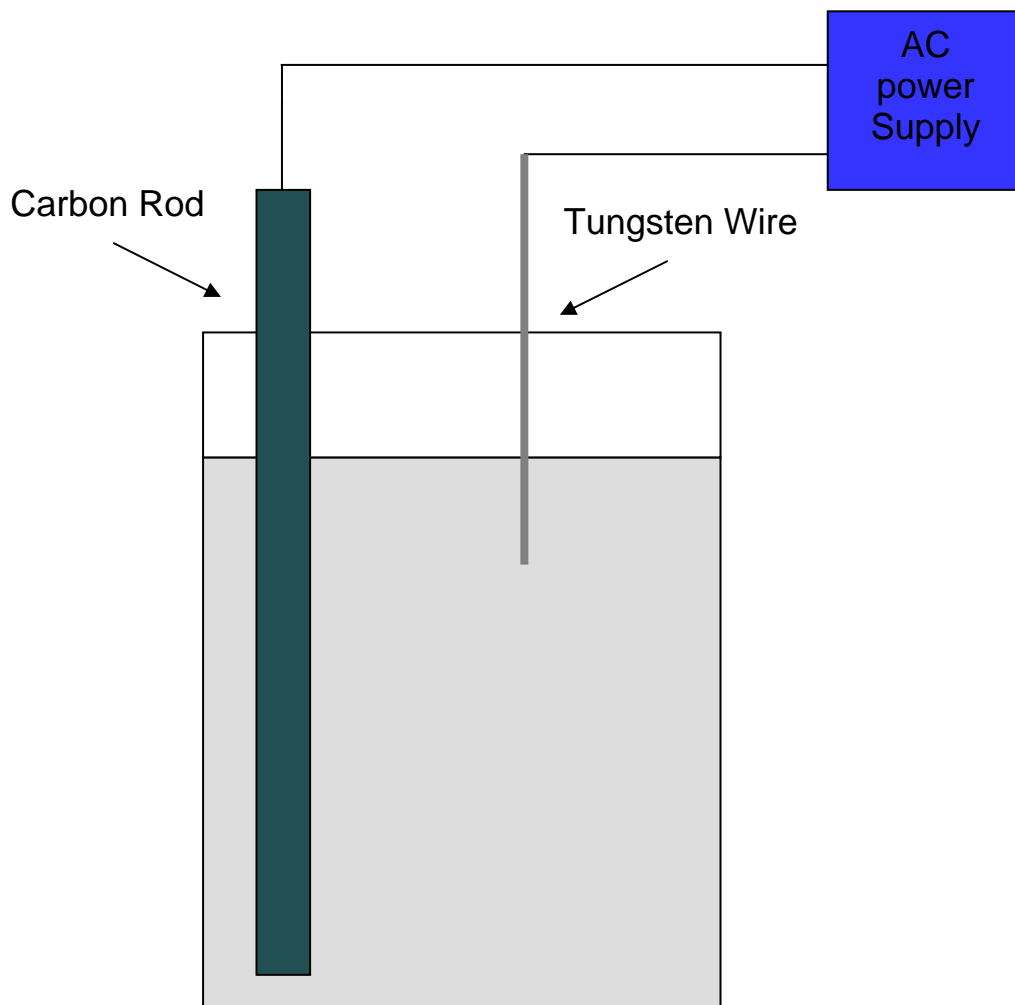
Appendix C

Procedure for nanotube retrieval

An optical inverted Epiphot 200 darkfield/brightfield microscope is used to observe the nanotubes. It was possible to view a multiwalled carbon nanotube down to about 20-30 nm in diameter. Two Newport 460A-XYZ micro-manipuators are set opposite to one another on the microscope stage. They are attached firmly to the stage with strong magnets. Miniature smooth tipped alligator clips are attached to each manipulator. The alligator clips are the tools which hold any materials that are manipulated in the preparation process. SEM tape is folded in half and fixed into an alligator clip, and then dipped into a batch of nanotubes. Visible excess mats of MWNTs are blown off, and then the alligator clip is pushed into its holder. The other manipulator is used to hold a sharp tungsten tip. The process of retrieving the MWNT is shown in fig. C.1. Once a MWNT is found, the tip is brought close to it and then touched with a small overlap. Then a DC bias voltage of about 3-7 V is applied between the Y junction and the tip. This provides an additional force to extract the MWNT. The tip is then pulled back to pull off the tube. If it does not come with the tip, then the voltage is turned off and the tip is brought back to the same position. This is done because a spark may occur if the voltage is on while the tip is maneuvered back to the MWNT. The procedure is then repeated until the MWNT comes off. However, sometimes the MWNT is well enough attached that it will not separate from the mat. In this case, the voltage can be carefully increased to the point that the MWNT sparks where it is joined with the mat and is now attached to the tip.
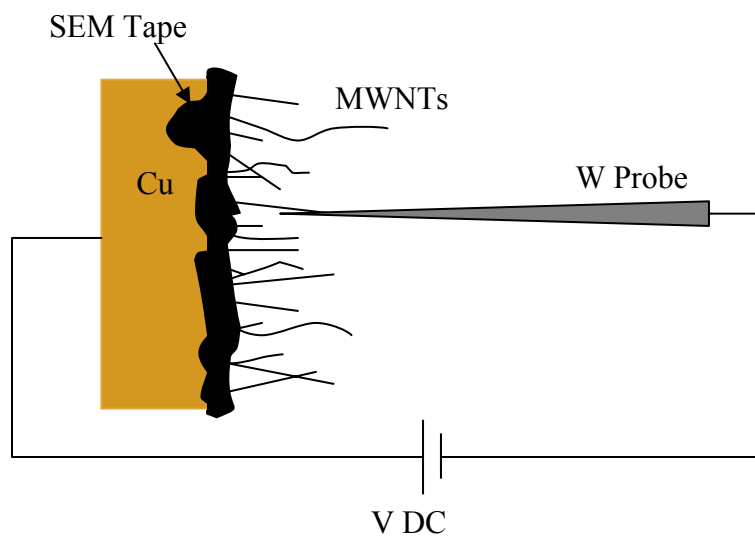
Figure C.1: Schematic of nanotube retrieval. The nanotubes are pulled using a sharp tungsten tip while a bias voltage is applied between the nanotube and tip.

Equipment List

1. Stanford Research Systems SR 850 Lockin Amplifier, located in Room 2.

2. Stanford Research Systems SR 844 Lockin Amplifier, located in Room 2.

3. Stanford Research Systems SR 810 Lockin Amplifier, located in Room 2.

4. Veeco Digital Instruments CP II (CP II) Scanning Probe Microscope (SPM), located in Room 11.

5. Epiphot 200 darkfield/brightfield microscope with a 50x 8.4 mm long working distance objective lense, located in room 2.

REFERENCES

[1] G. Binnig, C. F. Quate, and C. Gerber, *Phys. Rev. Lett.* **56**, 930 (1986).

[2] N. V. Lavrik, M. J. Sepaniak, and P. G. Datskos, *Rev. Sci. Instrum*. **75**, 2229 (2004).

[3] E. A. Wachter and T. Thundat, *Rev. Sci. Instrum*. **66**, 3662 (1995).

[4] Y. Arntz, J.D. Seelig, H.P. Lang, J. Zhang, P. Hunziker, J.P. Ramseyer, E. Meyer, M. Hegner, and Ch. Gerber, *Nanotechnology*, **14**, 86 (2003).

[5] R. McKendry, J. Zhang, Y. Arntz, T. Strunz, M. Hegner, H.P. Lang, M.K. Baller, U. Certa, E. Meyer, H.J. Güntherodt, and Ch. Gerber, *Proc. Nat. Acad. Sci. USA*, **99**, 9783 (2002).

[6] R. Berger, H.P. Lang, Ch. Gerber, J.K. Gimzewski, J.H. Fabian, L. Scandella, E. Meyer, and H. J. Güntherodt, *Chem. Phys. Lett*. **294**, 363 (1998).

[7] M.D. Ward and D.A. Buttry, *Science*, **249**, 1000 (1990).

[8] H.P. Lang, M.K. Baller, R. Berger, Ch. Gerber, J.K. Gimzewski, F.M. Battiston, P. Fornaro, J.P. Ramseyer, E. Meyer, and H.J. Güntherodt, *Analytica Chimica Acta*, **393**, 59 (1999).

[9] M. Roukes, *Scientific American*, **285**, 48, (2001).

[10] S. J. O'Shea, P. Lu, F. Shen, P. Neuzil and Q. X. Zhang, *Nanotechnology*, **16**, 602 (2005).

[11] I. Voiculescu, M. E. Zaghloul, R. A. McGill, E. J. Houser, and G. K. *Sensors Journal, IEEE*, **5**, 641 (2005).

[12] E. H. Conradie and D. F. Moore, *J. Micromech. Microeng.*, **12,** 368 (2002).

[13] C. W. Leow, A. B. Mohammad, and N. M. Kassim, *Proceedings IEEE International Conference on Semiconductor Electronics,* Penang Malaysia, ICSE 2002.

[14] L. Jiang, M. Hassan, R. Cheung, A. J. Harris, J. S. Burdess, C. A. Zorman and M. Mehregany, *Microelectronic Engineering*, **78-79,** 106 (2005).

[15] D. Bullen and C. Liu, *Sensors and Actuators A: Physical*, **125**, 504 (2006).

[16] J. Teva, G. Abadal, F. Torres, J. Verd, F. Pérez-Murano and N. Barniol *Ultramicroscopy*, **106**, 808 (2006).

[17] P. Poncharal, Z. L. Wang, D. Ugarte, and W. A. de Heer, *Science* **283**, 1513 (1999).

[18] M. F. Yu, G. J. Wagner, R. S. Ruoff, and M. J. Dyer, *Phys. Rev. B* **66**, 073406 (2002).

[19] S. T. Purcell, P. Vincent, C. Journet, and T. B. Vu, *Phys. Rev. Lett*. **89**, 276103-1 (2002).

[20] K. Yum, Z. Wang, A. P. Suryavanshi, and M. Yu, *Appl. Phys*. *Lett*. **96**, 3933 (2004).

[21] J. Gaillard, M. J. Skove, and A. M. Rao, *Appl. Phys. Lett*. **86**, 233109-1 (2005).

[22] G. Abadal, Z.J. Davis, B. Helbo, X. Borrise, R. Ruiz, A. Boisen, F. Campabadal, J. Esteve, E. Figueras, F. Perez- Murano, and N. Barniol, *Nanotechnology* **12,** 100 (2001).

[23] J. Verd, G. Abadal, J. Teva, M. Gaudo, A. Uranga, X. Borrise, F. Campabadal, J. Esteve, E. Costa, F. Murano, Z. Davis, E. Forsen, A. Boisen, and N. Barniol, *J. Micro. Sys.* **14**, 508 (2005).

[24] K. Ekinci and M. Roukes, *Rev. Sci. Instrum*. **76**, 061101 (2005).

[25] D. Sarid, *Scanning Force Microscopy*, Oxford University Press, New York, 1991.

[26] M. D. Ventra, S. Evoy, and J. R. Heflin, Jr, Introduction to Nanoscale Science and Technology, Kluwer Academic Publishers, New York, 2004.

[27] E. Wong, P. Sheehan, and C. M. Lieber, *Science* **277**, 1971 (1997).

[28] P. Poncharal, Z.L. Wang, D. Ugarte, and W.A. de Heer, *Science* **283,** 1513 (1999).

[29] R. Gao, Z. L. Wang, Z. Bai, W. A. de Heer, L. Dai, and M. Gao. *Phys. Rev. Lett.* **85,** 622 (2000).

[30] Z. L. Wang, R. P. Gao, Z. W. Pan, and Z. R. Dai, *Adv. Eng. Mat*. **3,** 657 (2001).

[31] Z.L. Wang, R.P. Gao, P. Poncharal, W.A. de Heer, Z.R. Dai, Z.W. Pan *Ma. Sci. and Eng.* **16,** 3 (2001).

[32] M. S. Dresselhaus, G. Dresselhaus, K. Sugihara, I. L. Spain, H. A. Goldberg *Graphite Fibers and Filaments,* Springer, Berlin, 1988.

[33] M. Blencowe and M. Wybourne, *Appl. Phys. Lett*. **77**, 3845 (2000).

[34] A. Bertz, H. Symanzik, C. Steiniger, A. Hoffer, K. Griesbach, K. Stegemann, G. Ebest, and T. Gessner, *Sensors and Acuators* **93**, 163 (2001).

[35] R. Andrews, D. Jacques, A. M. Rao, F. Derbyshire, D. Qian, X. Fan, E. C. Dickey and J. Chen, *Chem. Phys. Letters*, **303,** 467 (1999).

[36] B. Sadanadan, T. Savage, S. Bhattacharya, T. Tritt, A. Cassell, M. Meyyappan, Z.R. Dai, Z.L. Wang, R. Zidan, and A. M. Rao, *Journal of Nanoscience and Nanotechnology*, **3**, 99 (2003).

[37] H. Dai, J. H. Hafner, A. G. Rinzler, D. T. Colbert, and R. E. Smalley, *Nature* **384**, 147 (1996).

[38] J. Gaillard, M. J. Skove, R. Ciocan, and A. M. Rao, *Rev. Sci. Instrum.* **77**, 073907 (2006).

[39] M. Napoli, W. Zhang, K. Turner, and B. Bamieh, *J. Micro. Sys.* **14**, 295 (2005).

[40] P. G. Datskos, T. Thundat, Lavrik, and V. Nickolay, *Encyclopedia of Nanoscience and Nanotechnology*, **5,** 551 (2004).

[41] S. Evoy, D. W. Carr, L. Sekaric, A. Olkhovets, J. M. Parpia, and H. G. Craighead, *Journal of Applied Physics*, **86**, 6072 (1999).

[42] J. Mertensa, E. Finota,, T. Thundatb, A. Fabrea, M. Nadalc, V. Eyraudc, and E. Bourillota, *Ultramicroscopy* **97**, 119 (2003).

[43] J. Gaillard, R. Ciocan, M. J. Skove, and A. Rao, *APS March Meeting*, 2005, Los Angeles, CA, X27.00012.

[44].R. Ciocan, J. Gaillard, M. J. Skove, and A. M. Rao, *Nano Lett.* **5**, 2389-2393 (2005).

[45] M. J. Treacy, T. W. Ebbesen, and J. M. Gibson, *Nature,* **381**, 678 (1996).

[46] M. Yu, O. Lourie, M. J. Dyer, K. Moloni, T. F. Kelly, and R. S. Ruoff, *Science*, **287**, 637 (2000).

[47] O. Lourie, and H. D. J. Wagner, *Mater. Res.* **13**, 2418 (1998).

[48] M. Yu, G. J. Wagner, R. S. Ruoff, and M.J. Dyer *Phys. Rev. B*, **66**, 073406 (2002).

[49] S. T. Purcell, P. Vincent, C. Journet, and V. T. Binh *Phys. Rev. Lett.* **89**, 276103-1 (2002).

[50] K. Yum, Z. Wang, A. P. Suryavanshi, and M. Yu, *J. Appl. Phys.* **96**, 3933 (2004).

[51] J. Gaillard, M. J. Skove, and A. M. Rao, *Proc. of Mat. Res. Soc.* Meeting, Boston, (2004).

[52] R. Gao, Z. Pan, and Z. L. Wang *Appl. Phys. Lett*. **78**, 757 (2001).

[53] I.G. Main, *Vibration and Waves in Physics*, Cambridge University Press, Cambridge, 1993.

[54] Z. L. Wang, P. Poncharal and W. A de Heer, *Pure Appl. Chem.* **72**, 209 (2000).

[55] D. Qian, G. J. Wagner, W. K. Liu, M. Yu, and R. S. Ruoff. *Appl. Mech. Rev.* **55**, 495 (2002).

[56] Q. Lu, G. Keskar, R. Ciocan, L. L. Larcom, and A. M. Rao, *NT05: Sixth International Conference on the Science and Application of Nanotubes*, 2005, Gothenburg, Sweden, 426.

[57] V. Sazonova, Y. Yaishm, H. Üstünel, D. Roundy, T. Arias, and P.McEuen, *Nature* **431**, 284 (2004).

[58] M. Cartmell, *Introduction to Linear, Parametric and Nonlinear Vibrations,* Chapman and Hall, London, 1990.

[59] S. K. De and N. R. Aluru, *Journal of Microelectromechanical Systems*, **15**, 355 (2006).

[60] E. M. Abdel- Rahman, M. I. Younis, and A. H. Nayfeh, *J. Micromech. Microeng*, **12**, 759 (2002).

[61] E. M. Abdel- Rahman and A. H. Nayfeh, *J. Micromech. Microeng*, **13**, 491 (2003).

[62] Z. Jin and Y. Wang, *Sensors and Actuators A: Physical*, **64**, 273 (1997).